

---

# Simulated galaxy interactions in cosmological and idealized environments

Geray Simon Karademir

---



Munich 2018



# Simulated galaxy interactions in cosmological and idealized environments

Master's Thesis  
at the  
University Observatory  
of the  
Ludwig–Maximilians–Universität

submitted by

Geray Simon Karademir  
(Matr. Nr.:10756342)  
born on April 3, 1993 in Munich

supervised by:  
PD Dr. Klaus Dolag and Dr. Rhea-Silvia Remus

Munich, May 9, 2018





# Simulationen von wechselwirkenden Galaxien in kosmologischen und idealisierten Umgebungen

Masterarbeit  
an der  
Universitäts-Sternwarte  
der  
Ludwig-Maximilians-Universität

eingereicht durch

Geray Simon Karademir  
(Matr. Nr.:10756342)  
geboren am 3. April 1993 in München

betreut durch:  
PD Dr. Klaus Dolag und Dr. Rhea-Silvia Remus

München, 9. Mai 2018



*The Road goes ever on and on  
Down from the door where it began.*

J.R.R. Tolkien, *The Fellowship of the Ring*



# Abstract

Most of all galaxies are not field galaxies but are accompanied by other galaxies in groups or clusters. A special case of these galaxy gatherings are compact galaxy groups, which are extremely dense accumulations of galaxies in which galaxy interactions occur very frequently. These interactions have a huge impact on the corresponding galaxies and are a fundamental part of galaxy evolution. The information about the merging events are stored in the outer stellar halo of a galaxy or in the intra group light (IGL) respectively. In this thesis cosmological zoom simulations of compact groups as well as a parameter study using high-resolution isolated galaxy merger simulations covering a large bandwidth of orbit parameters and mass-ratios were used to study the effects of galaxy interactions onto their evolution. During this study it is found that compact galaxy groups are physically dense objects, and indications were found for the final phase of compact groups to be giant elliptical galaxies in isolated environments. In addition it can be seen that mergers always deposit significant amounts of mass in the outer stellar halos of galaxies and are therefore building and contributing to the IGL. Furthermore is shown that the outer stellar halo is enriched mainly by minor and very minor mergers, while the morphology of galaxies is mainly influenced by major or intermediate mergers.



# Contents

<b>Abstract</b>	<b>viii</b>
<b>1 Introduction</b>	<b>1</b>
<b>2 Zoom-simulations of compact galaxy groups</b>	<b>7</b>
2.1 Hickson compact groups . . . . .	7
2.1.1 Classification . . . . .	8
2.1.2 Space distribution, dynamical properties and structure . . . . .	8
2.1.3 Formation and evolution . . . . .	9
2.2 Simulations . . . . .	11
2.2.1 Objects . . . . .	11
2.2.2 Tracking . . . . .	13
2.2.3 Initial conditions . . . . .	14
2.2.4 Re-simulating . . . . .	15
2.3 Smallest enclosing circle . . . . .	17
2.3.1 Convex hull . . . . .	17
2.3.2 Skyum algorithm . . . . .	20
2.4 Results . . . . .	22
2.4.1 Resolution limitation and mass loss . . . . .	22
2.4.2 Group classification and lifetime . . . . .	23
2.4.3 Decoupling of gas and intragroup light . . . . .	26
2.4.4 Kinematic evolution . . . . .	28
2.4.5 Mass-size relation . . . . .	30
2.4.6 Final stage of evolution . . . . .	32
2.4.7 Non-group objects . . . . .	33
2.5 Conclusion and possible future work . . . . .	35
<b>3 Idealized galaxy mergers</b>	<b>37</b>
3.1 Method . . . . .	38
3.1.1 Galaxy set-up . . . . .	38
3.1.2 Stability tests . . . . .	39
3.1.3 Merger set-up . . . . .	40
3.2 Results . . . . .	42

---

3.2.1	Mass-deposition . . . . .	42
3.2.2	Theoretical predictions . . . . .	44
3.2.3	Contribution to the mass-distribution by different origin . . . . .	45
3.2.4	Disc growth . . . . .	46
3.2.5	Shells and streams . . . . .	48
3.2.6	Luminosity distribution . . . . .	49
3.2.7	Radial anisotropies . . . . .	50
3.3	Conclusion . . . . .	51
<b>4</b>	<b>Summary and conclusion</b>	<b>53</b>
<b>A</b>	<b>Appendix</b>	<b>55</b>
A.1	Compact galaxy groups . . . . .	55
A.2	Galaxy mergers . . . . .	59
	<b>List of Figures</b>	<b>69</b>
	<b>List of Tables</b>	<b>71</b>
	<b>Bibliography</b>	<b>73</b>
	<b>Acknowledgements</b>	<b>80</b>



# 1. Introduction

Galaxies are one of the key objects in cosmology and they occur in all kinds of sizes, luminosities and morphologies. The standard classification scheme for galaxies is the so called Hubble classification, which was extended by de Vaucouleurs (1959) and is displayed in Figure 1.1:

HUBBLE-DE VAUCOULEURS DIAGRAM

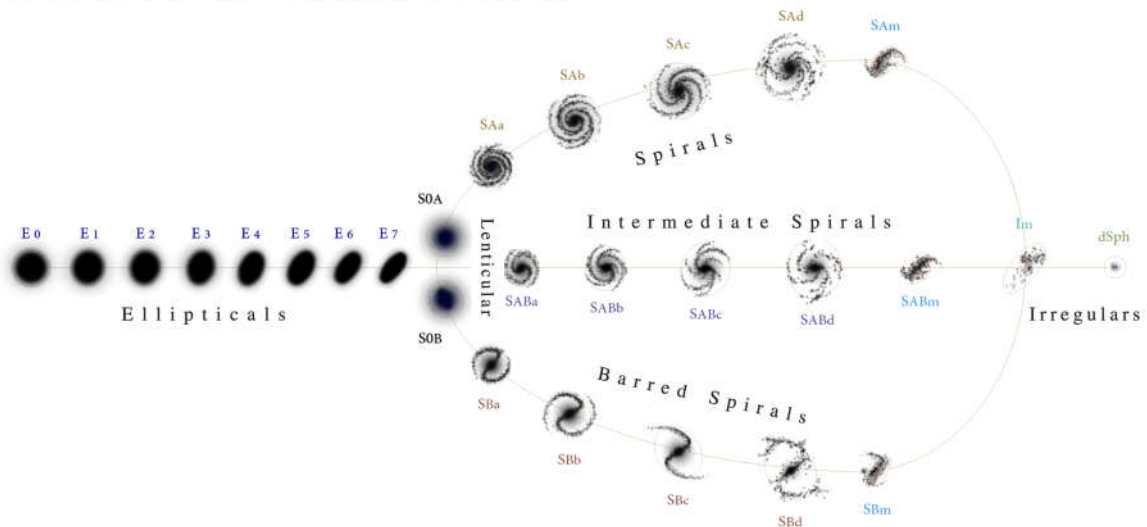


Figure 1.1: The extended Hubbles Tuning fork, a classification scheme for galaxies (Ciccolella and Leo)

Elliptical galaxies have an almost spherical distribution of stars, which mainly move on random orbits around the gravitational center of the galaxy. They are mostly gas poor and don't show signs of recent star formation in general. The other major type of galaxies are disc galaxies. They have, in contrast to elliptical galaxies, a highly ordered stellar rotating disc, which is often build of spiral arms, in which star formation is taking place, with a central spherical bulge that shows similar properties as an elliptical galaxy but is much smaller. For many of these spiral galaxies a central bar is dominating the disc, while

spiral arms are present at the end of this bar. Between the distinct classes of elliptical and spiral galaxies, an intermediate type of galaxy exists, which is also flat, but a bit thicker than disc galaxies, but has almost no star formation like elliptical galaxies. Using the extended Hubble classification these galaxies are called S0 galaxies and are defined in the de Vaucouleurs-classification scheme as SA0 or SAB0 galaxies. These galaxies are located at the crossing of the arms in Figure 1.1.

Additionally to the major classes many (mostly small) galaxies show no distinctive morphology and are therefore classified as irregular galaxies.

Especially larger galaxies often host smaller satellite galaxies, as in case of the Milky Way the Large (LMC) and Small Magellanic Cloud (SMC), which have been accreted by the Milky Way quite recently and are parts of a still ongoing minor merger event (Pardy et al., 2018).

On larger scales galaxies tend to close ranks and form groups or clusters of various sizes, which represent the largest objects in the Universe. Interestingly, galaxies are neither homogeneously spread nor randomly, but form a web of filaments with large under-dense regions and large objects like clusters or groups at the junctions of these filaments.

The measurement of velocities of the almost virialised galaxy cluster members and the rotation velocities of stars in spiral galaxies lead to the first hints for the existence of dark matter (DM), because the amount of luminous mass observed in these objects is not enough to keep the member galaxies bound. Also the rotation curves in the outskirts of spiral galaxies are too fast to be explained only by the luminous mass of the galaxy, which therefore indicates additional mass (Rubin, 1991). Even though dark matter could not be directly measured till now, additional hints come from the structure of the Universe itself: In large astronomical surveys like the Sloan Digital Sky Survey (SDSS) (Kitaura et al., 2016) it can be seen that the amount of luminous matter is not sufficient to explain the observed density fluctuation in the Universe.

The light of galaxies at high distances, even though at rest, is red-shifted, which is a clear indicator for the expansion of the universe. This cosmological redshift  $z$  can be measured by comparing the emitted wavelength  $\lambda$  with the observed wavelength  $\lambda'$ .

$$z = \frac{\lambda'}{\lambda} - 1 = \frac{1}{a(t)} - 1 \quad (1.1)$$

The redshift can also be directly related to the scale factor  $a(t)$  of space at the time of the emission, through which the redshift is used as a position and also a time variable. This scale factor follows from the Friedmann-Lemaitre-equation, which assumes a homogenous and isotropic universe for which the distance dependency is given by:

$$H(t) = \frac{\dot{a}(t)}{a(t)} = H_0 \sqrt{\Omega_0 a(t)^{-3} + (1 - \Omega_0 - \Omega_\Lambda) a(t)^{-2} + \Omega_\Lambda} \quad (1.2)$$

$H(t)$  is called the Hubble rate and describes the expansion of the universe at any given time. For today  $t = t_0$  this value is equal to the Hubble constant  $H_0$  and the scale factor

is defined in a way that  $a(t_0) = 1$ .  $\Omega_0$  describes the density of matter in the universe, while  $\Omega_\Lambda$  introduces the cosmological constant. For different combinations of  $\Omega_0$  and  $\Omega_\Lambda$ , different geometries for the universe arise. If  $\Omega_0 + \Omega_\Lambda = 1$ , this leads to a flat universe, while  $\Omega_0 + \Omega_\Lambda < 1$  yields to an open, hyperbolic universe, and  $\Omega_0 + \Omega_\Lambda > 1$  would be a closed and elliptically shaped universe. Recent measurements show that the values for  $\Omega_0$  and  $\Omega_\Lambda$  combine to the critical value for a flat universe (Hinshaw et al., 2013; Planck Collaboration et al., 2016).

While spiral galaxies are the most common morphological type in the field, in more dense environments like clusters, elliptical and S0 galaxies dominate. This morphology-density relation (Figure 1.2, Dressler (1980)) is explained by interactions between galaxies and their accretion history. In general the formation of structure is a continual process, where galaxies increase their mass by the accretion of diffuse material and other galaxies. If this accretion process is slow or diffuse enough, a disc galaxy is able to preserve their morphology. While if the disc galaxy is merging with a galaxy of similar mass, the fluctuations in the gravitational potential and the tidal forces are strong enough to disrupt the disc and the stellar orbits are disordered. The result of this process is an elliptical galaxy. It is likely that intermediate-mass elliptical galaxies form in this way from binary mergers of Milky Way mass disc galaxies (Naab and Ostriker, 2009), but there is an alternative way to form elliptical galaxies by undergoing multiple minor merger (Naab et al., 2009).

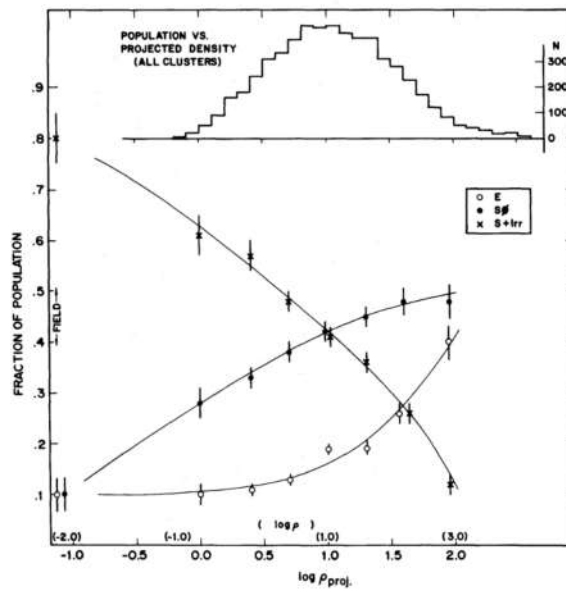


Figure 1.2: Original morphology-density relation by Dressler (1980)

This explanation outdated the initial belief that elliptical galaxies are evolving through monolithic collapse and evolve afterwards to a spiral galaxy. Nevertheless, elliptical galaxies are still called "early-type" galaxies and disc galaxies as "late-type" galaxies for historical reasons (Hubble, 1926, 1936).

## Numerical simulations

A very powerful tool in studying various kinds of physical processes are numerical simulations. The first numerical simulation started as an experiment by Holmberg (1941), using 74 light bulbs to simulate the merging of two galaxies. With increasing computational power, the number of particles increased and it became possible to use this method for many different aspects of astrophysics. From the formation of individual stars over the dynamics and evolution of galaxies up to large scale cosmology, where a whole "universe" is simulated, range now the fields in which numerical simulations are used to study the complex processes and connections in astrophysics. As an example, the dark matter only cosmological simulation DIANOGA (section 2.2) is displayed in Figure 1.3.

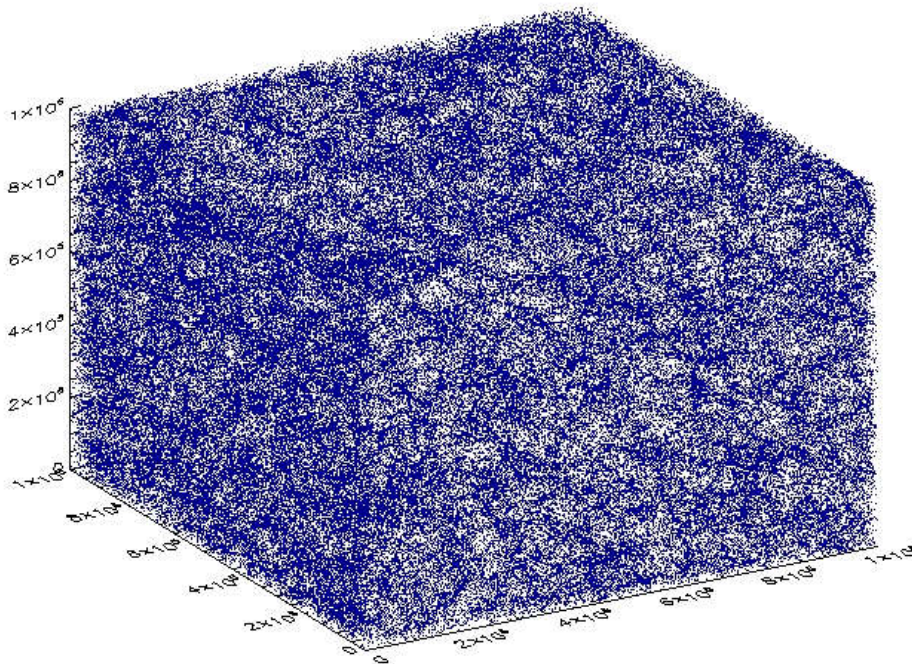


Figure 1.3: Full box of the cosmological simulation DIANOGA

In the common approach for galactic astrophysics, cold dark matter is described as an ideal collisionless fluid of particles, as for the most of the time the Universe is mainly dominated by gravity. This approach is the so-called cold dark matter approach (CDM), and the resulting N-body problem can be solved in two different ways: The most intuitive approach would be by solving this N-body problem by calculating the individual gravitational forces for each particle directly. Although this approach would result in the exact Newtonian potential, it is computationally very expensive, due to its runtime  $t$  scaling  $t \propto N^2$  with particle number  $N$ . The second way is by solving the resulting Poisson equation and

the therefore resulting hydrodynamical differential equations. For this hydrodynamical approach two different techniques are used. These techniques are based on the two different kinds of hydrodynamical formulations: The first is the Eulerian approach, which divides the fluid into individual spatial fixed grid cells and solves the fluid equations for each grid cell, which is later on treated as a grid-point containing all the information of its cell. In this method the coordinate system is fixed as the fluid is moving through it. The other approach of solving the hydrodynamical equations is by using the Lagrangian formulation of hydrodynamics. In this formulation the fluid itself is divided into a set of particles and all equations are solved by averaging over the nearest neighbors of this particle, while the coordinate system in this method moves with the particles. This so called "smoothing" allocates every particle a scalar of the calculated property and through this the partial differential equations reduce to ordinary differential equations, which can be then solved more easily and reduces the computational time to  $t \propto N \log N$ . Due to the smoothing the method is called smoothed particle hydrodynamics (SPH), and is our method of choice for all simulations used in this thesis.



## 2. Zoom-simulations of compact galaxy groups

### 2.1 Hickson compact groups

More than 50 % of all galaxies live within galaxy groups. Compact galaxy groups are a special case of galaxy groups, which are rather small and isolated groups where their members are in close proximity to each other. The probably most famous example for a compact galaxy group is Stephans Quintett (Figure 2.1) in the constellation of Pegasus. It has been detected at first by Edouard Jean-Marie Stephan in 1877, who initially thought to observe nebulae.



Figure 2.1: Stephans Quintett observed by the Hubble Space Telescope (HubbleSite).

### 2.1.1 Classification

In order to distinguish common galaxy groups (further called loose groups) from compact groups, Hickson (1982) defined three criteria which a group has to satisfy to become a compact galaxy group. These groups are accordingly called Hickson compact groups (HCG).

The first criteria states that a compact group has to consist of a minimum of four galaxies, which differ by a maximum of  $3.0mag$  in the optical waveband; typically HCGs consist of four to five members. In addition, these galaxies have to have a minimum mean surface brightness of  $\bar{\mu}_G < 26$  in the optical, which is calculated by measuring the flux over the smallest enclosing circle  $\theta_N$  containing all geometrical centers of the member galaxies. This compactness criterion is to first order distance independent. An isolation criterion is used in order to exclude cores of clusters. A group gets rejected if, within three radii of the smallest enclosing circle  $\theta_G$ , another non-member galaxy within a magnitude  $3mag$  of the brightest galaxy occurs. The three criteria can be summarized as:

- 1)  $N \geq 4$  (member criteria)
- 2)  $\theta_N \geq 3\theta_G$  (isolation criteria)
- 3)  $\bar{\mu}_G < 26.0$  (density criteria)

Alternatively, the classification of compact groups is done by using redshift information. This procedure, firstly done by Humason et al. (1956), defines a compact group by the following criteria: The member galaxies are only allowed to have a minimum separation of  $50h^{-1}kpc$  in projection and a maximum velocity difference of  $1000km/s$ . The numerical values here were chosen in order to match the results to the characteristics of the HCGs. Even though this method is more effective in finding compact groups and its automatic elimination of foreground and background galaxies, it allows due to its more generous isolation criterion the inclusion of more groups. This would lead to the classification of compact groups, which are less isolated and therefore less distinct.

A larger bias - which applies to both methods - occurs due to the geometrical orientation of the group. Most non-spherical systems would preferably be defined as a compact group if their most eccentric axis is along the line of sight, rather than if not. The orientation of for example a prolate system is therefore strongly influencing its classification, because only the projected density is taken into account. The velocity measurement of the second method only removes interlopers, and therefore compliments the HCG angular-selection criteria.

### 2.1.2 Space distribution, dynamical properties and structure

HCGs have a median redshift of  $z = 0.30$  (Hickson, 1997) and are therefore much farther away than the center of the local supercluster, of which the Milky Way is part of. In addition, HCGs are mostly uniformly distributed but tend to follow large scale structures like filaments, and are also connected to loose groups (Rood and Struble, 1994).



Even though HCGs are connected to loose groups, HCGs have a much smaller fraction of late-type galaxies than loose groups. Their velocity distribution, nevertheless, which follows a Gaussian distribution with a standard deviation of  $\sigma \approx 250 \text{ km/s}$ , is similar to loose groups, but much smaller than the distribution of rich clusters. By using the velocity distribution a characteristic density can be calculated, from which it can be shown that HCGs have mean total mass-to-light ratio of  $50 M_{\odot}/L_{\odot}$  (Hickson et al., 1992) in solar units. For individual galaxies (Rubin et al., 1991) found the mass-to-light ratio to be  $7 M_{\odot}/L_{\odot}$  which suggests that only  $\approx 15 \%$  of mass are stored in the galaxies itself, while the rest consists of gas and dark matter.

HCGs have a centrally concentrated surface density profile, consisting of stripped stars accumulating in the potential well of the group, which connects all member galaxies (Da Rocha et al., 2008), like it can be seen in galaxy clusters as well. HCGs also tend to lack in cold gas compared to loose groups, which is consistent with a similar deficit in continuum radio emissions (Menon, 1995), and indicates that the cold gas has been removed from the galaxies due to interactions. It has also been shown that gas in HCGs is not bound to the galaxies (Williams and van Gorkom, 1988; Williams et al., 1991), and is even distributed over all members of the HCG. These observations indicate that compact groups are physically dense objects and no projection effects or coincidental alignments in loose groups.

The morphological types of HCG galaxies show a much higher fraction of early-type galaxies than for field galaxies. This supports the standard idea of the formation of early-type galaxies by major merging, which had to take place in such dense environment as a HCG. To mention is that a HCG with a higher velocity dispersion, which suppresses the merging rate, therefore tend to have lower amounts of early-type galaxies than HCGs with lower velocity dispersion. Another strong support for high interaction rates between member galaxies is that up to  $\approx 66 \%$  (Rubin et al., 1991) of HCGs spiral galaxies show peculiar rotation curves and various kinds of irregularities and asymmetries.

HCG disc galaxies in addition typically show less nonthermal continuum emission than isolated disc galaxies. This is mainly due to lower star formation in comparison. But meanwhile, if considering the central region only, significantly higher nonthermal nuclear emissions are observed, which can occur due to star formation and active galactic nuclei (AGN). These emissions have to be feed by large amounts of gas and the emission distribution is consistent with galaxy interactions. These interactions remove gas from the outer regions of the galaxy, while fueling the inner regions with gas, which results in higher star formation rates in the inner regions and the possibility of fueling an AGN.

### 2.1.3 Formation and evolution

The formation process of compact groups is still under discussion. The idea of merging activity in compact groups, with continuous in-fall from the environment (Governato et al., 1996), is favored because it explains the observed differences in morphological types of the member galaxies. In this model galaxy mergers should occur on a regular basis and it has been observed that up to  $25 \%$  of all galaxies in compact groups show signatures of mergers

(Hickson, 1997), if a more generous way of applying certain conditions is used. But due to small number statistics, a significant amount of merging in HCGs can't be determined. Nonetheless, in detailed studies of individual galaxies in many cases clear indications for galaxy-galaxy interactions occur.

It can be therefore concluded that compact groups only have a limited lifetime. The typical lifetime  $t_{HCG}$  of a group is expected to be a magnitude higher than its dynamical timescale (e.g. Barnes (1985)) which yields to  $t_{HCG} \approx 0.2 H_0^{-1}$ . This leads to the conclusion that compact groups have steadily reproduced and a large population of compact group remnants have to exist.



Figure 2.2: Visualization of the simulated compact group Bofur 0 using the visualization software SPLOTCH (Dolag et al., 2008).

The remnant of a compact galaxy group is believed to be a massive isolated elliptical, due to the arguments presented by numerical simulations that multiple and major mergers lead to the formation of elliptical galaxies. But this idea leads to some difficulties, because for example the luminosities of massive isolated elliptical are usually only of  $\sim 20$  to  $30$  % compared to the luminosities of compact groups. Even if galaxy-galaxy interactions boost the star formation rate in compact groups, this amount would not be sufficient to explain these differences. It is therefore not clear if elliptical field galaxies are the remnants of compact galaxy groups.

It is obvious that compact groups are very important and very interesting objects. They offer a great general framework to study dynamical evolution and shapes of galaxies like their kinematics and morphology with respect to interactions. In addition the study of processes which trigger many different processes like starbursts, star formation in general, AGNs and nuclear activity makes compact groups highly interesting objects. And still there are many questions unanswered like their lifetime, their end-products, their influence on galaxy evolution and their fit into the overall structure hierarchy.

## 2.2 Simulations

The starting point for all further simulations is the DIANOGA simulation. The DIANOGA simulation is a standard WMAP-7  $\Lambda$ CDM universe with a cosmological parameter  $\Omega_\Lambda = 0,76$ , a matter density parameter of  $\Omega_m = 0.24$ , a baryon fraction of  $\Omega_{bar} = 0.04$  and a Hubble parameter of  $h = 0.72$ . The simulation is a dark matter only simulation of a huge periodic  $1h^{-1}Gpc$  box-size containing  $1024^3$  particles with an individual mass of  $M_{dm} = 6.62 \times 10^{10} h^{-1}M_\odot$ . It has been performed with the N-body/SPH Code GADGET 3 (Springel et al., 2001; Springel, 2005). As an impression the full box of this simulation could be seen in Figure 1.3. The procedure of the re-simulations is done by using the example described by Schlachtenberger (2014).

### 2.2.1 Objects

In order to find compact galaxy groups we looked at the DIANOGA simulation at  $z = 0$ . With the halo-finder SUBFIND (Springel et al., 2001), which is integrated in GADGET (Springel, 2005), we excluded heavy clusters and low-mass galaxies by setting a mass-limit between  $1 \times 10^{13} h^{-1}M_\odot < M < 1 \times 10^{14} h^{-1}M_\odot$ . Also heavy individual galaxies were excluded by selecting only halos with a minimum of 4 sub-halos. This still leads to numerous possible objects. Therefore these halos were sorted by their distance to the next cluster ( $M > 1 \times 10^{14} h^{-1}M_\odot$ ) and next group sized halo with a similar mass of  $1 \times 10^{14} h^{-1}M_\odot > M > 1 \times 10^{13} h^{-1}M_\odot$ . The distances for each object can be seen in Figure 2.3.

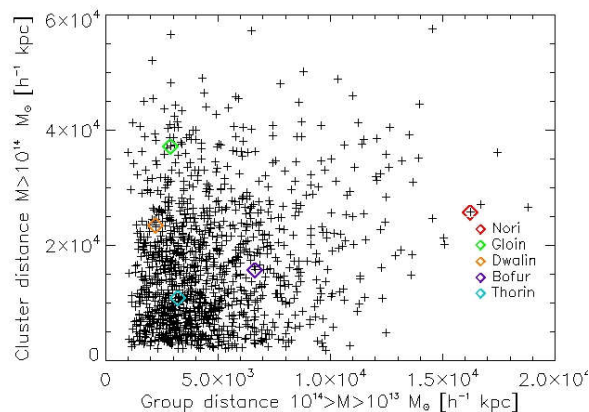


Figure 2.3: Additional halo selection criteria. The minimum distances to the next cluster and next group are displayed as the axis intercepts. The diamonds display the position of the final objects.

This ensures that the targeted object is dominating its environment. From this final list, a few objects were chosen. As a final step objects with a maximum number of sub-

halos with similar masses were preferred. The final objects which proved themselves as interesting after the first tests and were executed further on are listed here:

object name	mass [ $10^{10} h^{-1} M_{\odot}$ ]	$r_{vir}$ [ $h^{-1} kpc$ ]	color in Figure 2.3
Gloin	2940.04	648.305	green
Nori	2995.86	652.39	red
Bofur	4056.51	721.73	purple
Dwalin	4310.81	736.50	orange
Thorin	4317.01	736.88	turquoise

Table 2.1: Main parameters of the chosen objects from the parent simulation DIANOGA.

In Figure 2.4 the larger environment of the selected objects is shown. It can be seen that the larger objects like Thorin and Dwalin are close to crossing of larger filaments and Bofur is also sitting in a mayor filament as well as Gloin. At a first inspection Nori already stands out, because it is not part of a mayor structure, but it is in a region very distant from any larger object inside a very thin filament which could have already been seen in Figure 2.3. In Figure 2.5 it can also be seen that Nori sits in a low density environment, as well as Gloin, while all other objects have a denser environment.

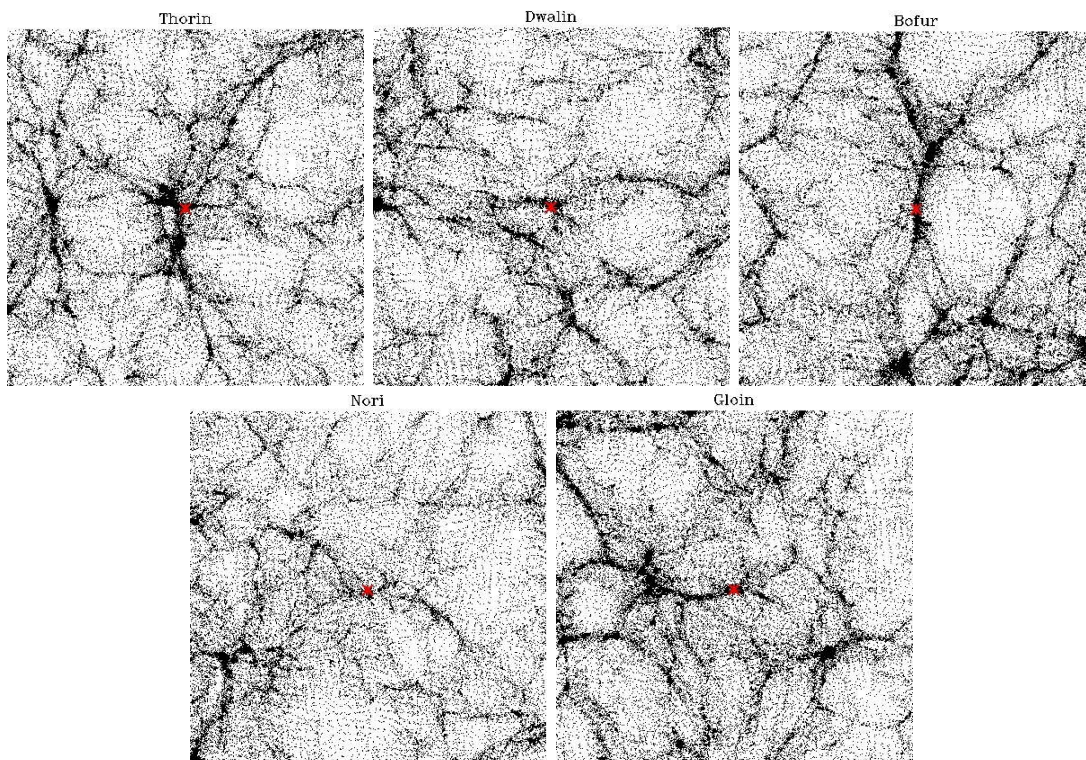


Figure 2.4: Environment of all objects in the DIANOGA simulation with an axis length of  $1 \times 10^5 h^{-1} Mpc$  at  $z = 0$ .

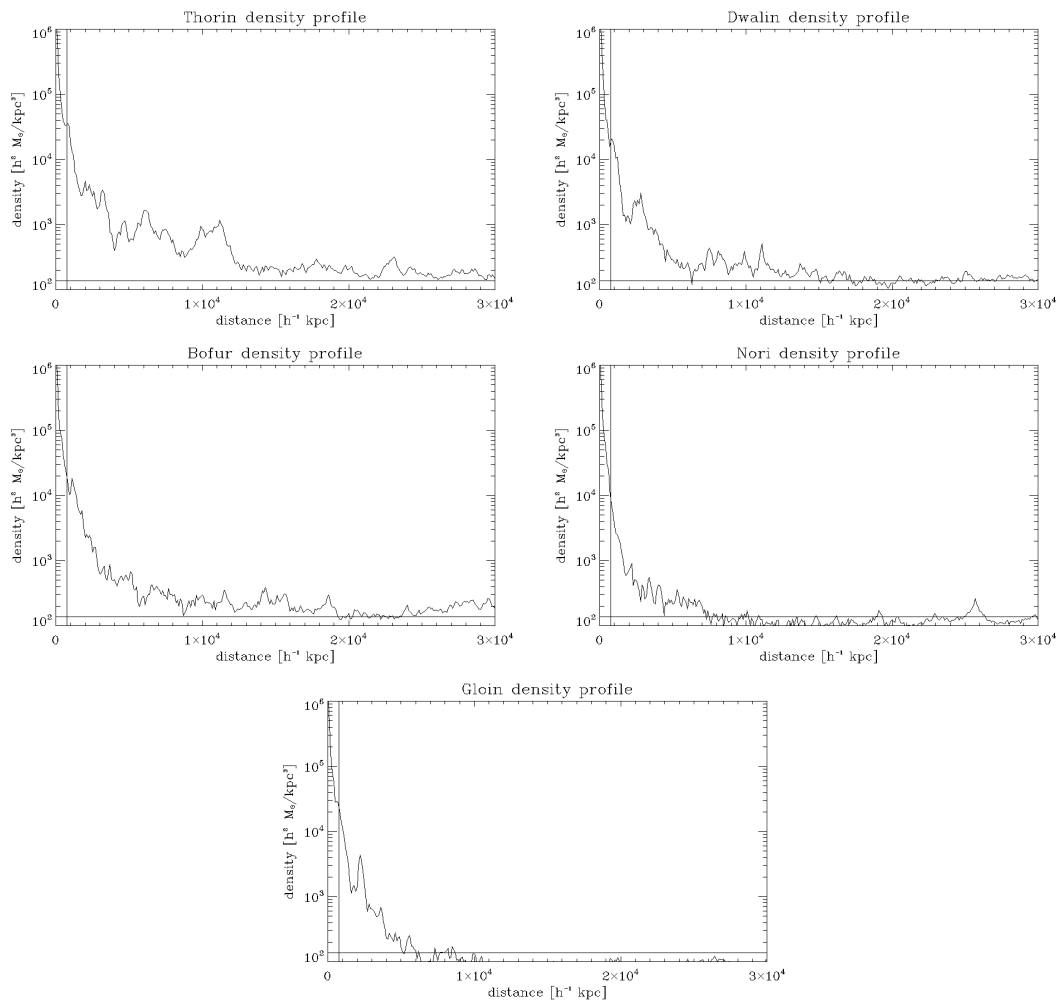


Figure 2.5: Density of the environment around all objects, the horizontal line represents the mean density in DIANOGA and the vertical line the size ( $r_{vir}$ ) of the objects.

### 2.2.2 Tracking

After choosing the object at  $z = 0$  we have to track the individual particles back in time in order to find their original position in the box. Here it is important to distinguish between particles which are a part of the final object, and therefore have a major impact on the formation, and all other particles which only influence the object by large range forces. As a first guess we are taking all particles in a certain sphere  $r_{sp}$  around the final object to be classified as particles of the object. As trace radii of the sphere values of  $r_{sp} \sim 7 h^{-1} Mpc$ , roughly 10 times the virial radius of the object are chosen. Here we are including a rather large area to prevent disturbances through low-resolution particles. This is essential to avoid unphysical potential minimums and therefore unphysical structure formation due to an artificial seed-particle.



After the first re-simulation of the object for the further simulations the prior approach is replaced by tracking the selected individual particles individually back to their origin. This procedure by Tormen et al. (1997) creates a Lagrangian Volume, our high-resolution region, which is enclosed by a low-resolution cube. The shape of this region is displayed by mapping the particles into a 3D  $16^3$  grid. In figure 2.6 a slice through the resulting Lagrangian region, containing the high-resolution particles (blue) and a buffer zone around (red) is displayed. Depending on the result of this tracing it has sometimes been necessary to modify the resulting Lagrangian region to avoid small holes, extend, or consolidate the region. A further consolidation has been successful in some cases in order to reduce the amount of high-resolution particles and therefore the amount of computational time. But due to the huge zone of attraction of the chosen objects it had to be done with caution.

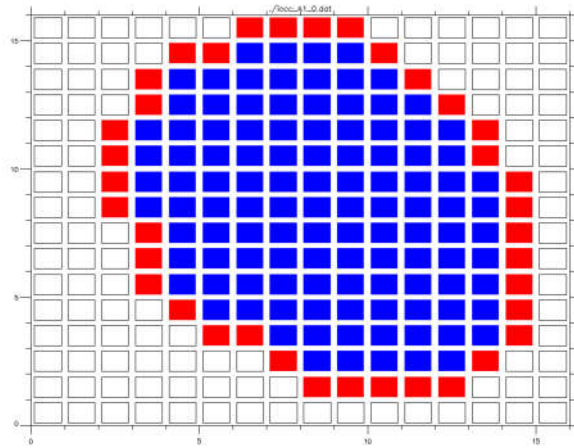


Figure 2.6: Slice of the iocc-region mapped on a 3D  $16^3$  grid. The blue boxes represent high-resolution regions, while the red boxes are a puffer zone to the low resolution region.

### 2.2.3 Initial conditions

After each tracking new initial conditions are required. This is done for our newly created Lagrangian region by using the Zoomed Initial Conditions (ZIC) technique by Tormen et al. (1997). This technique creates a sphere of particles with the same mass as the original simulation on a grid, which are responsible for the creation of the local force field. On the outside of this sphere the amount of particles is minimized. As long as the angular distribution is maintained these particles describe the long range tidal forces. In the center of this sphere, the high resolution region, particles with a higher mass resolution are put on a regular grid. In the left panel of Figure 2.7 the total initial conditions are displayed. The red center corresponds to the high-resolution region. Here it can be seen very clearly how the amount of low-resolution particles declines with larger distances to the high-resolution region. In the second panel of Figure 2.7 the different layers can be seen very clearly, a grid-like sphere of low-resolution particles, high resolution dark matter region and gas

distribution (red).

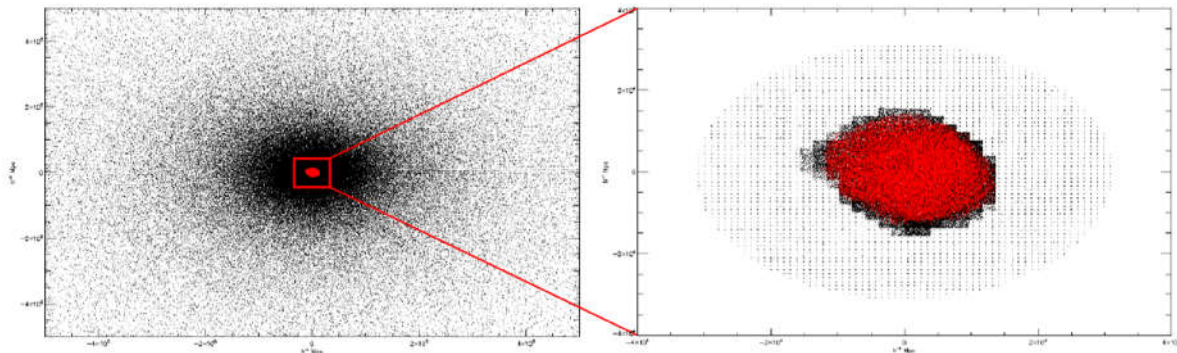


Figure 2.7: a) Initial conditions produced with the ZIC method, here the red part displays the high-resolution region. b) Central view of the initial conditions with gas component (red).

This idealized distribution, which has inclining mass per particle from the center to the outside, gets disturbed by the disturbances of the initial simulation. By introducing perturbations with smaller wavelengths (Bonafede et al., 2011) the same cosmological conditions are created, this time with higher resolution.

### 2.2.4 Re-simulating

At first a gravitational dominated dark matter only simulation is performed to check for uncontaminated initial conditions. Here we required a clean area around the object at all redshifts of at least  $r_c \geq 7 \times r_{200}$ , which can be seen in Figure 2.8. In case of a low resolution intruder we had to increase the high-resolution box until we achieve a sufficiently large clean region again.

After having successfully cleaned the object, the particles were re-tracked again and new ICs are created. But now gas particles were introduced to the ICs by splitting up the high resolution DM particles and converting them into gas and DM particles. The new particles are then arranged in a way to conserve the momentum and center of mass of the initial particle. In the right panel of Figure 2.7 the resulting high resolution region can be seen. It can also be seen that the DM region has a buffer region between the low resolution region and the gas region.

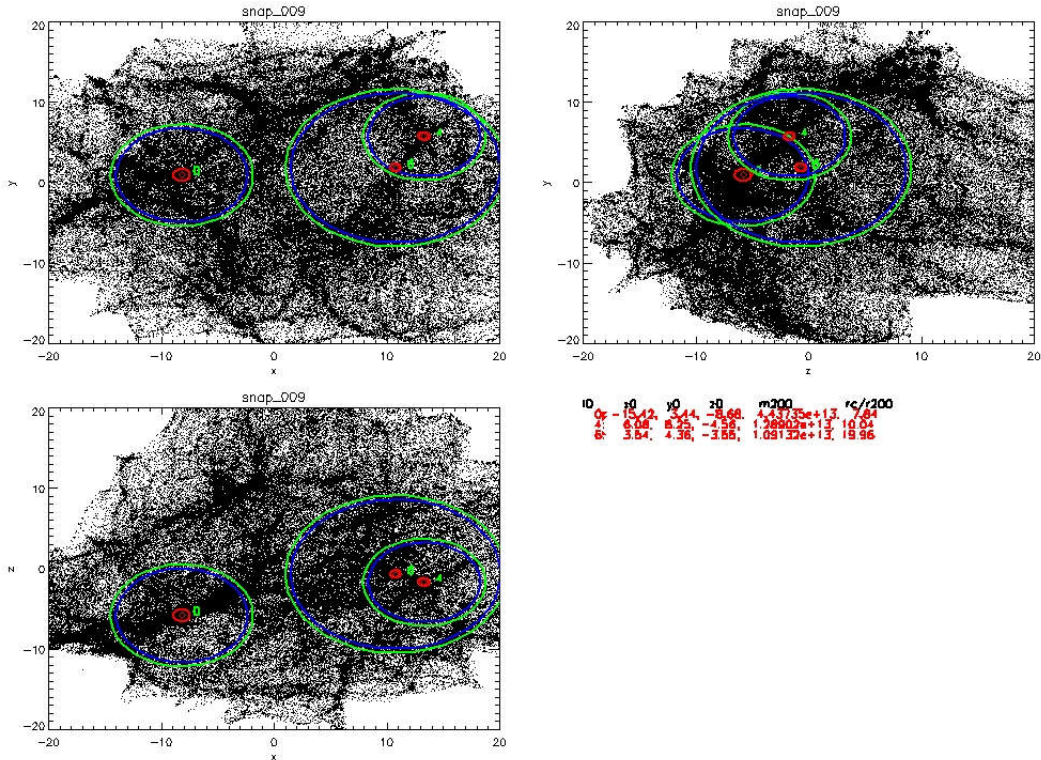
For the re-simulations different resolution steps were used, which are similar to the resolutions used in the Magneticum Pathfinder simulations (Remus et al., 2017). While the first step is only performed with DM-only, all other simulation steps were at first performed as DM-only and gas was included afterwards in a separate simulation. The different resolutions are listed in Table 2.2.

For each resolution step the newly created initial conditions are simulated with the newest version of the cosmological TreePM SPH code GADGET-3, which is a subsequent

resolution	Magneticum Pathfinder equivalent	DM particle mass [ $h^{-1}M_{\odot}$ ]	gas particle mass [ $h^{-1}M_{\odot}$ ]
1x	(high resolution (HR))	$1 \times 10^9$	—
10x		$1 \times 10^8$	$1.6 \times 10^7$
25x	(ultra high resolution (UHR))	$4 \times 10^7$	$6.2 \times 10^6$
250x		$4 \times 10^6$	$6.2 \times 10^5$

Table 2.2: Resolution steps with corresponding particle mass.

version of the GADGET-2 (Springel, 2005) code. A state of the art SPH implementation as presented by Beck et al. (2016) is used to overcome known weaknesses of the SPH formalism (i.e. Agertz et al. (2007)), and a Wendland C6 kernel is used. In addition we use time depended artificial viscosity and conduction to enhance the properties of SPH in terms of shock capturing and particle noise reduction. Furthermore complex physics are used like radiative cooling (Katz et al., 1996) and star formation (Springel and Hernquist, 2003) following the Salpeter (1955) initial mass function (IMF) and stellar winds. Further black hole seeding and supernova feedback is enabled as well.

Figure 2.8: Dark matter only run of Thorin (halo 0) at  $z = 0$ , showing all clean halos with  $M > 1 \times 10^{13} h^{-1}M_{\odot}$ , the green/blue circles display the clean area.



## 2.3 Smallest enclosing circle

In order to check for the compact group criteria it is necessary to find the smallest enclosing circle of all possible group members. In all simulations an object has to have at least  $2 \times 10^{10} h^{-1} M_{\odot}$  in total mass and a black hole inside of  $10 h^{-1} kpc$  from the center, which is a quite large value due to difficulties with the black hole model, to be considered as a galaxy (see Bittner (2018)). A first approach by using the center of the halo group provided by SUBFIND or by calculating the center of mass will lead to fast and already quite good results; but it will result in to high uncertainties. To find the smallest enclosing circle and to be sure it is the smallest one, a few possible methods can be used.

The easiest way would be by testing if all pairs of points  $(P_i, P_j)$ , with a circle of diameter from  $P_i$  to  $P_j$ , contain all other points. In addition, a testing for all triplets of points can be done and again it can be checked if the perimeter contains all points. And from all these circles then the smallest one is chosen. This brute-force-method would work in general, but it would be unnecessary time consuming and inelegant.

Therefore, the quite simple but efficient algorithm by Skyum (1991), which runs with a runtime of  $O(n \log n)$  was computed. This algorithm consist of two parts, first the determination of the convex hull and then the algorithm itself.

### 2.3.1 Convex hull

The convex hull is the smallest set of  $N$  points  $X = P_0, P_1, P_2, \dots, P_N$  in the Euclidean plane  $V$ , which contains all points. It is defined as the intersection of all convex superset of  $X$ , itself is convex as well and therefore the smallest hull which contains  $X$ .

$$\text{conv}X = \bigcap_{X \subseteq K \subseteq V} K \quad ; K \text{ convex} \quad (2.1)$$

There are a number of algorithms known for computing the complex hull for a finite set of points. Here the Graham scan algorithm (Graham, 1972) - although it is not the simplest method, but a quite efficient algorithm with a runtime of  $O(n \log(n))$  - was chosen.

For this algorithm the first step is to find a point which definitely is a member of the convex hull. Therefore, one searches for the point with the smallest ordinate  $P_0$ . If there are two or more points which share the smallest ordinate the one with the smallest abscissa is chosen. After finding the starting point, all other points are sorted anticlockwise by increasing angle between  $P_0 \rightarrow P_i$  and the unit vector  $\vec{e}_x$ . This is done by computing the angle between two vectors. If two or more points share the same angle, and are therefore colinear with  $P_0$ , only the point with the largest distance to  $P_0$  is kept. All other are removed from the sample, because they can't be a turning point of the convex hull. This can be seen for an example point set in the left panel of Figure 2.9 for the points  $P_1$  and  $P_{12}$  which will be excluded already at the first step of the algorithm.

For  $X$  being now our sorted point set, all points are checked to find the turning points of the convex hull. In the beginning the starting point  $P_i = P_0$  and the following point

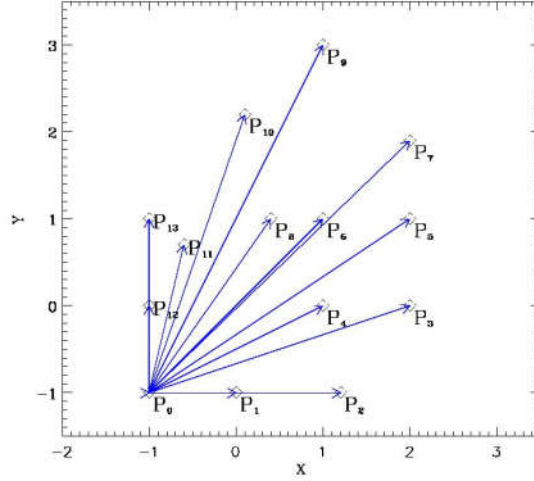


Figure 2.9: Vectors from the starting point ( $P_0$ ) to all other points of an example point set.

$P_{i+1} = P_1$  are considered as turning points. Now the next point  $P_{i+2} = P_2$  is added and it is determined, if by traveling from  $P_i \rightarrow P_{i+1} \rightarrow P_{i+2}$  it is doing a right- or left-turn. This task is solved by calculating the determinant  $\det T(P_i, P_{i+1}, P_{i+2})$ .

$$\det T(P_i, P_{i+1}, P_{i+2}) = \begin{vmatrix} 1 & x_i & y_i \\ 1 & x_{i+1} & y_{i+1} \\ 1 & x_{i+2} & y_{i+2} \end{vmatrix} = \begin{vmatrix} x_{i+1} - x_i & y_{i+1} - y_i \\ x_{i+2} - x_i & y_{i+2} - y_i \end{vmatrix} \quad (2.2)$$

$$= (x_{i+1} - x_i) \times (y_{i+2} - y_i) - (x_{i+2} - x_i) \times (y_{i+1} - y_i) \quad (2.3)$$

$$\det T(P_i, P_{i+1}, P_{i+2}) = \begin{cases} < 0, & \text{if } P_{i+2} \text{ is on the right side of } \overrightarrow{P_i P_{i+1}} \\ = 0, & \text{if } P_{i+2} \text{ lies on } \overrightarrow{P_i P_{i+1}} \\ > 0, & \text{if } P_{i+2} \text{ is on the left side of } \overrightarrow{P_i P_{i+1}} \end{cases} \quad (2.4)$$

Due to the initial sorting the first three points are always going left and every additional point is also, due to construction, always expanding the hull. By including more and more points it is possible that old points are now lying inside the new hull. This is the case if the curve is doing a right-turn. Now the second point of the considered points has to lie inside of the convex hull, to perform this turn and is therefore removed from  $X$ . This procedure is done for a full loop over all points after which the convex hull is determined.

The resulting convex hull for the example point set is displayed in Figure 2.10.

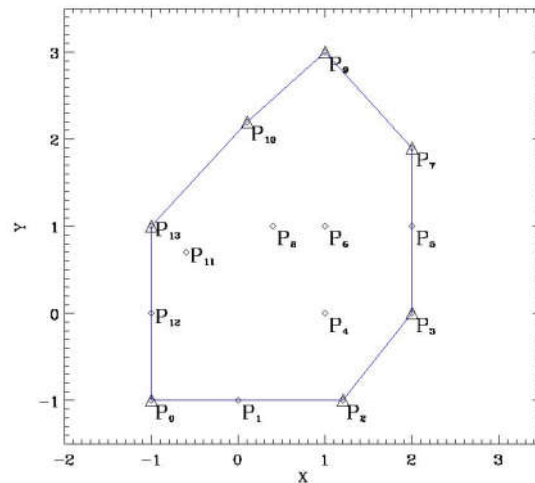


Figure 2.10: The resulting convex hull with its defining points  $P_0, P_2, P_3, P_5, P_6, P_9, P_{11}$  and  $P_{13}$  marked by triangles.

### Pseudocode of the computed Graham Scan:

**Algorithm:** Graham Scan

Input: point set  $X$

Output: points defining the convex hull of  $X$

**Begin:** Function

Find  $P_0$

Sorting the angles  $\sphericalangle(X, P_0, e_x)$

$n$  = number of points in  $X$

**Begin:** Loop: For  $i=0$  to  $i=n$  begin

$P_i, P_{i+1}, P_{i+2}$

calculate  $\det T(P_i, P_{i+1}, P_{i+2})$

If  $\det T \leq 0$  then remove  $P_{i+1}$

$i = i+1$

**End:** Loop

Return points defining convex hull

**End:** Function

### 2.3.2 Skyum algorithm

For the algorithm by Skyum (1991) we start with the points which define the convex-hull of our point set. These points  $S = P_1, P_2, \dots, P_n$  in the Euclidian plane  $R^2$  define a convex polygon and are sorted in this case anticlockwise but it can also be done clockwise. As a first step the circumcircle of three subsequent points  $\circ(P_{i-1}, P_i, P_{i+1})$  for all points is calculated. The resulting circumcircles can be seen in panel a) of Figure 2.11. This circumsphere for three non-collinear points is always defined and the radius  $r$  can be calculated by using the distances  $d$ :

$$r = \frac{d(P_{i-1}, P_i) \times d(P_i, P_{i+1}) \times d(P_{i+1}, P_{i-1})}{2 \times |\det(P_{i-1}, P_i, P_{i+1})|} \quad (2.5)$$

In the special case of two equal points, half the distance between these and the third points is denoted as the radii. Also the coordinates of the circle center  $(x_m, y_m)$  are calculated in this process:

$$x_m = \frac{1}{2} \times \frac{(x_{i-1}^2 + y_{i-1}^2)(y_i^2 - y_{i+1}^2) + (x_i^2 + y_i^2)(y_{i+1}^2 - y_{i-1}^2) + (x_{i+1}^2 + y_{i+1}^2)(y_{i-1}^2 - y_i^2)}{y_{i-1}(x_{i+1} - x_i) + y_i(x_{i-1} - x_{i+1}) + y_{i+1}(x_i - x_{i-1})} \quad (2.6)$$

$$y_m = \frac{1}{2} \times \frac{(x_{i-1}^2 + y_{i-1}^2)(x_i^2 - x_{i+1}^2) + (x_i^2 + y_i^2)(x_{i+1}^2 - x_{i-1}^2) + (x_{i+1}^2 + y_{i+1}^2)(x_{i-1}^2 - x_i^2)}{y_{i-1}(x_{i+1} - x_i) + y_i(x_{i-1} - x_{i+1}) + y_{i+1}(x_i - x_{i-1})} \quad (2.7)$$

In order to terminate the algorithm the angle of the largest circumcircle has to be  $\angle(P_{i-1}, P_i, P_{i+1}) \leq 90^\circ$ . The calculation of the angle can be done as usual:

$$\angle(P_{i-1}, P_i, P_{i+1}) = \arccos \frac{d^2(P_{i-1}, P_i) + d^2(P_i, P_{i+1}) - d^2(P_{i+1}, P_{i-1})}{2 \times d(P_{i-1}, P_i) \times d(P_i, P_{i+1})}$$

But this calculation is on the one hand side quite expensive and as well lacks in accuracy. Furthermore the angle itself is not important, only if it is larger than  $90^\circ$  and therefore a simplified criteria is used:

$$W_{P_{i-1}, P_i, P_{i+1}} = d^2(P_{i-1}, P_i) + d^2(P_i, P_{i+1}) - d^2(P_{i+1}, P_{i-1}) \quad (2.8)$$

$$\angle(P_{i-1}, P_i, P_{i+1}) \leq 90^\circ \iff W_{P_{i-1}, P_i, P_{i+1}} \geq 0 \quad (2.9)$$

If the angle and therefore the point  $P_i$  doesn't satisfy this criteria, it is excluded from  $S$  and the circumcircles are recalculated. This is done as long, till  $\angle(P_{i-1}, P_i, P_{i+1}) \leq 90^\circ$  and the smallest circle is found or  $|S| = 2$ , in which the smallest circle would also be found. The speed of the algorithm yields from the way of recalculating the circumcircles.  $S$  contains the set of circles  $\circ(P_0, P_1, P_2), \dots, \circ(P_n, P_0, P_1)$ . If  $\angle(P_{i-1}, P_i, P_{i+1})$  of the largest circumcircle  $\circ(P_{i-1}, P_i, P_{i+1})$  is  $\angle(P_{i-1}, P_i, P_{i+1}) > 90^\circ$  then  $P_i$  gets removed.

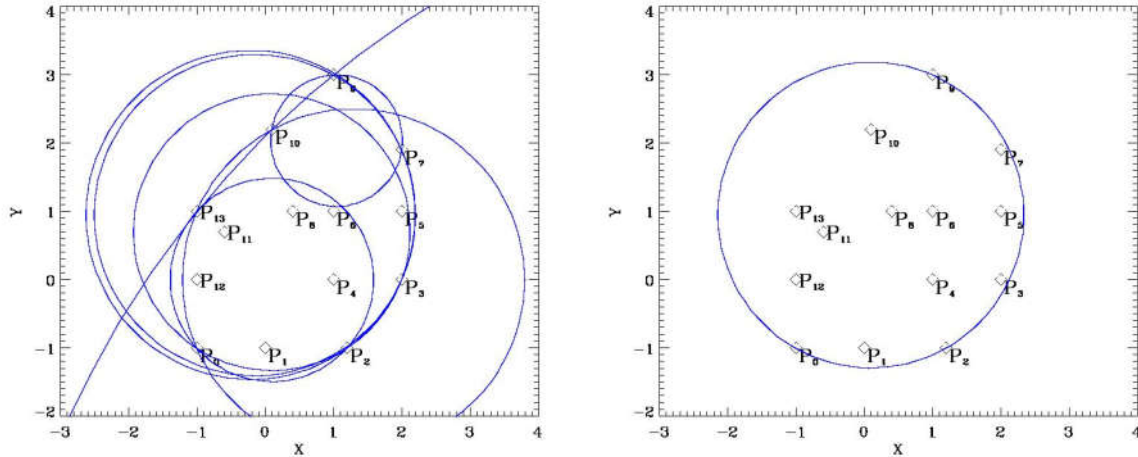


Figure 2.11: a) All circumcircles defined by three point for  $S$ . b) the smallest enclosing circle.

Now instead of recalculating all circumcircles only two new circumcircles, which consist of points which are now subsequent to each other,  $\circ(P_{i-2}, P_{i-1}, P_{i+1})$  and  $\circ(P_{i-1}, P_{i+1}, P_{i+2})$ , are recalculated.

**Pseudocode of the computed Skyum algorithm:**

**Algorithm:** Skyum

Input: sorted point set  $S$ , which are defining a convex polygon

Output: smallest enclosing circle of  $S$

**Begin:** Function

Calculating all possible circumcircles for subsequent points

**Begin:** Loop:

find  $P_i$  for which:  $\max(\circ(P_{i-1}, P_i, P_{i+1}))$

**if**  $\angle(P_{i-1}, P_i, P_{i+1}) > 90^\circ$  **then**

remove  $P_i$  and all its corresponding circumcircles

recalculate  $\circ(P_{i-2}, P_{i-1}, P_{i+1})$  and  $\circ(P_{i-1}, P_{i+1}, P_{i+2})$

**else finish**

**End:** Loop:

Return parameters of smallest enclosing circle

**End:** Function

## 2.4 Results

### 2.4.1 Resolution limitation and mass loss

At reaching the UHR (25x) resolution step, some inconsistencies were found. By taking a closer look to the galaxies of our group members, and especially for the low mass galaxies, it has been found that there are cases where the only black hole in a certain galaxy is orbiting the gravitational center of its galaxy at distances of up to disc size. This contradicts common knowledge, where the center of the galaxy should harbor a massive black hole. This effect is displayed in Figure 2.12 for a galaxy in the object Dwalin 0 at  $z = 0$ . The object is a small satellite galaxy of the group and currently making its way towards it. It can be seen clearly that the black hole isn't in the center of its host galaxy but almost at the end of the galaxy.

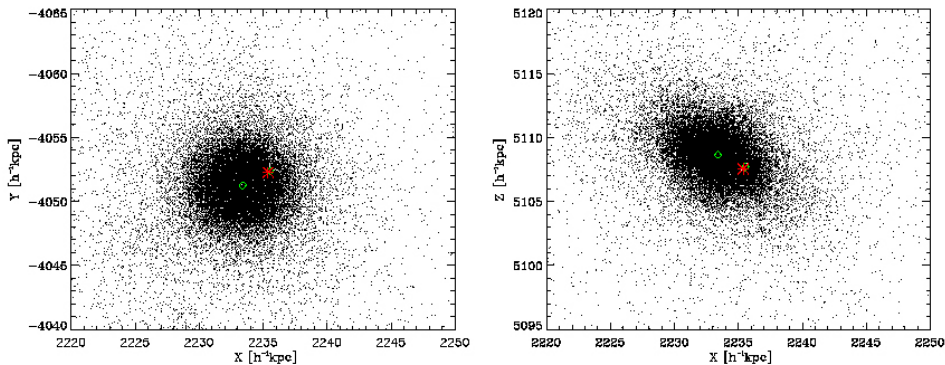


Figure 2.12: Offset of the blackhole (red star) from the center of the galaxy, for this example a sub-halo of the object Dwalin 0 at 25x and  $z = 0$  is shown. The green diamond is the position of the sub-halos found by SUBFIND and marks the gravitational center of the galaxy and its sub-halo.

The source for this behavior lies in the implementation of black hole physics into the code because in these simulations the black hole is not fixed to the minimum potential like it is done in most simulations. Due to numerical fluctuations the black hole was able to detach from the center of the galaxy and move. This effect is influencing the stellar distribution aside the center of the galaxies which it shouldn't. Also the merging timescales changed and the black holes were introducing additional turbulence. This behavior and possible solutions were studied in detail by Bittner (2018).

These cases have been found in UHR too often, thus a further increase in resolution therefore was not reasonable. A fully functionally solution for this problem has not been found in time, hence the resolution was limited to UHR for all simulations. The reason

object	initial mass (DIANOGA) [ $10^{10} h^{-1} M_{\odot}$ ]	mass at 10x [ $10^{10} h^{-1} M_{\odot}$ ]	mass at UHR (25x) [ $10^{10} h^{-1} M_{\odot}$ ]
Thorin 0	4317.01	4022.22	—
Dwalin 0	4310.81	1871.98	1424.13
Bofur 0	4056.51	2126.73	2626.72
Nori 0	2995.86	356.36	329.65
Gloin 0	2940.04	2116.03	—

Table 2.3: Masses of the largest halos at  $z = 0$  for all objects at the individual resolution steps with gas.

for for the maximum resolution for Thorin and Gloin being 10x is in the case of Gloin that it didn't fulfill the group criteria in 10x and it is therefore not expected to do this in higher resolution. Thorin on the other hand is large object and therefore computationally expensive to run. This was avoided to be done without a proper implementation of the black hole physics. During the simulations with each resolution step the objects lost weight. This lead to a decrease of a factor of almost 10 in the extreme case of Nori from the DIANOGA halo to UHR. Through this the halos in Nori fell out of the group mass range, but remained at Milky Way sized halos which was the reason why they were kept running up to UHR in order to give additional objects for the study of spiral galaxies in cosmological zoom-simulations by Bittner (2018). Unfortunately these objects were not run at higher resolutions then UHR and were also not used in this study due to the complexity of the black hole physics.

The masses for the main halo for each object from DIANOGA to its final resolution are displayed in Table 2.3; it can be seen how some objects are able to keep their mass, while others drastically shrink. The main mass loss occurs at the resolution step of 10x. Interestingly Bofur was the only halo who was able to increase its mass at UHR.

### 2.4.2 Group classification and lifetime

The first step is the classification of the objects, which is done by using the methods described prior in the subsection 2.3 and a mass-to-light ratio of  $M_{\odot}/L_{\odot} = 1$ . In this case we define a halo to be a galaxy if it contains at least  $2 \times 10^{10} h^{-1} M_{\odot}$  of stellar mass and harbors a black hole. In Figure 2.13 the classification is displayed for Bofur 0 at  $z = 0.118$ , and it can be seen that Bofur 0 had in one perspective up to seven member galaxies, which would make him an extremely uncommon HCG. This large amount of member galaxies results from the fact that galaxies in this case are defined by their mass and not by their ability to be observational distinguishable. Therefore, from an observational point of view, likely a lower amount of galaxies would be observed.

From our five objects, three halos which could be classified as compact groups were found; these objects are Thorin, Bofur and Dwalin. In Nori and Gloin no halo satisfies the classification criteria because the Nori splitted up into several individual galaxies and Gloin lost to much mass and is in the end not massive enough. These objects will be separately

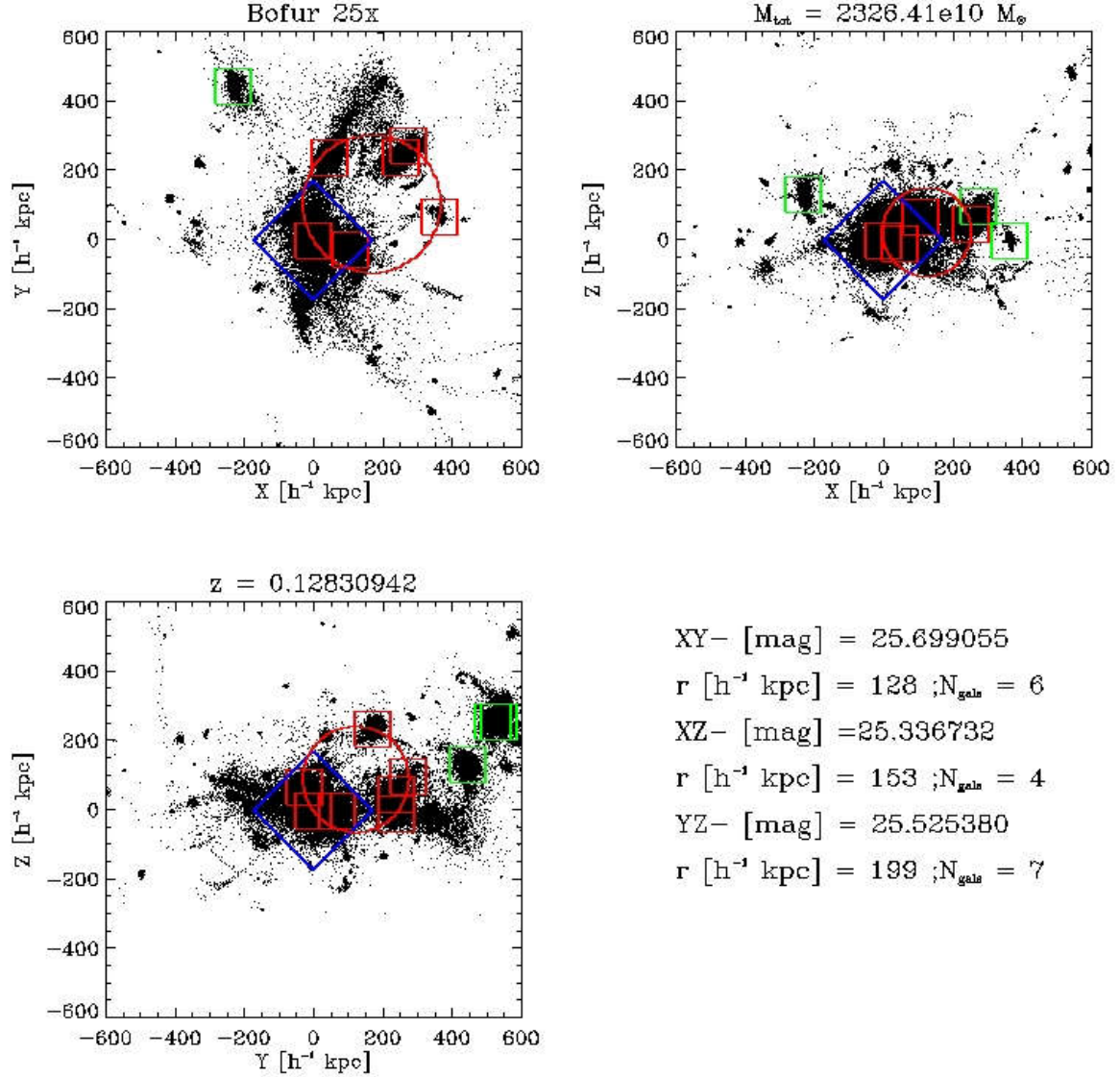


Figure 2.13: Compact group classification for Bofur 0 at  $z = 0.118$ . The red rectangles are member galaxies and the red circle is the smallest enclosing circle, which covers the area over which the mean surface brightness is calculated. The green rectangles show galaxies which are not included into the group. In the lower right panel the mean surface brightness for each projection, the radius of the smallest enclosing circle and the number of included galaxies is given.



Halo name	$m_{tot}$	$m_{star}$	$m_{gas}$	$N_{satellites}$	Group?
Thorin 0	4022.22	101.92	286.16	17	yes
Thorin 1	2808.62	70.04	131.21	13	no
Bofur 0	2626.72	67.76	195.17	8	yes
Bofur 1	1691.27	46.27	135.98	6	no
Bofur 2	1464.07	40.52	79.84	3	yes
Gloin 0	1274.99	28.27	76.38	6	no
Dwalin 0	1236.07	41.86	95.94	5	yes

Table 2.4: Total mass of all halos [ $10^{10} h^{-1} M_{\odot}$ ] at  $z = 0$  with  $m > 1 \times 10^{13} h^{-1} M_{\odot}$ . In addition their gas and stellar masses within  $r_{vir}$  and their number of satellites with  $m_{star} > 1 \times 10^{10} h^{-1} M_{\odot}$ , which are also within  $r_{vir}$ , are stated for their highest resolutions.

discussed in section (2.4.7).

A first guess about the question if an object is containing a group or not can already be taken by comparing the locations of the objects (Figure 2.4). The group objects prefer to sit in dense filaments or in a crossing of multiple filaments, while Nori is not part of any larger structure and Gloin is sitting at the tail of a filament.

In the object Thorin we found two halos with masses larger than  $1 \times 10^{13} h^{-1} M_{\odot}$ , but only one could be defined as a compact group. Dwalin contains only one halo inside the mass range which is a compact group. In Bofur, however, three halos with masses of  $m > 1 \times 10^{13} h^{-1} M_{\odot}$  were found, and two can be classified as compact groups, while the third is only rarely satisfying the criteria in case of merger events in some projections, and is not able to keep the status for a longer period. For all halos with  $m > 1 \times 10^{13} h^{-1} M_{\odot}$  their composition at  $z = 0$  is shown Table 2.4. In the following the main halo is labeled with 0, while the smaller halos are labeled with 1 and 2.

One of the major questions regarding compact groups is, if they are purely projection effects or not. In Figure 2.14 the time at which the objects would be classified as a compact group is shown in different projections.

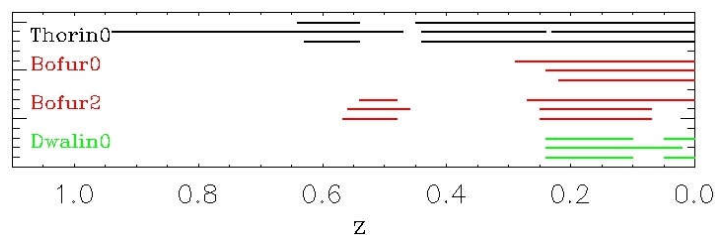


Figure 2.14: Temporal progression of the compact group classification for the halos of Thorin, Bofur and Dwalin. A solid line indicates that the object is classified as a compact group in a the corresponding perspective. From top to bottom for each object: xy-,xz-,yz-projection.

As it can be seen, do compact galaxy groups always have a preferred axis at which

the galaxies align and at which most of the mergers and interactions occur. Even though compact groups are prolate objects, it can be seen that in most of the times a compact group is classified as a compact group in all projections. This can especially be seen for Bofur 0, Bofur 2 and Dwalin 0, where there are only small times at which certain projections fail to satisfy the compact group conditions. For Dwalin however this result is quite defective due to very low temporal resolution in this simulation. This is also the reason why in the following discussion not all procedures were done for Dwalin.

In opposite to Bofur 0, Bofur 2 and Dwalin 0, Thorin 0 is able to evolve into a group much earlier, even though that at the beginning this is only visible in one projection. Here we can see the impact of the prolate shape of the group. The major difference between Thorin 0 and the other objects is their mass: Thorin 0 is roughly  $2 \times$  heavier than the other objects and it is able to accrete the mass much earlier.

Another difference between the objects is the mass at which they are classified as a compact group the first time. This mass is strongly varying. For the most massive object (Thorin 0), its first classification states a total mass of  $2.5 \times 10^{13} h^{-1} M_{\odot}$ , while for the halos in Bofur it is only  $0.8 - 1.8 \times 10^{13} h^{-1} M_{\odot}$ . This is similar to Dwalin 0 with  $0.9 \times 10^{13} h^{-1} M_{\odot}$ . The mass, when finally reaching the compact group status in all projections, is  $1.3 \times 10^{13} h^{-1} M_{\odot}$  for Dwalin 0 and  $1.2 \times 10^{13} h^{-1} M_{\odot}$  for Bofur 2.

### 2.4.3 Decoupling of gas and intragroup light

As observed and explained by Hickson (1997), the decoupling of the gas from the stellar component in the compact groups can be observed as well. This decoupling begins when the group members start to interact with each other. Even before the group can be classified as compact, decoupled gas can be seen due to prior mergers. But this gets more dominant if the halo becomes compact<sup>1</sup>.

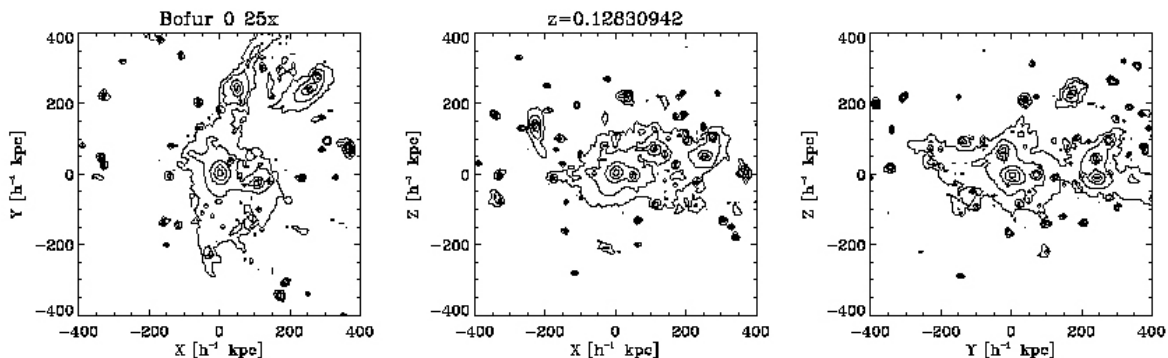


Figure 2.15: Contour diagram of Bofur 0 intragroup light at  $z \approx 0.13$ , where it is classified as a compact group in all projections.

<sup>1</sup>The decoupled gas component could have already be seen prior in Figure 2.2 for Bofur 0.

As observed by Da Rocha et al. (2008), compact groups are connected by diffuse intra-group light (IGL) which contains between 15 – 26 % of the total light in the cases of HCG 15, HCG 35 and HCG 51. This intragroup light is displayed in Figure 2.15 as contours for Bofur 0. This cohere region is evolving during the formation process of the compact group and can take up to  $1Gyr$  to cover all member galaxies. This evolution is, of course, much shorter if the group gets compact in all three projections at a similar time, but not necessarily all member galaxies are always comprised by the IGL in all projections.

A way to separate the IGL component from the galaxies is by their velocity distributions, which is done for the most massive compact groups Thorin 0 and Bofur 0. As demonstrated by (Dolag et al., 2010) and (Remus et al., 2017) for the brightest cluster galaxy and the intracluster light these components split up into two dynamical components. For this examination at first all substructures identified by SUBFIND and its corresponding particles are excluded and the global velocity is subtracted. Afterwards a double Gaussian is fitted to the histogram of the velocity distribution with an equal bin size of  $\Delta v = 10km/s$ . In Figure 2.16 the velocity distribution for Thorin 0 at  $z = 0$  is displayed.

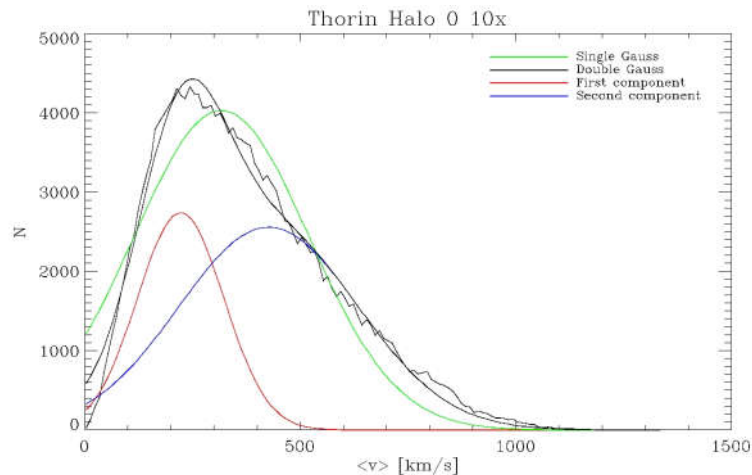


Figure 2.16: Velocity histogram for the main galaxy and the IGL of Thorin 0 at  $z = 0$ .

Here it can be seen how the distribution is only very poorly described by a single Gaussian, which requires a second component. With two distinctive components the behavior can be represented very well. In all cases the slower Gaussian represents the main galaxy of the group and the faster Gaussian the IGL component in the group. Interestingly, here the IGL component is of larger size than the main galaxy. By comparing the integral of the IGL component with the total integral over the distribution without removing the substructures the IGL fraction is determined. This determination is done for all time steps since  $z = 1.2$  and is shown in Figure 2.17 for Thorin 0.

It can be observed how the Thorin 0 is accreting mass over time, initially only minimal till  $z \approx 0.7$ , where a major accretion takes place with also the total IGL component in-

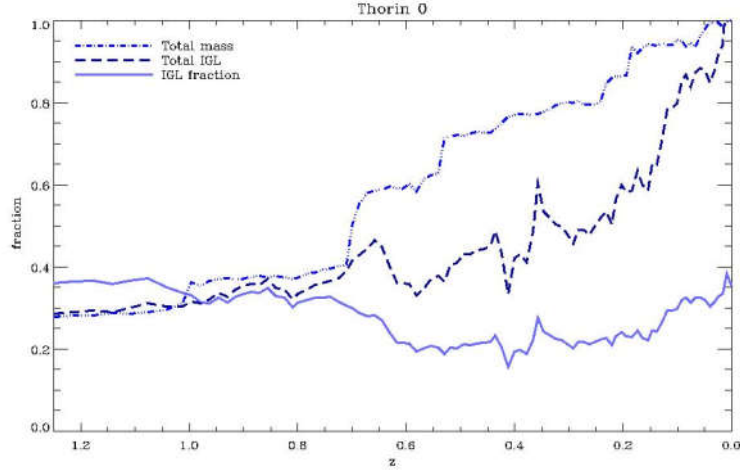


Figure 2.17: Evolution of the total mass, IGL mass and IGL fraction over time for Thorin 0.

creases due to the disruption of the merger, while the IGL fraction goes down because most of the infalling mass is still bound to the galaxies and other substructures. Afterwards at  $z \approx 0.5$  a second significant impact takes place and is again increasing the IGL component and is causing the two following peaks in the IGL mass. After these events the halo is continuing to steadily increasing mass either in total as well as in the IGL component. As already seen in Figure 2.14 Thorin 0 evolves to a compact group at  $z \approx 0.9$  the first time and is only interrupted at  $z \approx 0.45$ , and these times are in agreement with the major accretion events. During its time as a compact group the fraction of IGL of Thorin 0 is 15 – 40 % (and 10 – 30 % for Bofur 0) which is in good agreement of the observational results mentioned earlier.

#### 2.4.4 Kinematic evolution

In order to get a classification of the galaxies the  $b$ -value (Teklu et al., 2015), including the correction for redshift (Obreschkow et al., 2015), is calculated for all time steps.

$$b = \log_{10} \left( \frac{j_{star}}{kpc \ km \ s^{-1}} \right) - \frac{2}{3} \log_{10} \left( \frac{M_{star}}{M_{\odot}} \right) + \frac{1}{2} \log_{10} (1 + z) \quad (2.10)$$

A galaxy with a value of  $b \approx -4$  is classified as a disc and  $b \approx -5$  as a pure spheroidal (Romanowsky and Fall, 2012). For the region of measurement, 10 %  $R_{vir}$  was used. For the compact groups, the main galaxies in the two most dominant halos, Thorin 0 and Bofur 0, are described. In Figure 2.18 the evolution of the  $b$ -value of the halos of Thorin 0 and Bofur 0 is displayed.

The trend of Thorin 0 is highly fluctuating, which is due to the high frequency of merger events for this halo, and which can also be suggested from Figure 2.19. Nevertheless it can

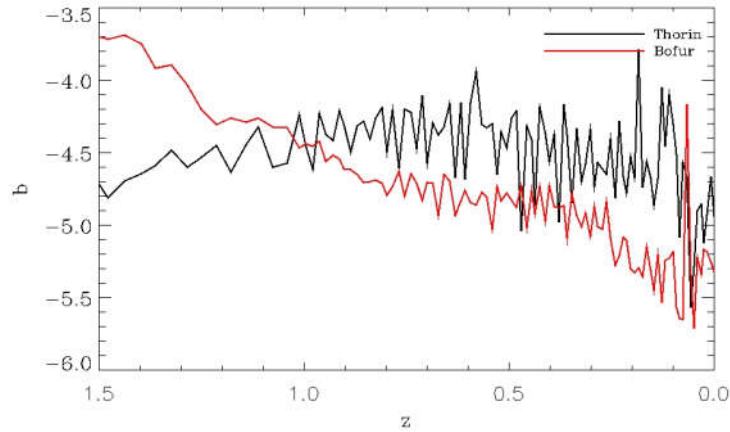


Figure 2.18:  $b$ -value of the main galaxies in the objects Thorin 0 and Bofur 0 over time.

be seen that Thorin 0 initially increases its  $b$ -value and decreases it at later times. In the case of Bofur 0, a steady decrease and a more peacefully evolution is visible. The major dip at  $z \approx 1.25$  is due to a major merger, which distorts the former ordered motion of the main galaxy and is therefore causing the dip in  $b$ . At  $z < 0.3$ , mergers at a high frequency occur and are responsible for the high fluctuations regarding the  $b$ -value in that period.

The evolution of the  $b$ -values regarding the main galaxy of Bofur 0 and its nearest neighboring galaxies at all times tends to lower values. In the upper left panel of Figure 2.19 it is displayed how neighbor galaxies approach the main galaxy with time and how their  $b$ -value decrease. Another trend which can be observed in the upper left panel of Figure 2.19 is that the lowest  $b$ -values are achieved close to the center of the group at times close to  $z = 0$ .

In the upper right panel of Figure 2.19, the evolution of Bofur 0 in the stellar mass vs. stellar angular momentum plane is displayed. The separated group of symbols on the right corresponds to the evolution of the main galaxy. It illustrates very clearly how it gained mass over time and how the stellar angular momentum decreases with increasing mass, but tends to increase again in the latest times. The combination of the two axis results in the  $b$ -value and are displayed in Figure 2.18. For the neighboring galaxies, which are the left group of symbols, also an increase in mass but only a slight trend to lower  $b$ -values can be seen for most galaxies.

For Thorin 0 this evolution is more chaotic, see the lower left panel of Figure 2.19. Here the individual tracks of the galaxies can't be observed that clearly as for Bofur 0. But the general trend to lower  $b$ -values is visible as well. In the lower right panel of Figure 2.19 the separation of the main galaxy from the other galaxies occurs as well. Here, nevertheless despite the mass growth, no trend regarding the  $b$ -value is visible. Also for the nearest galaxies no general mass growth or change in  $b$ -value can be determined, although more  $b$ -values with a lower value are reached at later times.

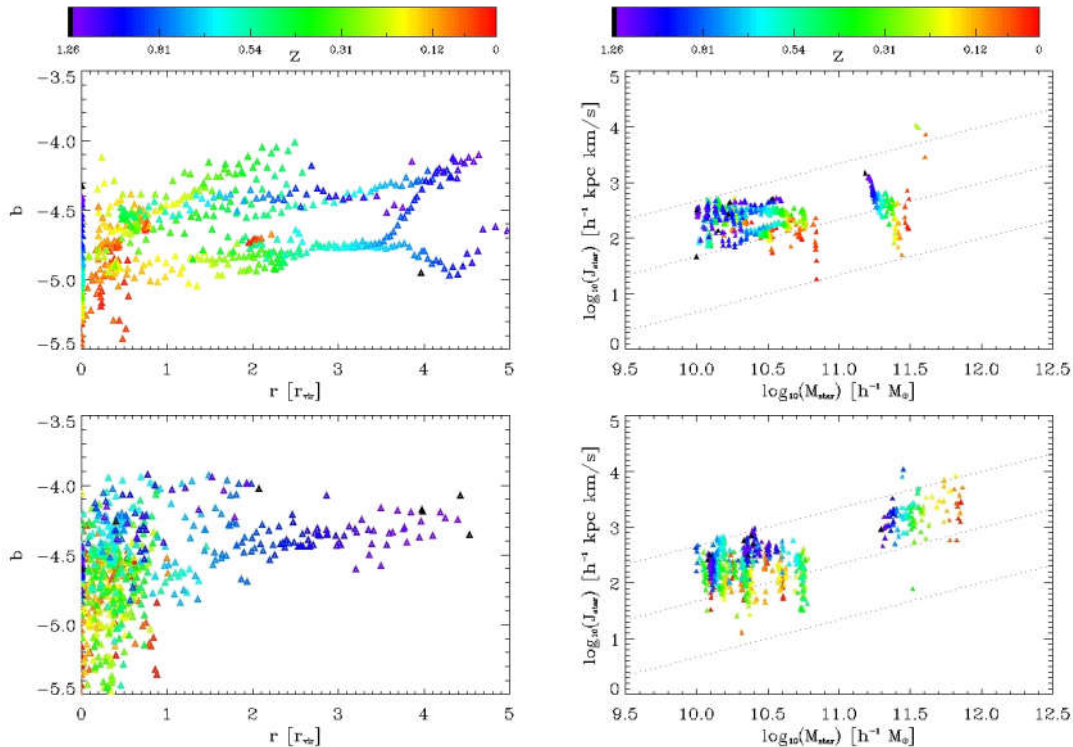


Figure 2.19: Upper row Bofur 0 and lower row Thorin 0: a)  $b$ -values of the closest neighboring galaxies over time. b) Stellar mass inside the half-mass radius vs. the corresponding specific angular momentum. The dotted lines indicate, from top to bottom,  $b$ -values of  $-4$ ,  $-5$  and  $-6$ .

### 2.4.5 Mass-size relation

For further insight on the main galaxies, the evolution of these galaxies in the mass-size plane is studied, as it is well known that there is a correlation between the sizes and masses of galaxies regarding their type.

The function of the mass-size relation is motivated by Shen et al. (2003), and is a combination of two power-law functions:

$$R_e = \gamma \left( \frac{M_*}{M_\odot} \right)^\alpha \left( 1 + \frac{M_*}{M_0} \right)^{\beta-\alpha}. \quad (2.11)$$

Here  $R_e$  is the effective half-light radius, where we will use the half-mass radius of the stellar mass  $M_*$  within 10 %  $r_{vir}$  while excluding any substructure.  $M_0$  is the breaking point between the two different power laws, and is an artificial transition mass. For  $\gamma$ ,  $\alpha$ ,  $\beta$  and  $M_0$  we use the values from Lange et al. (2016) and their morphological cut in the r-band, which are displayed in Table 2.5.

parameter	early type	late type
$\alpha$	0.11	0.16
$\beta$	0.78	1.0
$\gamma$	0.12	0.1
$M_0$	$2.25 \times 10^{10} M_\odot$	$33.62 \times 10^{10} M_\odot$

Table 2.5: Mass-size relation parameters.

The resulting masses and sizes for the central galaxies are displayed in Figure 2.20. It can be seen that, in general all of our galaxies lie within or near the range of the observational mass-size relation.

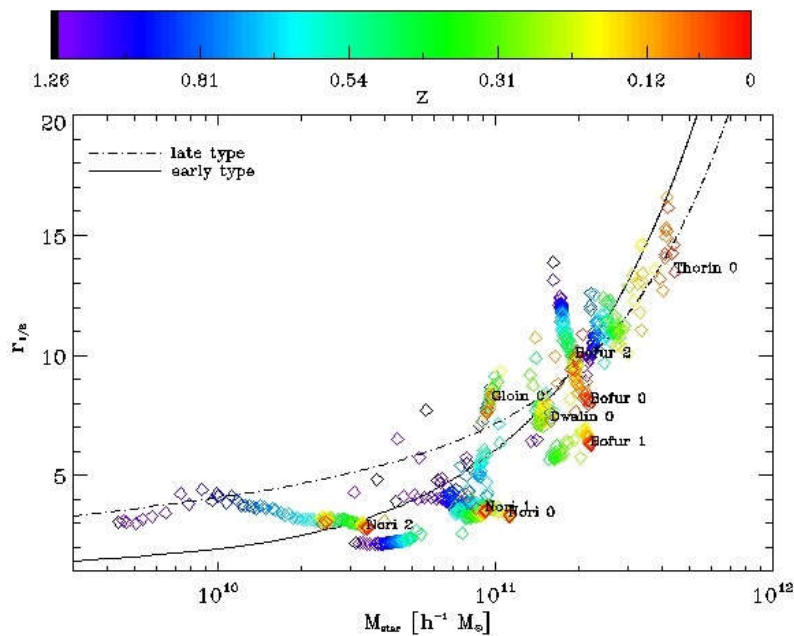


Figure 2.20: Mass-size relation and evolution for all main galaxies.

Although the final galaxy type of the halos can't be determined only by this approach, a few trends are visible. At first it can be seen that central galaxies of groups prefer to lie near or above the transition of the different mass-size relations. This means that the major galaxy in compact groups is preferred to be a large galaxy. Interestingly, do all central galaxies of Bofur lie very close to this transition point, although the central galaxies of Bofur 0 and Bofur 2 have larger sizes than the main galaxy of the non group halo Bofur 1 at similar mass. While Bofur 1 and Bofur 2 have a quite chaotic evolution, Bofur 0 has a very interesting track in the mass-size plane. It is becoming more compact without increasing significantly in mass, which is in contrast to all other halos. This behavior is related to the fact that, even though it is a compact group it has no major merger since



$z = 1.2$ . It is only accreting  $\approx 35\%$  of its mass during that time, and is therefore able to contract itself. Only at times close to  $z = 0$  some major merger events are starting and this would suggest an increase in mass and size in the near future. Due to the proximity of the two different mass-size relations in this area, no classification attempt can be done for the central galaxies of Bofur and Dwalin. As the most massive central galaxy, Thorin 0 already started above the transition mass and is then evolving in between the two mass-size relations while increasing mass over time, but in the end tending towards the mass-size relation of an early-type galaxy. For the objects in Nori, a more classical behavior can be seen. They are in general much more compact, and while accreting mass they are moving more or less steadily from a late-type to a more early-type galaxy; only interrupted by major merger events which leave gaps in the tracks, as it is visible for Nori 1 for example. Gloin 0 and Dwalin 0, on the other hand, don't show any real tracks, but are more or less stable, without larger mass-accretion or size variations.

#### 2.4.6 Final stage of evolution

As by looking at the kinematic properties and the mass-size evolution of the galaxies in the compact groups, the first guess leads to the idea that the compact groups evolve into a giant elliptical galaxy in the end.

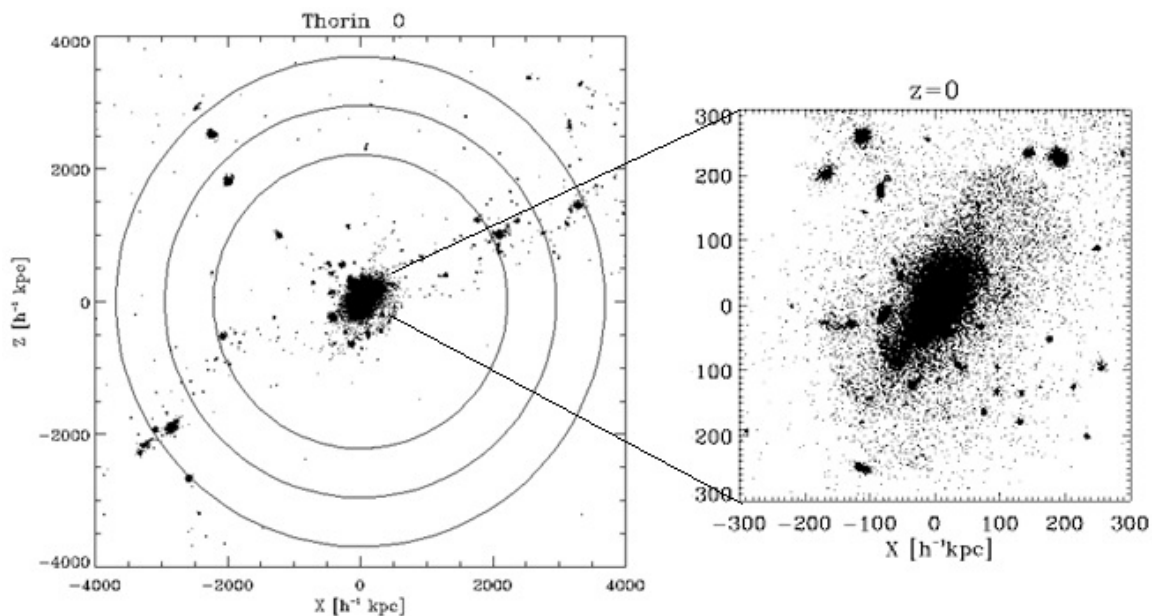


Figure 2.21: a) Stellar environment of Thorin 0 at  $z = 0$ . The circles indicate distances of 3, 4 and 5  $r_{vir}$  from the center. b) Central view on Thorin 0.

There are a few indicators for this conclusion. One is the general trend to lower  $b$ -values for all main galaxies in compact groups. Also, the central galaxy of the most dominant



compact group, Thorin 0, tends towards the mass-size distribution of an early-type galaxy. In addition, the study of the halo indicates a spheroidal object, as it is illustrated in the right panel of Figure 2.21 for the halo Thorin 0 at  $z = 0$ . The isolation of Thorin 0 can be seen in the left panel of Figure 2.21, where there are almost no other large objects except a few single galaxies until a radius of  $5 r_{vir}$ .

This is supporting the initial idea of Hickson (1997), that giant elliptical field galaxies, also called fossil groups are the remnant of compact groups. Nevertheless, it is only one object which shows clear indications on the final stage of compact galaxy groups, therefore no statistics can be applied and no final conclusion can be drawn and especially no conclusions can be drawn how the evolution of compact groups at higher redshift evolves.

### 2.4.7 Non-group objects

The object Nori, seemed promising at the beginning, unfortunately evolved itself to an object with three individual, non-interacting major halos, with masses of Nori 0 =  $3.29 \times 10^{12} h^{-1} M_{\odot}$ , Nori 1 =  $2.27 \times 10^{12} h^{-1} M_{\odot}$  and Nori 2 =  $2.37 \times 10^{12} h^{-1} M_{\odot}$  at  $z = 0$ , but broke up into three individual galaxy-mass halos at higher resolution.

Obviously this object is not a candidate for a compact group, as it is visible in Figure 2.22 for Nori 0 at  $z = 0$ .

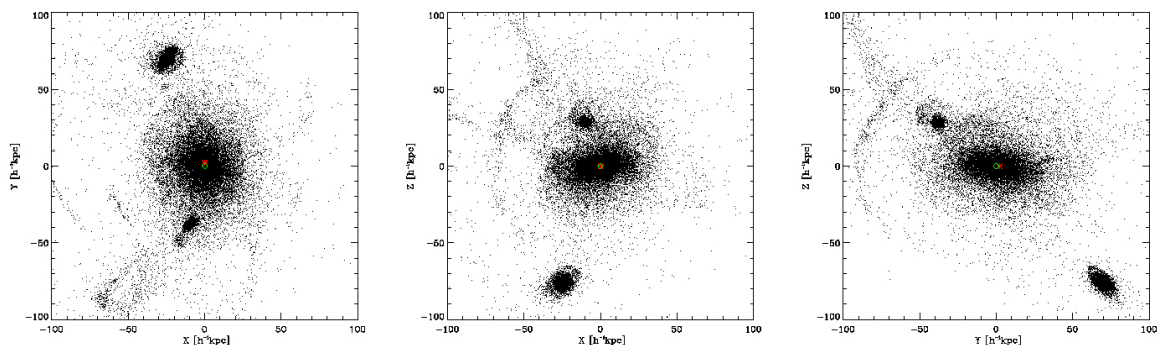


Figure 2.22: Stellar component of the largest halo with  $3.39 \times 10^{12} h^{-1} M_{\odot}$  in Nori at  $z = 0$  in three projections. The black hole (red star) and the gravitational center (green diamond) of the galaxy are displayed as well.

In all three major halos of Nori, the main galaxy tends to evolve to lower  $b$ -values over time, which is displayed in Figure 2.23. This trend is due to the loss of angular momentum due to cosmic expansion (Obreschkow et al., 2015), which results in a lower  $b$ -value with decreasing redshift.

The peaks, either positive or negative, in the  $b$ -value are due to significant merger events. For three peaks this is shown in the lower panel of Figure 2.23, while here the first passage of the merger is displayed. It can be observed that, in case of Nori 1, the  $b$ -value has a significant drop afterwards due to the merger, while Nori 0 and Nori 2 don't show a general increase or decrease after the peak. The satellite corresponding to the merger event

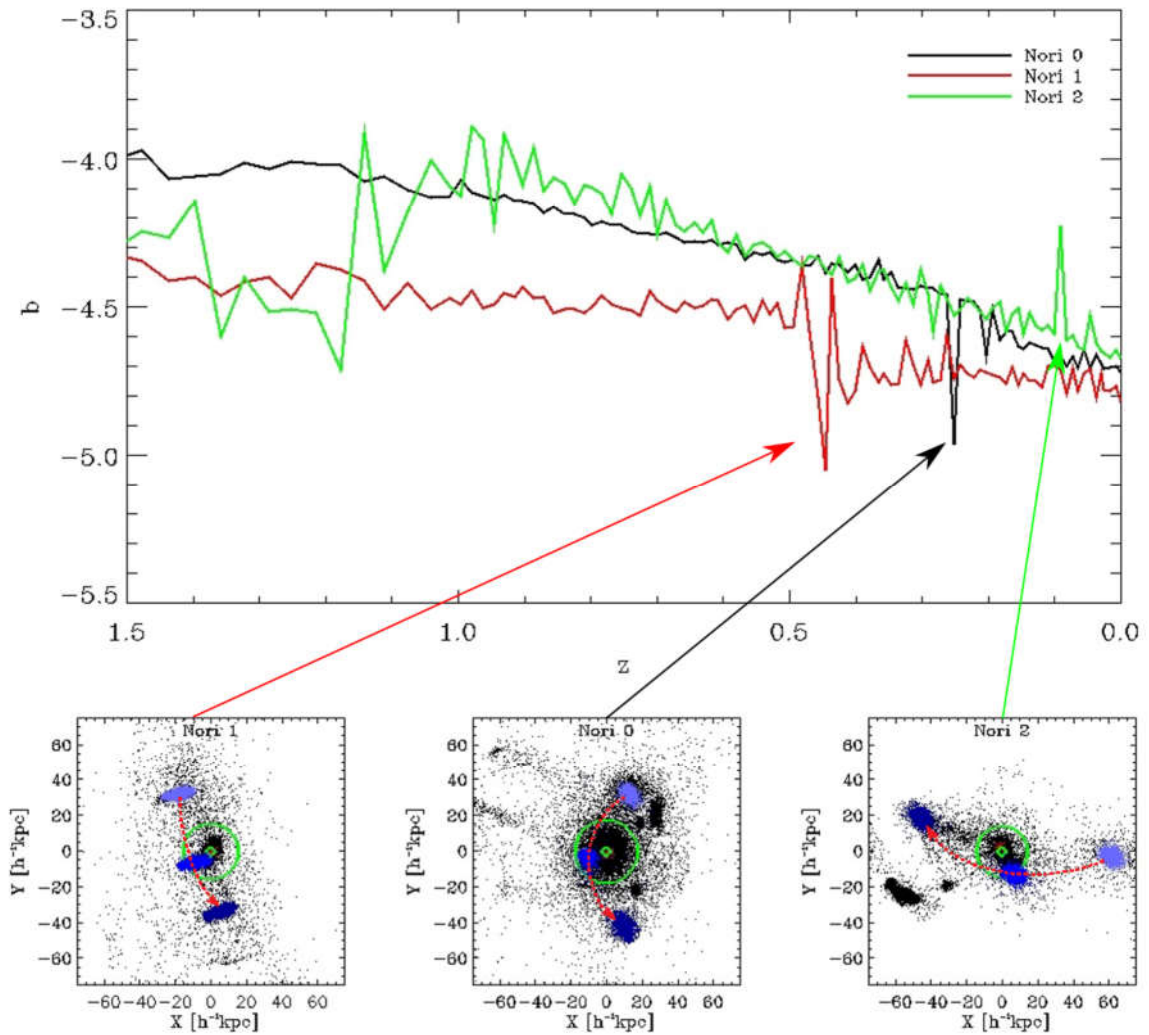


Figure 2.23: In the upper panel the  $b$ -values for all major halos in Nori from  $z = 1.5$  till  $z = 0$  are displayed. In the lower panel, the merger causing the sharp peaks in the  $b$ -value is shown at three time steps: before, during and after the passage. The path of the merger is displayed by the green dashed line, while the solid green circle represents  $10\% R_{vir}$  of the object.

in Nori 1 is a  $\sim 1:2$  major merger in stellar mass, and is therefore significantly disturbing the host galaxy, which leads to the decline in  $b$  in this case. Interestingly, the general increase for Nori 2 at  $z \sim 1.15$  is due to a merger (mass ratio  $\sim 1:4$ ) as well, but here a positive step in  $b$  occurs. Nori 2 has in addition a  $\sim 1:2$  major merger at  $z \sim 0.1$ , but the peak corresponds to the first flyby and the merger is due to its high velocity only reaching its first turning point at  $z = 0$  and is not finished yet. The merger for Nori 0 is, in contrast to the other mergers, only a minor merger with a mass-ratio of  $\sim 1:10$  in stellar mass, and therefore not that massive enough to cause a similar significant decline as for Nori 1.

From a first analysis the reason for the merger leading to a decline or increase of the  $b$ -value could not be determined with sufficient accuracy. Nevertheless it has to be connected with the orbit and the mass-ratio of the merger. A full orbit determination of the merger is necessary in order to understand the influence of a merging event to the  $b$ -value. All these findings make Nori an interesting object, not for the study of compact groups, but for further studies about the evolution of Milky-Way mass galaxies and their kinematics.

The only halo in G101 with a total mass larger than  $1 \times 10^{13} h^{-1} M_{\odot}$  has a very low mass stellar component, which could have already be seen in Table 2.4. During the mass accretion of the halo at several time steps a minimized group is visible. However it is simply not massive enough and therefore fails the brightness criteria. At  $z = 0$ , a single galaxy with a  $b$ -value of  $-5.1$ , which would suggest the type of the galaxy as an early-type galaxy, is present. This galaxy is accompanied by a larger satellite, which can be seen in the lowest three panels of Figure A.1 in the appendix.

## 2.5 Conclusion and possible future work

Compact galaxy groups are ideal surroundings to study the evolution of galaxies in dense regions and their corresponding physics due to galaxy-galaxy interactions. In order to find compact groups, only halos with  $1 \times 10^{13} h^{-1} M_{\odot} < M < 1 \times 10^{14} h^{-1} M_{\odot}$  and with at least 4 sub-halos were chosen. But due to the inaccuracies with the AGN model these simulations only stayed at a lower resolution as initially planned.

Nevertheless, a few insights could already be made. At first it can be said with high confidence, that compact groups are no projection effects. Even though there might be some observed groups which are a projection, the simulations show that compact groups are real and physically dense objects and that they are compact in almost all projection.

Also the decoupling of the gas and the build-up of the intra group light could be seen. In addition, the IGL component can be separated from the component bound to the galaxies and it can be observed how the IGL builds up while the group is getting more compact, and with the corresponding increase in frequency of interactions. Interestingly not necessarily all galaxy members are connected by the IGL in all cases all the time, not even in constellations where it satisfies the compactness criteria in all projections.

In addition there are clear hints by the study of Thorin 0 and the general evolution of the main galaxies in compact groups that the remnant of a compact group might be a

giant elliptical galaxy<sup>2</sup>.

For the future there are many things which could be studied and where the procedure illustrated in this thesis would be promising. For example, an examination of the compactness criteria not only in three projections, but for every possible angle about how precise the classification scheme is would complete the picture. It would also be interesting to see, if the remnants of the simulations show, for example, the same velocity dispersions and luminosities found in present day giant ellipticals to get a better picture about the remnant of compact groups. Another interesting aspect to study would be the appearance of shocks and their influence on the gas distribution, and to see how this correlates with the decoupled gas.

As a side effect of the simulations, the halos in Nori were found, which are no compact groups but three Milky-Way mass halos. The object itself is very interesting due to three halos of Milky-Way mass evolve in close proximity together, but without any larger structure nearby. In these objects the effect of mergers onto the  $b$ -value could be seen very well, but a further and deeper study is necessary to fully understand the corresponding kinematics.

In general it can be seen that compact groups are highly interacting regions dominated by mergers, which play a significant role in their general evolution and in the evolution of their member galaxies.

---

<sup>2</sup>Albeit it is possible that compact groups at high redshifts might have become part of larger galaxy clusters eventually, but compact groups at high redshift were not included in this study.

### 3. Idealized galaxy mergers

In the standard cosmological models, galaxy mergers are a basic and significant process in galaxy evolution. Mergers are important for the hierarchical growth of galaxies, their profile-shapes, as well as their kinematic evolution.

As shown by Rodriguez-Gomez et al. (2016), the major contributor to stellar mass growth are major mergers ( $\mu > 1/4$ ), while minor ( $1/10 < \mu < 1/4$ ) and very minor mergers ( $\mu < 1/10$ ) contribute roughly the same amount. For spheroidal galaxy mergers, Hilz et al. (2012) found (in order to understand the inside-out growth of giant elliptical galaxies) that minor mergers lead to an increased size growth and a more rapid profile shape change compared to major mergers. Through stripping, dry minor mergers also increase the size of a compact spheroid, which results in an almost unchanged inner host structure as shown by Hilz et al. (2013). This is in agreement with Lagos et al. (2018), who found that dry mergers increase the stellar mass density in the outskirts of the galaxy, while wet mergers tend to build the bulge of the host galaxy.

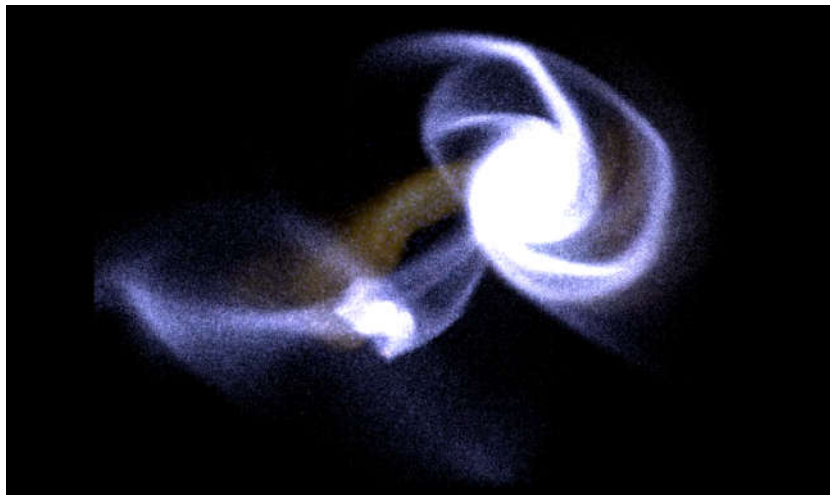


Figure 3.1: Visualization of a 1:5 merger after the first passage using SPLITCH.

It is well known (e.g. Cooper et al. (2015), Rodriguez-Gomez et al. (2016) and Zolotov et al. (2009)) that the *in-situ* stellar halo dominates over the accreted stellar halo in the inner region of the remnant, while the stellar component in the outer parts is the result

of merging and accretion processes. These outer regions can extend up to a few hundreds of  $kpc$  (Zolotov et al., 2009). And these accreted stellar components, manifesting as tidal features, are observed in up to 26% of galaxies (Atkinson et al., 2013). These tidal features are also more likely to occur in massive galaxies with  $M > 10^{10.5} M_{\odot}$  (Atkinson et al., 2013) than in low mass galaxies. This is in agreement with Martínez-Delgado et al. (2010), who also finds that many spiral galaxies in the Local Universe inhabit significant numbers of giant stellar structure which are remnants of an earlier accretion process.

The disruption of the merging galaxy is a reasonable mechanism for the production of intrahalo light (IHL) on all scales. For galaxies, the IHL is dominated by the disruption of satellites with a stellar mass  $\sim 10^{8.5} M_{\odot}$ , and its properties are defined by the corresponding merger history (Purcell et al., 2007). This diffuse IHL has been observed recently in several galaxies (Merritt et al., 2016) and a giant stellar disc, extending up to  $70kpc$ , has been discovered recently by Zhang et al. (2018).

Idealized merger simulations ignore the cosmological background and therefore important features like gas accretion and environmental effect. But they are, in contrast to full cosmological or zoom-in simulation, much more computational time saving and are offering a huge range of possibilities regarding the study of galaxy mergers. It offers the opportunity to collide any type of galaxy, with any mass-ratio at any orbital configuration at any resolution necessary for the specific aim. These kind of simulations have been used since a long time and contributed to the further understanding of galaxy evolution.

## 3.1 Method

The simulations are also carried out using the Tree-SPH code GADGET-3 as described in subsection 2.2.4. Here also, supernova feedback is used and a Supermassive Black Hole (SMBH) is included in the center of the colliding galaxies. Due to the higher resolution, and the corresponding much smaller softening length, the SMBHs are staying in the centers of the galaxies and merge on reasonable timescales.

### 3.1.1 Galaxy set-up

The initial conditions for the study are created using the method that has been described in Springel (2005). Further documentation of the method can be found in Springel et al. (2005) and Cox et al. (2006). The setup for the isolated disk galaxies consists out of a dark matter halo, a spherical bulge as well as an exponential stellar and gas disk. The dark matter halo follows a spherical Hernquist-profile (Hernquist, 1990, 1993). This profile yields:

$$\rho_{\text{dm}}(r) = \frac{M_{\text{dm}}}{2\pi} \frac{a}{r(r+a)^3}. \quad (3.1)$$

$M_{\text{dm}}$  is the total dark matter mass of the halo, it describes the relation between the halo concentration parameter  $CC$  and the scale length  $r_s$  of the well known NFW-profile

(Navarro et al., 1997). The stronger decline of the Hernquist-profile in its outer parts gives the advantage of convergence. While the NFW-profile must be numerically integrated and truncated to obtain the mass distribution, the Hernquist-profile can be integrated analytically. Therefore, we can evolve the mathematical expressions for the mass distribution and velocity distribution directly from an analytic model. In this galactic model the bulge also follows a Hernquist-profile, giving the same advantages in terms of implementation. The stellar disk and the gas disk are following a surface density profile given via:

$$\Sigma_{\star} = \frac{M_{\star}}{2\pi l_d} \exp\left(-\frac{r_{\text{polar}}}{l_d}\right), \quad (3.2)$$

for the stellar disk, with  $M_{\star}$  as the stellar mass in the disk and  $l_d$  as a scaling parameter. The same is valid for the gas component of the disk.

$$\Sigma_{\text{gas}} = \frac{M_{\text{gas}}}{2\pi l_d} \exp\left(-\frac{r_{\text{polar}}}{l_d}\right), \quad (3.3)$$

The parameter  $r_{\text{polar}}$  is the radius component in cylinder-coordinates with the gas mass  $M_{\text{gas}}$  and the same scaling factor  $l_d$  as given in the stellar disk.

For this study, five similar disk galaxies are created by using the method described above. All dark matter halos have a concentration parameter of  $CC = 12$ . The stellar bulges of these systems are modeled with a mass fraction of  $m_b = 0.01367$  regarding the total mass. The exponential disk contains a gas fraction of  $m_{\text{gas}} = 0.2$  and a total mass fraction of  $m_d = 0.041$ . The galaxies also contain a black hole in their center with a mass of  $M_{\text{BH}} = 1.186 \times 10^5 M_{\odot}$ . This results in a darkmatter- to baryonic mass fraction of  $M_{\text{dm}}/M_{\text{bar}} = 10$  per particle. Our main galaxy, (further on called as host-galaxy) is a Milky Way-like galaxy with a total mass of  $1.89 \times 10^{12} M_{\odot}$ , corresponding to a virial velocity of  $v_{200} = 160 \text{ km/s}$ . The galaxy consists of 10.8 Million particles in total, which split up into: 6.8 Million halo-, 1 Million bulge-, 2.4 Million disc-, and 0.6 Million gas-particles. This results in a mass of  $\approx 1.88 \times 10^4 M_{\odot}$  per baryonic particle, which gives us sufficient mass resolution to study the merger process in great detail.

All other three galaxies are downscaled copies of our host-galaxy. In order to cover a broad range of different masses the other galaxies were created, by a factor of 1/5, 1/10, 1/50, 1/100, lighter than the host-galaxy. The resulting main parameters of the individual galaxies can be seen in Table 3.1.1.

### 3.1.2 Stability tests

Prior to any simulations, the stability of the galaxy set-up and the compiled code has to be tested. This was done by letting the initial host galaxy itself run and evolve for the same time as the later simulations without any further interactions. Here, the effects of the numerics and of the model itself were studied. This test proved that the model

Mass ratio	$v_{200}$	Mass [ $M_{\odot}$ ]	number of baryonic particles
1	$160 \text{ km/s}$	$188.7 \times 10^{10}$	$400 \times 10^4$
1:5	$94 \text{ km/s}$	$37.7 \times 10^{10}$	$80 \times 10^4$
1:10	$74 \text{ km/s}$	$18.9 \times 10^{10}$	$40 \times 10^4$
1:50	$43 \text{ km/s}$	$3.8 \times 10^{10}$	$8 \times 10^4$
1:100	$34 \text{ km/s}$	$1.9 \times 10^{10}$	$4 \times 10^4$

Table 3.1: Main parameters of the created galaxies

remained almost constant over this time, with only slight changes in the disc scale height and also only minor changes in the Hernquist profile of the bulge. This can be seen in Figure 3.2 where the final profile is almost identical with the initial. This also proves that the softening length is reasonable. The model only evolved some kind of spiral structure due to numerics which nevertheless is no problem regarding the aim of our study but would be crucial if someone wanted to study the inner regions of the galaxy in more detail.

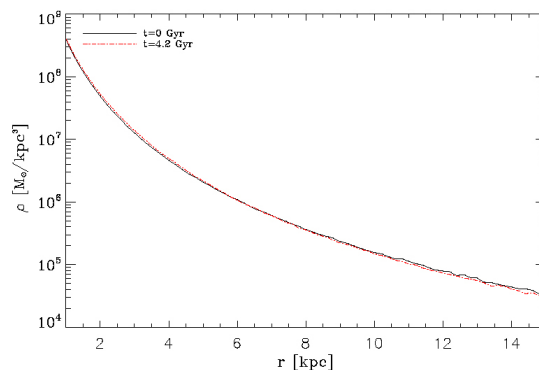


Figure 3.2: Comparison of the radial density profile of the Hernquist sphere at the beginning and at the end of the simulation.

### 3.1.3 Merger set-up

The simulations consist of eight different orbital parameters, each executed with four different mass ratios, and some special orbits where some parameters are combined. The resulting 35 simulations cover a broad range of different orbit parameters as well as different mass-ratios. For the angular orientation of the galaxies itself, the angles  $\omega$  and  $\iota$  as described by Toomre and Toomre (1972) are used. The impact parameter in our collisions is defined by the angle  $\alpha$ , which is an equivalent analog for the pericentric distance, and the angle  $\Omega$  for the inclination of the orbit corresponding to the main plain. These parameters are chosen because they provide freedom in modifying the parameters in every thinkable way without being restraint to any specific kind of orbit configuration. The corresponding pericentric distances to each value of  $\alpha$  are shown in Table 3.1.3.



For all simulations the initial distance between the galaxies has been set to  $d_{sep} = 80kpc$ , a distance roughly three times the radius of the host-galaxy (which is a reasonable distance either in a physical sense, because it anticipates almost no interaction, and also keeps the amount of computational time at a reasonable level). Their approaching velocity is equal to the virial velocity regarding the host galaxy, which yields to  $v_{vir} \approx 144.1km/s$ . The velocity vector is always parallel to the adjacent side of  $\alpha$  and always pointing in the direction of the other galaxy, which can be seen in Figure 3.3. Each simulation is run long enough that the galaxy has roughly  $3.5Gyr$  to relax itself after the collision.

The set of simulations can be separated in two families. In the first family, family 1, the orbits are in the plane of the host-galaxy disc, while the merging galaxy is tilted by an angle of  $\omega = 30^\circ$ , and  $\iota = 0^\circ$ . Their impact parameter is varying,  $\alpha \in \{10^\circ, 20^\circ, 30^\circ, 40^\circ\}$ , and a geometrical description of these orbits can be seen in Figure 3.3. For each value of  $\alpha$ , four simulations with different mass ratios (1:5,1:10,1:50,1:100) were executed.

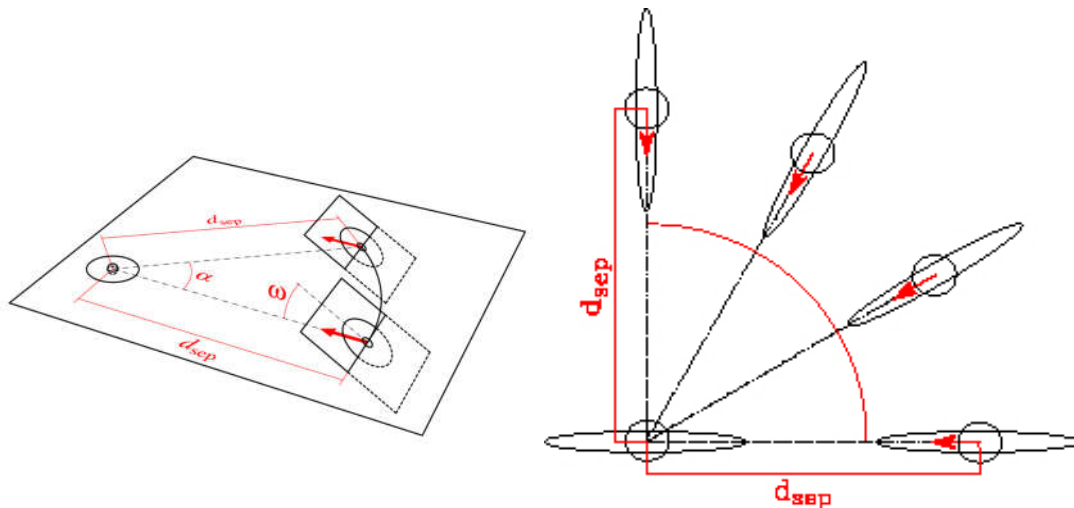


Figure 3.3: a) The geometrical set-up for all family 1 mergers. In this family the only varied variable is  $\alpha$  and  $\omega$  is keep constant at  $30^\circ$ . b) For family 2 the different orbits are a result in varying  $\Omega$  and keeping  $\alpha = 0^\circ$  constant.

For the second simulation family, family 2, the geometrical setup is shown in Figure 3.3. Here we fix  $\alpha$  to  $0^\circ$  and vary  $\Omega \in \{0^\circ, 30^\circ, 60^\circ, 90^\circ\}$  instead. In this family,  $\omega = 0^\circ$  and  $\iota = 0^\circ$ . Again, for every combination, the simulation has been performed with all four mass ratios. In addition to the two families a few 1:100 mergers as special cases were executed, whose orbit parameters can be taken from Figure 3.5.

impact parameter $\alpha$	$10^\circ$	$20^\circ$	$30^\circ$	$40^\circ$
pericentric distance [ $kpc$ ]	1.8	7.0	15.0	24.8

Table 3.2: Comparison between  $\alpha$  and the pericentric distance.

## 3.2 Results

### 3.2.1 Mass-deposition

In order to study the mass-deposition of the merging event we calculated the corresponding surface density distributions of the remnant. One of the global trends concerning the surface density deposition, which is displayed for all simulations in Figure 3.4, is that at a certain radius the merger galaxy starts to dominate the resulting mass-profile. This behavior is independent of the impact parameter  $\alpha$  or  $\Omega$ . This point is mainly depending on the mass-ratio of the merger, while a larger merger has a closer turning point and for a minor merger the turning point lies at larger radii. This insight is confirming common knowledge. Also the total mass which is deposited inside of the remnants disc-range is mainly depending on the mass-ratio. While a 1:100 merger is only able to deposit  $\sim 25\%$  of its initial baryonic mass inside the disc-range of the remnant, a 1:5 merger is able to deposit up to 80%. This is confirming earlier studies (e.g. Hilz et al. (2013)), which promote that minor mergers result in faster size growth, while major mergers result in higher mass growth.

It can also be seen globally that the very minor mergers only have a slight impact on the surface density distribution of the merger remnant, if compared to the initial galaxy. The gradient of the merger remnant follows the initial gradient for minor mergers for radii of up to  $\sim 30kpc$  ( $\sim 4 \times r_{1/2}$ ) while minor mergers already have a significant influence on the gradient at  $\sim 15kpc$  ( $\sim 2 \times r_{1/2}$ ). But for all mergers the enrichment of the outskirts is much more significant than in the center of the galaxy.

Starting with family 1, for the minor mergers (panel 5 and 6 of Figure 3.4) the surface density distribution is very similar for different  $\alpha$ . Mergers with both of these mass-ratios are able to reach the center of the remnant in a significant manner, and are therefore able to disturb the host-galaxy strongly. This can also be seen by comparing the Sersic-indices of the remnant, which is done in subsection 3.2.6.

A trend which can already be discovered at the 1:10 mergers, but which gets more dominant for the very minor mergers, is that the merger isn't able to contribute to the galaxy center anymore. Instead, they have a first peak at a radius of  $\sim 5$  to  $20kpc$  ( $\sim 1 - 3r_{1/2}$ ) depending on the mass ratio and impact parameters. The shape of the distribution nevertheless stays similar for the individual mass-ratios, while getting damped slightly and mainly shifted to the outer regions with increasing  $\alpha$ , leaving an almost vacant region in the center (panel 7 and 8 of Figure 3.4).

For family 2, the mass-distribution behaves similar to family 1 in some aspects. The mass-deposition for the minor mergers are again only marginally, varying for different inclination angles  $\Omega$  (panel 13 and 14). Also, their influence on the center of the main galaxy is, like in family 1, much more significant, which can be seen in the panels 13 and 14 of Figure 3.4.

For the smaller minor mergers, the variation of the inclination angle is much more significant. If  $\Omega \geq 30^\circ$ , the distribution is only marginally varying (panel 15 and 16), but for smaller  $\Omega$  it shows the same behavior as for family 1, it is therefore of great importance

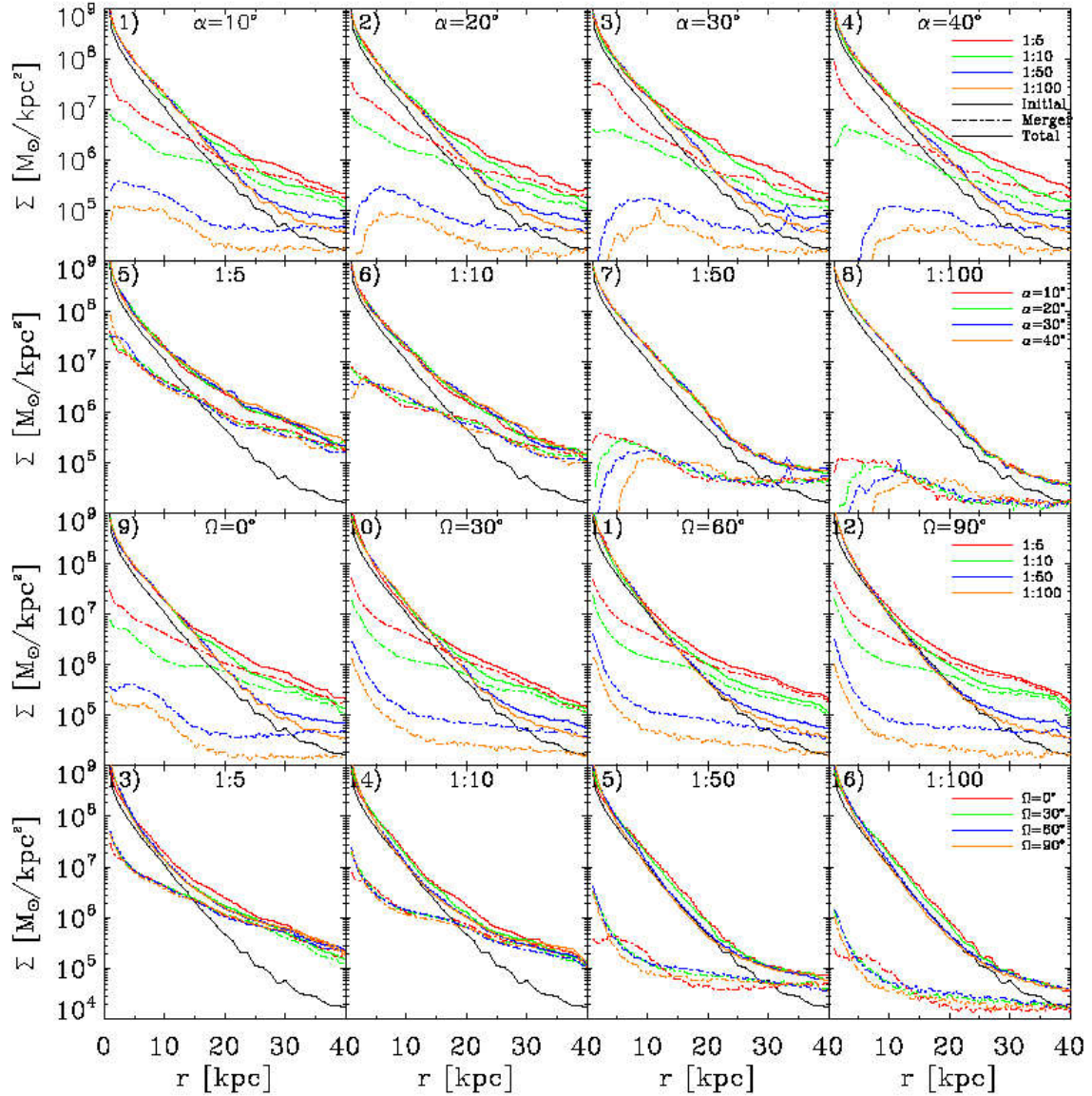


Figure 3.4: Surface density distribution for all simulations at  $\sim 3.5 Gyr$  after the beginning of the merging. The first two rows belong to family 1, while the first row compares all mass-ratios at a certain  $\alpha$ . The second row compares the mass-ratios to its different  $\alpha$ . The lower two rows regard to family 2. Here, as for the first family, for the upper row all mass-ratios are compared at a fixed  $\Omega$ , and in the lowest row the individual mass-ratios are displayed for different  $\Omega$ .

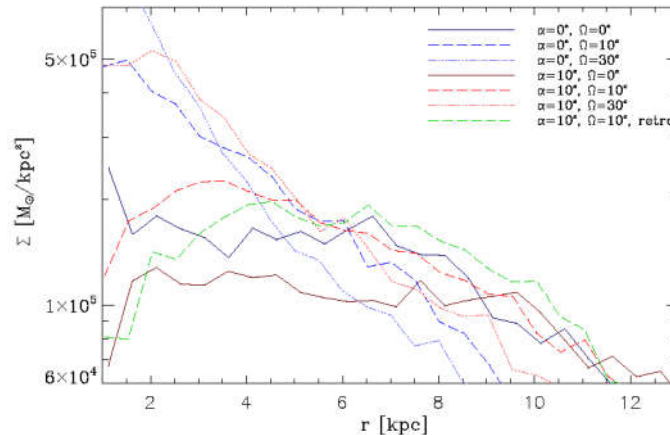


Figure 3.5: Central surface density distributions for 1:100 mergers with various orbit configurations

if the merger has to travel through the stellar disc or not.

Due to the anisotropic impact distribution of very minor mergers, which has its highest probability in the disc plane (Shao et al., 2018), we extended our set of very minor mergers for combinations of small values of  $\alpha$  and  $\Omega$ . The resulting central surface brightness distributions for these very minor mergers are displayed in Figure 3.5. For  $\alpha = 0^\circ$  and  $\Omega \geq 30^\circ$ , the density inclines steadily inwards. For low  $\Omega$  and larger  $\alpha$ , the density in the center decreases, and for  $\alpha \geq 20^\circ, \Omega = 0^\circ$  a region with lower density appears in the center. The two parameters  $\alpha$  and  $\Omega$  work opposite to each other. While an increase of  $\Omega$  increases the density in the central region, a larger  $\alpha$  decreases it and shifts the distribution outwards. In addition, one counter-rotating merger was performed (green line). It can be seen that an inversion of the rotation results in a similar density distribution with a small shift outwards compared to its co-rotating counterpart (red dashed line). However at large radii there no real difference between both mergers.

### 3.2.2 Theoretical predictions

To compare the median of the final mass distribution with the theory we want to find the distance  $R_0$  at which the tidal radius equals the half mass radius and at which therefore half of the mass should be stripped. A relation between the size of an object and  $R_0$  is deduced by Binney and Tremaine (2008), where the Jacobi radius  $r_J$  corresponds to the observational tidal radius and largest extend of the system.

$$r_J = \left( \frac{M_S}{3M_H} \right)^{1/3} R_0 \quad (3.4)$$

The medians of the mass distributions are displayed in Figure 3.6 and it can be seen

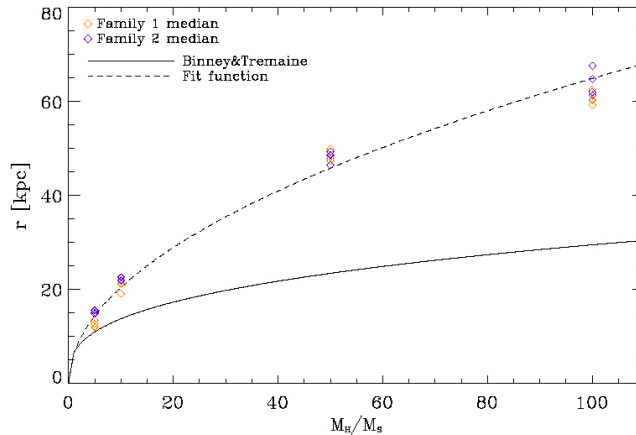


Figure 3.6: The median of the mass distribution for all family 1 and family 2 mergers compared to idealized theoretical models.

very clearly that they differ strongly from the theoretical model. The fit function yields to:

$$r_{1/2} = \left( \frac{M_S}{2.1M_H} \right)^{1/2} R_0 \quad (3.5)$$

For the minor mergers the difference is not that strong yet, especially for the 1:5 mergers, where family 1 fits the theoretical lines. But for lower mass ratios the deviation gets stronger and the mass gets deposited much further outwards than the theoretical predictions would suggest. A possible explanation for this behavior is the continuous aim of the system to re-virialize which leads to an expansion of the merger simultaneously to the stripping process. This would lead to a larger characteristic radius, lower densities and an easier stripping of the remaining mass, finally resulting in a mass deposition at larger radii. This effect has been described recently for dark matter only halos by van den Bosch et al. (2018) and would occur for galaxies as well.

### 3.2.3 Contribution to the mass-distribution by different origin

By splitting up the merger in its components it can be seen for the gas-component that it settles into the central regions of the remnant in all cases. For very minor mergers this is at the position of the initial peak. This peak has a large proportion of gas and new stars in addition to former disc- and bulge particles, which can be seen in Figure 3.7. This is in agreement with the picture of gas been removed from the outer regions of a galaxy towards the central region, feeding star formation, due to the merging process.

It can also be seen that, in general, the density of former disc particles is higher than of bulge particles, due to the higher amount of mass stored in the disc compared to the bulge.

But especially in the outer regions the bulge stars vanish, and only disc particles remain. An additional feature which is illustrated in Figure 3.7 is the peak at  $r = 64kpc$ , which is dominated by bulge particles. This peak consists of the surviving core of the merger, which is still orbiting the remnant as a bound accumulation of bulge particles, which is losing mass with every orbit.

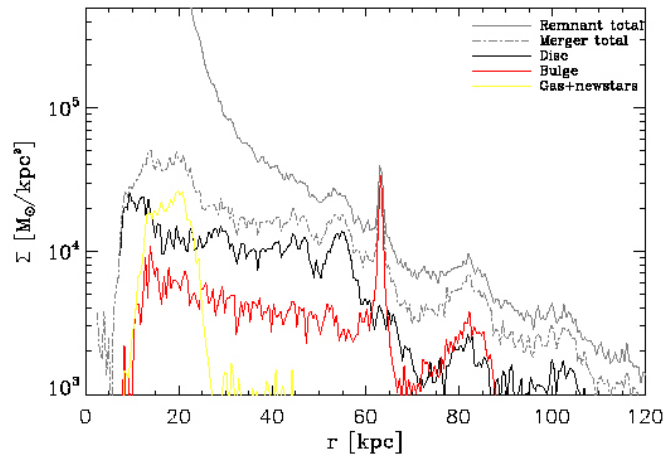


Figure 3.7: Surface density for a family 1 very minor merger (1:100) separated by origin with  $\alpha = 40^\circ$

### 3.2.4 Disc growth

With higher mass-ratios the initial disc loses its form and gets more and more isotropic as shown previously. But under certain conditions it is possible that mainly the disc increases in size without getting more isotropic in general. As displayed in Figure 3.8 for the family 2 mergers with  $\Omega = 0^\circ, \alpha = 0^\circ$ , the disc of the galaxy grows up to two times the size by an 1:100 merger and even more for the 1:50 merger. Meanwhile, the disc-height remains constant with a scale-height of  $h \approx 1.5kpc$  for both very minor mergers. With increasing mass of the merger the size of the disc is not increasing any further, but instead the disc-height starts to grow significantly. In the lower panels of Figure 3.8 this effect can be seen very dominantly.

Besides the mass-ratio, the orbit parameters are very important for such a large disc to form. An increase in disc size can only be seen while  $\Omega < 30^\circ$ . If the inclination rises to  $\Omega \geq 30^\circ$  the density distribution becomes spherical. The extension of the stellar particles by varying  $\alpha$  stays roughly constant. But for larger  $\alpha$  the overall shape of the remnant loses its disc like appearance, and it changes to a more stream dominated like structure.

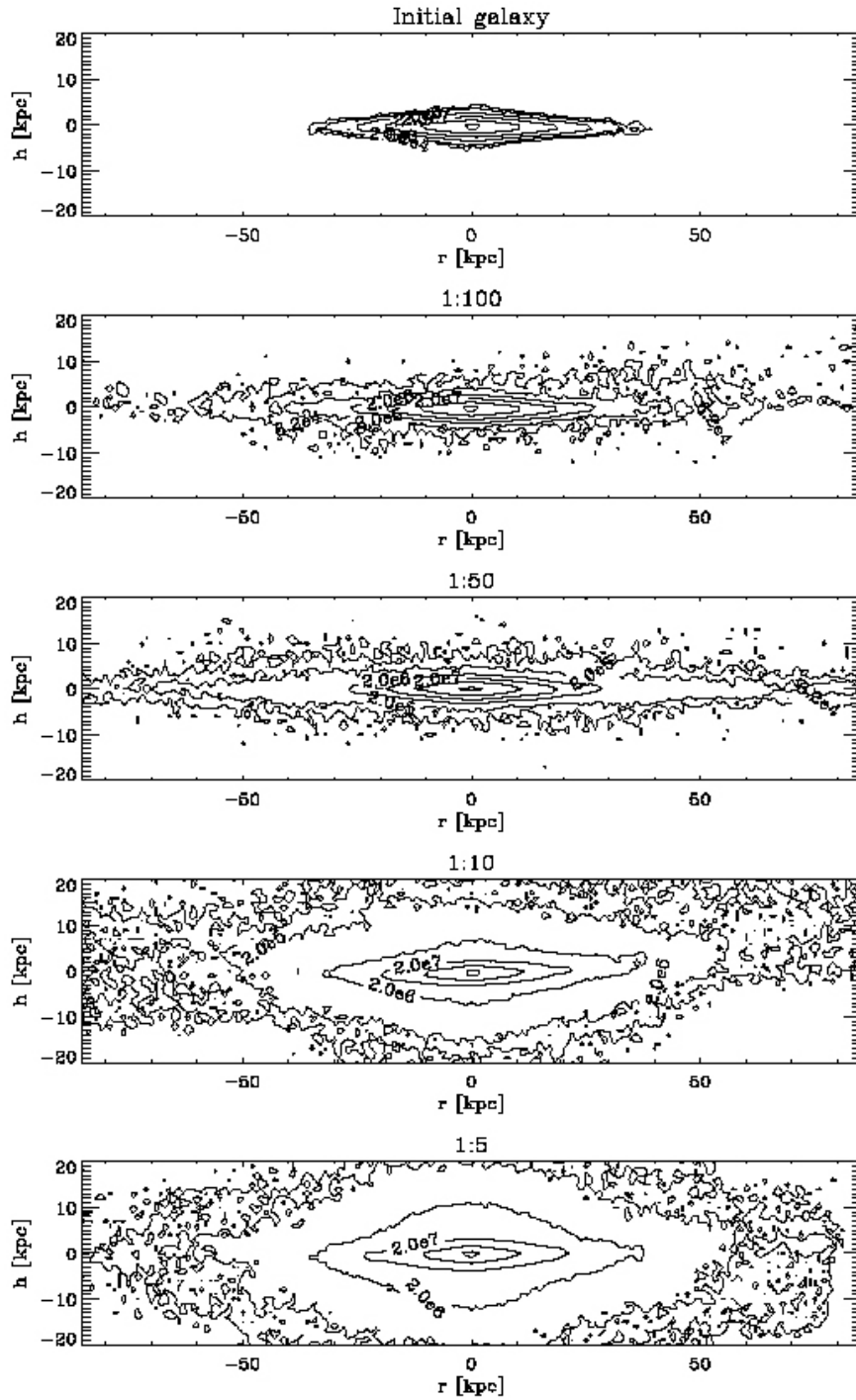


Figure 3.8: The resulting density distribution of the disc-component after a relaxation time of  $\approx 3.5Gyr$  for different mass-ratios at  $\Omega = 0^\circ$  and  $\alpha = 0^\circ$ . The contour lines are in  $M_\odot/kpc^2$ .



### 3.2.5 Shells and streams

Galaxy shells are faint ring-like structures surrounding galaxies. These shells are quite common in S0 and elliptical galaxies, and roughly 10 % of all galaxies have shells (Malin and Carter, 1983; Schweizer, 1983; Schweizer and Ford, 1985).

It can be seen in the simulations that shells only occur on flat and almost radial orbits and are more dominant for very minor mergers than for minor mergers as already stated by Hernquist and Quinn (1988) .

In these cases the merging galaxy disintegrates, and its stars begin to oscillate in the potential of the host galaxy, which create the shell like structures around the host galaxy. The shells can be separated in the phase space due to their different energy levels and their oscillation can be seen very clearly in Figure 3.9. The outermost shell is the first shell to be created by the merger, while with each orbital period a new shell with a lower energy level is evolving. This loss in energy is due to dynamical friction where the high energetic particles transfer energy to particles with lower energies of the host during their orbits. As it is illustrated in Figure 3.9, the disc component is mainly responsible for the evolution of shells and is showing clear tracks in the phase space. Due to similar energy levels the bulge particles are reinforcing the shells, but are on much more isotropic orbits and having a larger deviation in mean velocity. The gas, in contrast, doesn't show any disc like structure and is concentrated uniformly in the center.

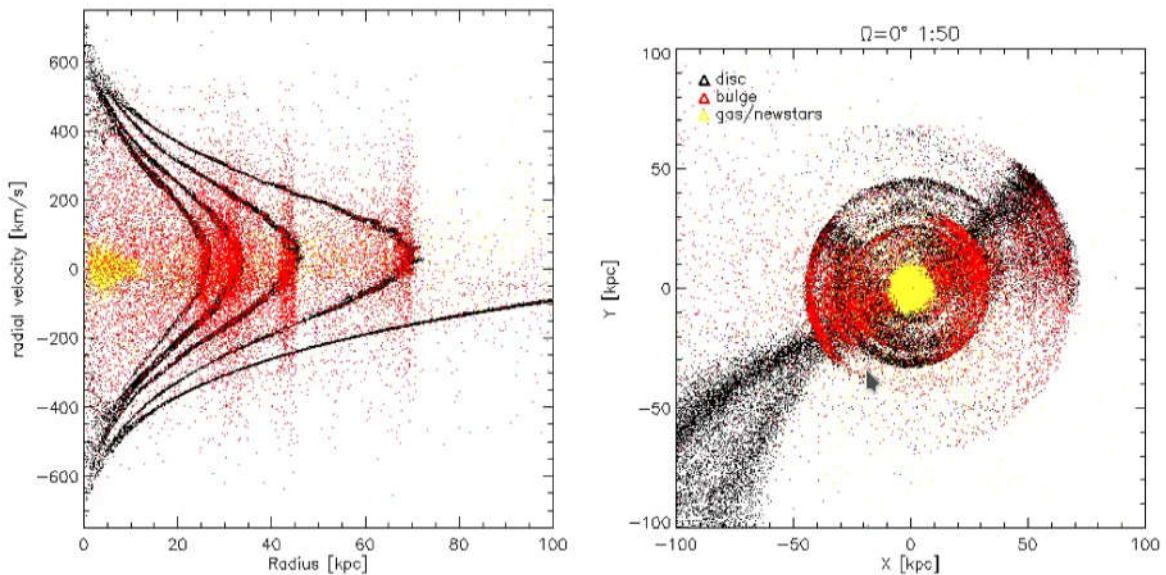


Figure 3.9: a) Galaxy shells in phase space, the different colors indicate different particle types of the merger. b) The corresponding top view of the galaxy.

For all mergers the top views can be found in Figure A.5 and A.7 of the appendix. As stated previously for the increase in disc size for larger  $\alpha$ , the shape of the remnant



changes and the shells evolve into streams. The required  $\alpha$  for the creation of shells is that  $\alpha < 10^\circ$ , and with  $\alpha \geq 30^\circ$  the shells completely transform into streams. In addition the simulations show that the lifetime of streams is much larger than of shells, which are much faster smoothed out into a continuous distribution.

### 3.2.6 Luminosity distribution

As discussed in subsection 3.2.1, the mergers are influencing the resulting shape of the remnant strongly depending on their mass-ratio and impact parameter. In order to give a rough classification of the remnant and to investigate for trends, we use the light distribution by assuming a mass to light ratio of  $M_\odot/L_\odot = 1$  and calculate the corresponding Sersic-Index (Sersic, 1968).

The Sersic-Index is the parameter  $n$  in the corresponding Sersic-profile and is responsible for the curvature of the profile:

$$I(R) = I(0) \exp(-kR^{1/n}) \quad (3.6)$$

Here  $I(0)$  is the initial intensity at  $R = 0$ ,  $k$  is the inverse of a scalelength and smaller values of  $n$  lead to less concentrated profiles and shallower profiles. For all mergers of both families, the variation of the Sersic-index due to the merger event follows the same behavior, which can be seen exemplarily in Figure 3.10, all profiles can be found in the Figures A.10 and A.11 in the appendix.

For all mergers of both families, the variation of the Sersic-index due to the merger event follows the same behavior. While the initial galaxy has an index  $n \approx 1.3$ , which gets quite close to the index of an idealized exponential late type galaxy. It varies after the collision, mainly depending on the different mass-ratios. For the 1:5 merger the remnant results in an index of  $n \approx 3.5 - 6.5$ , which would correspond to an index of an early type galaxy. The index of the remnant is decreasing with higher mass-ratios, the 1:10 mergers result in  $n \approx 2.2 - 4.5$ , a value neither corresponding to late nor early type galaxy. With a mass-ratio of 1:50 the index reaches  $n \approx 1.3 - 2.0$  and the 1:100 mergers in  $n \approx 1.3 - 1.4$  which is almost identical with the initial index. This leads to the conclusion that very minor mergers are not able to disturb the host disc-galaxy in a significant manner which is in agreement with common knowledge. Interestingly, the orbit for very minor mergers play almost no role, while for minor mergers the impact on the profile is of much larger importance and the spread in  $n$  is much larger. This spread is due to the orbital parameter  $\omega$ , while lower  $n$  are reached with lower  $\Omega$ . This result is explainable by the buffer the disc builds against incoming particles, so particles coming from a flat orbit are distributed more evenly and onto larger scales than ones coming from higher inclined orbits. The results are similar to when the Einasto profiles (Einasto, 1965) are calculated for all remnants.

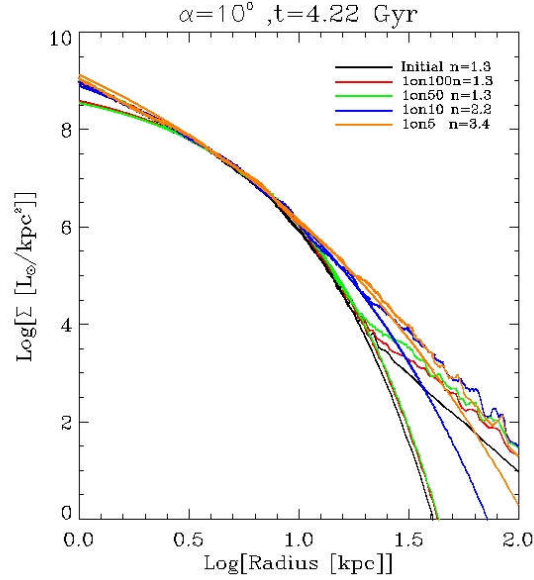


Figure 3.10: Sersic profiles for mergers with different mass-ratios at  $\alpha = 10^\circ$ .

### 3.2.7 Radial anisotropies

To quantify the systems degree of radial anisotropy, we calculate the anisotropy parameter  $\beta$  as described by Binney and Tremaine (2008):

$$\beta = 1 - \frac{\sigma_\theta^2 - \sigma_\phi^2}{2\sigma_r^2} \quad (3.7)$$

Here  $\sigma_\theta$ ,  $\sigma_\phi$  and  $\sigma_r$  are the velocity dispersions corresponding to the unit vector in spherical coordinates which are calculated by:

$$\sigma_i = \sqrt{\frac{1}{N} \sum_{n=1}^N (x_n - \bar{x})^2}. \quad (3.8)$$

In the idealized case of only circular orbits ( $\sigma_r = 0$ ) this would lead to  $\beta = -\infty$ . If  $\beta = 0$ , then the radial the distribution function (DF) is ergodic. At the maximum of  $\beta = 1$ , all orbits would be perfectly radial ( $\sigma_\theta = \sigma_\phi = 0$ ). Anisotropies with  $\beta > 0$  are called radially biased, and if  $\beta < 0$  tangentially biased.

For the initial galaxy, the DF is constantly strongly radially biased for all radii. In Figure 3.11 the anisotropy profile of a 1:50 merger at  $\alpha = 10^\circ$  is displayed. It can be seen how the merging component has an ergodic profile and how it is causing a dip in the total profile by disturbing the host galaxy.

For all mergers the DF becomes more tangentially biased, but only in the inner regions up to  $r < 20kpc$ . Here the mass-ratio is the main source of influence, while minor mergers

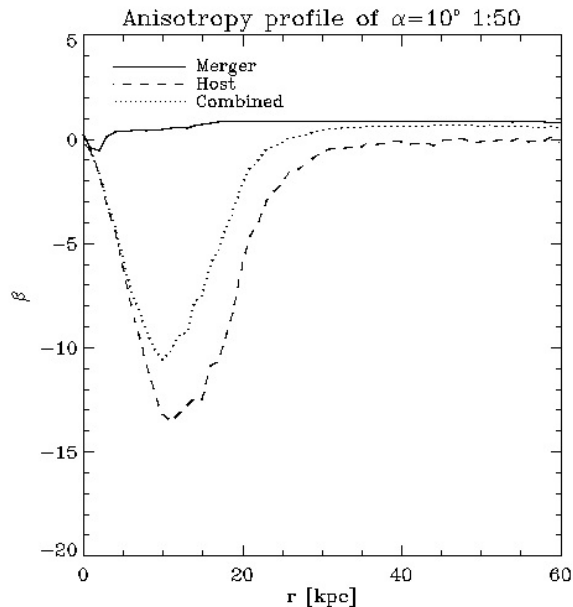


Figure 3.11: Radial anisotropy profile of a 1:50 merger at  $\alpha = 10^\circ$ .

only have a low impact and shift the anisotropy to  $\beta \sim -4$ , intermediate mergers reach values of up to  $\beta \sim -17$ . In general for all family 1 mergers with same mass-ratio, the DFs look similar. For family 2, this is only valid for the minor mergers, which are also similar to the ones of family 1. For the very minor merger their impact on the DF increases with increasing  $\Omega$ . In case of the 1:100 mergers of family 2 this results in values of  $\beta \sim -4$  for  $\Omega = 0^\circ$  up to  $\beta \sim -8$  for  $\Omega = 90^\circ$ . All profiles can be found in the appendix in Figure A.10 and A.11.

### 3.3 Conclusion

It is well known that galaxy mergers are of great importance for their evolution and also happen quite frequently, especially the very minor ones. And albeit the fact that cosmological simulations have now reached resolution levels where they are even able to resolve individual galaxies, idealized merger simulations are still essential to study the impact of galaxy mergers in detail.

One of the main results is that, independent of the orbit, minor mergers are depositing a way larger amount of their mass inside of the remnant galaxy than very minor mergers. Nevertheless, the complete outer halo is build of particles initially belonging to the merging galaxy. For very minor mergers most of its mass is deposited in the outer halo of the remnant. In addition, a variation of orbit parameters have in general a low impact on minor mergers, while for very minor mergers they are of great importance. This can be clearly seen as for orbits with pericentric distances of at least  $d_p = 7kpc$ , very minor mergers

are not able to deposit their mass in the center of the remnant, but build a ring structure around the center, which radius is depending on the impact parameter. Interestingly, the orbit parameters  $\alpha$  and  $\Omega$  influence the mass-distribution inversely and with a similar weighting for small values while an inversion of the internal rotation of the merger only yields to a minor effect. The median of the merger mass is also located at much higher radii than the theoretical models would predict which is a clear indicator for the importance of particle-particle interactions which usually are neglected in simplified models.

In addition, minor mergers are always disturbing the host galaxy in a significant manner and are able to introduce a crucial amount of disturbances to change the galaxies type from a initial late type galaxy to an early type galaxy. Very minor mergers, on the other hand, are not able to have a significant impact on the host galaxy and are therefore a process by which a galaxy can grow in mass without changing its type. Nevertheless, here the impact of the orbit can be seen very clearly, as orbits with higher inclinations increase the Sersic-index much more than mergers with flat orbits. For these orbits the disturbances are damped by the disc of the host galaxy.

But despite their minor impact on the host galaxy minor mergers are able to significantly increase the disc size of the host. This effect can only be seen for flat orbits and almost direct hit orbits, even small deviations in the orbit lead to a significantly alternate resulting shape. Regarding the orbit this behavior goes in sync with the occurrence of galaxy shells, which are only forming if the orbit is ideally within  $10^\circ$  and at an absolute maximum limit of  $< 30^\circ$  of the disc plane. For larger angles in the disc plane, streams are formed instead of shells. This leads to the conclusion, assuming isopheric and centralized infall, that in  $> 50\%$  of all of these orbits it is impossible to produce shells and the probability for orbits which most likely produce shells is  $\sim 17\%$ .

It has also been displayed how the origin of the particles is important for their final position. While during the process of merging, the gas gets always stripped from the merger and accumulates in the central regions of the remnant. The disc and bulge component are in contrast to the gas component distributed about evenly until in in the furthest outskirts mainly disc particles remain and therefore mainly former disc particles are responsible for the beautiful structures like shells and streams.

## 4. Summary and conclusion

In this thesis interaction between galaxies in cosmological and idealized environments were studied. On the one hand, using cosmological zoom simulations it is possible to simulate objects with different environments at higher resolution than in a cosmological box. This allows to reduce the computational costs without losing the complex environment and achieving objects with unique evolutionary histories. The parameter study of idealized merger simulations on the other hand has the advantage of having a determined set of initial conditions and even higher resolutions than the zoom simulations. This allows to study certain aspects of the interaction in much higher detail in an closed environment without further disturbances, but lacking the complex cosmological environment. The combination of these two techniques gives a very powerful approach to understanding the formation and evolution of galaxies in highly interacting environments.

It was found that compact galaxy groups are physically dense objects and not projection effects. Also, hints were found that one possible final phase of compact groups are giant elliptical galaxies in isolated environments, so called fossil groups. Further more it could also be seen how the gas decouples and builds up a hot halo additionally to interactions, the IGL forms from the accretion of stellar systems. The IGL needs time to be build up to cover all group members but is contributing significantly to the total stellar mass of the group. This IGL and the corresponding structures like streams and shells were studied in detail with idealized merger simulations. It was found that mergers always deposit significant amounts of mass in the outer stellar halo of the remnant, and are therefore the main origin of the IGL stellar component. Interestingly, the much more frequent minor and very minor mergers contribute, percentaged of their individual mass, more to the outer stellar halo than more massive mergers. These major and intermediate mergers have, on the contrary, much larger impact on the morphology of the host galaxy. It can therefore be concluded that the morphology of galaxies is mainly influenced by major or intermediate mergers, while the outer stellar halo, and therefore the IGL, is enriched mainly by minor and very minor mergers.



# A. Appendix

## A.1 Compact galaxy groups

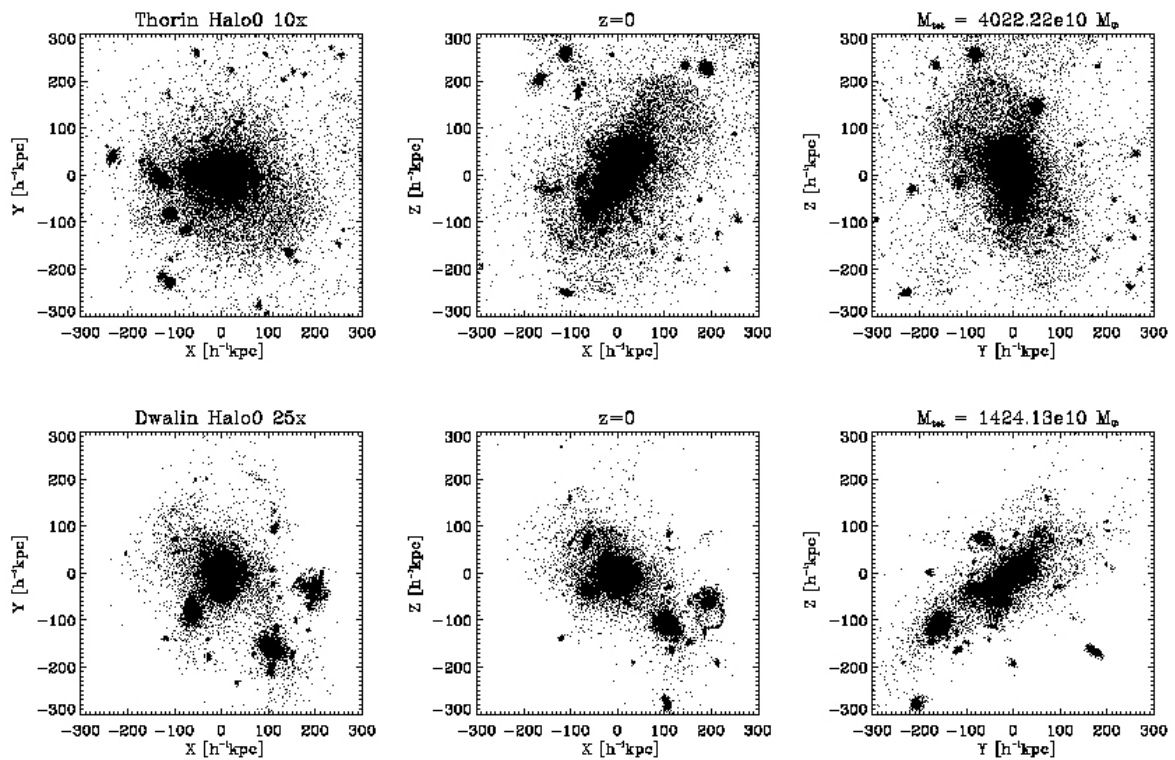


Figure A.1: Image of the stellar component of the halos Thorin 0 and Dwalin 0 at  $z = 0$  in different projections.

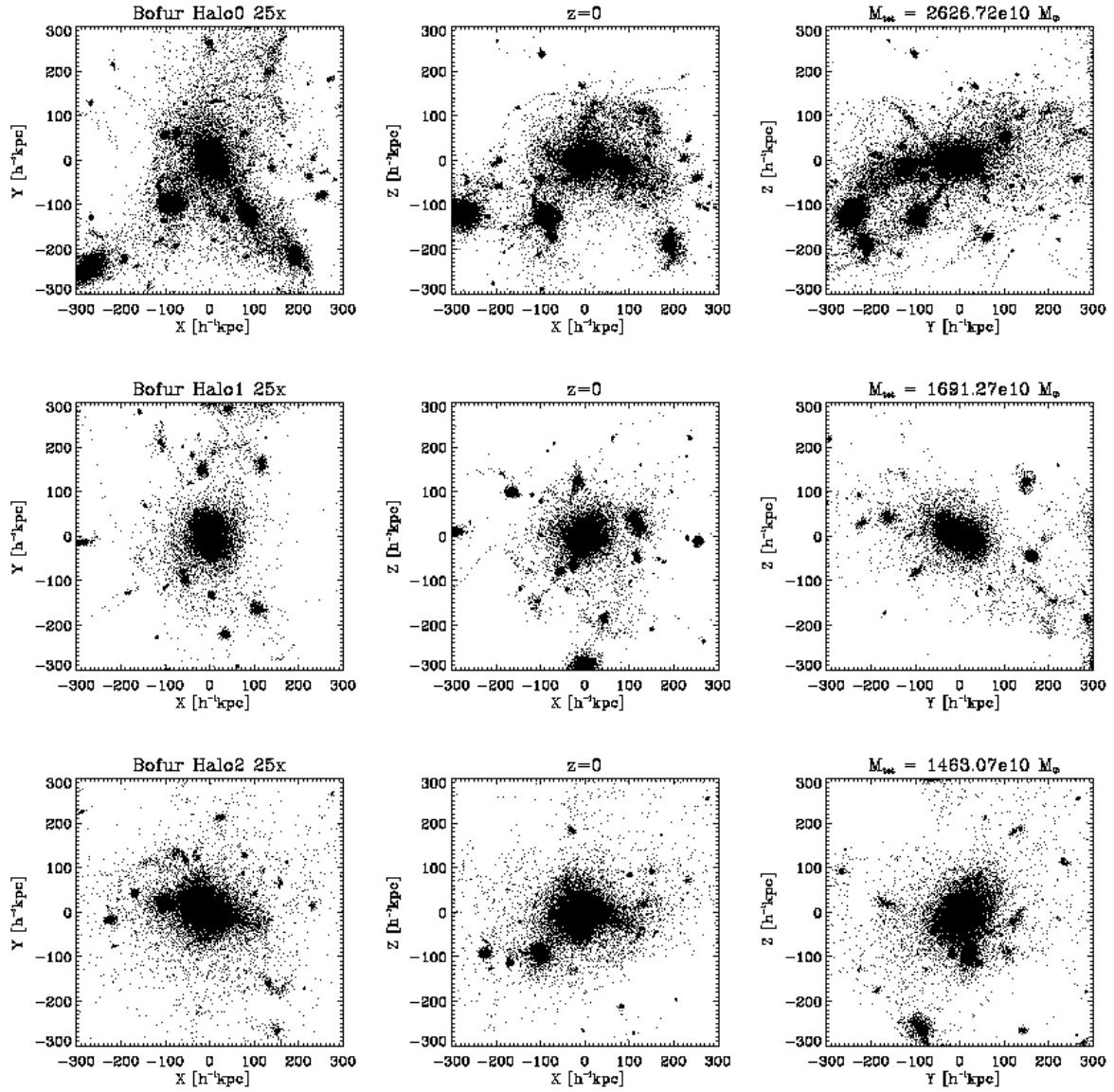


Figure A.2: Image of the stellar component of the halos Bofur 0, Bofur 1 and Bofur 2 at  $z = 0$  in different projections.



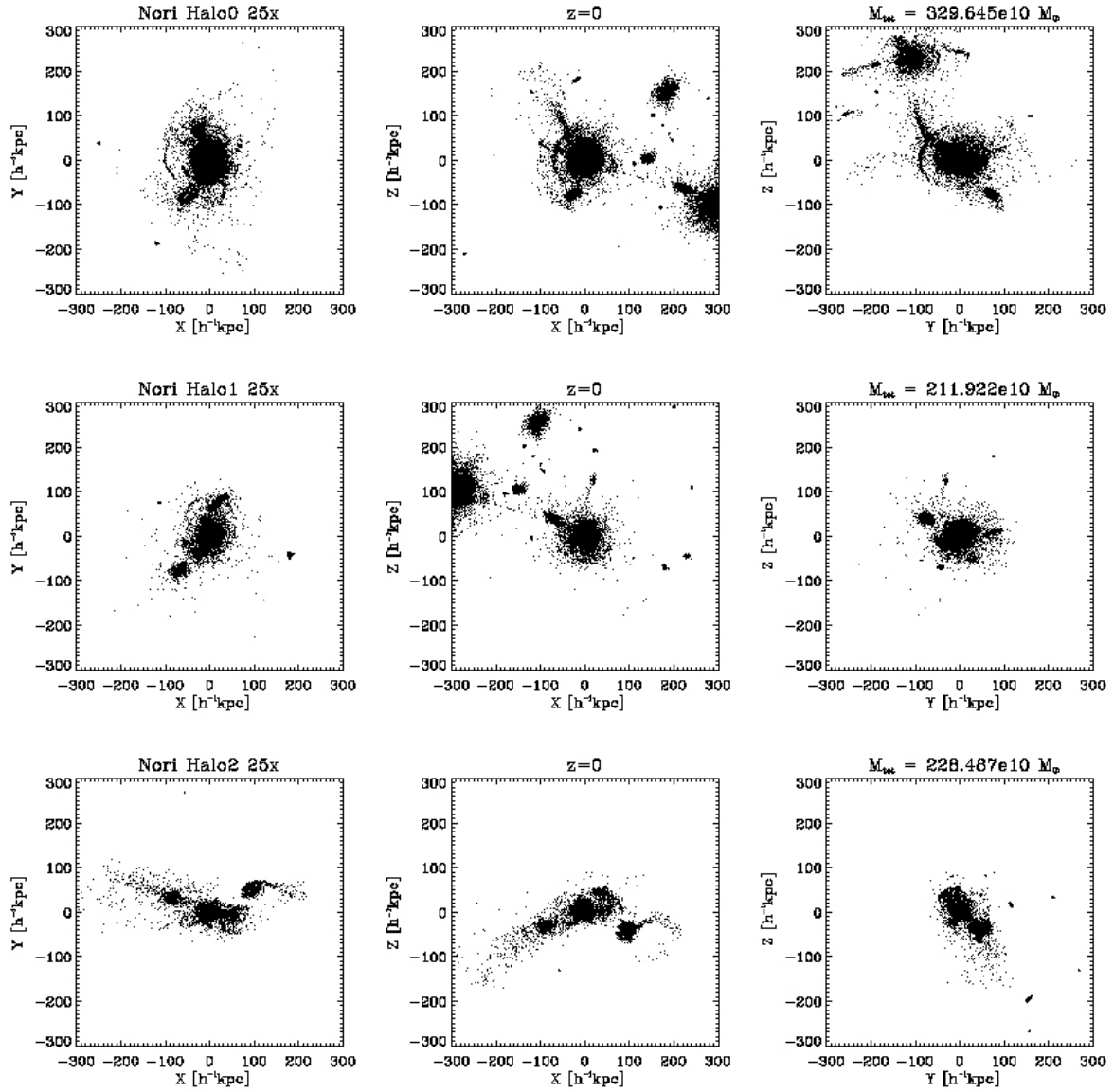


Figure A.3: Image of the stellar component of the halos Nori 0, Nori 1 and Nori 2 at  $z = 0$  in different projections.

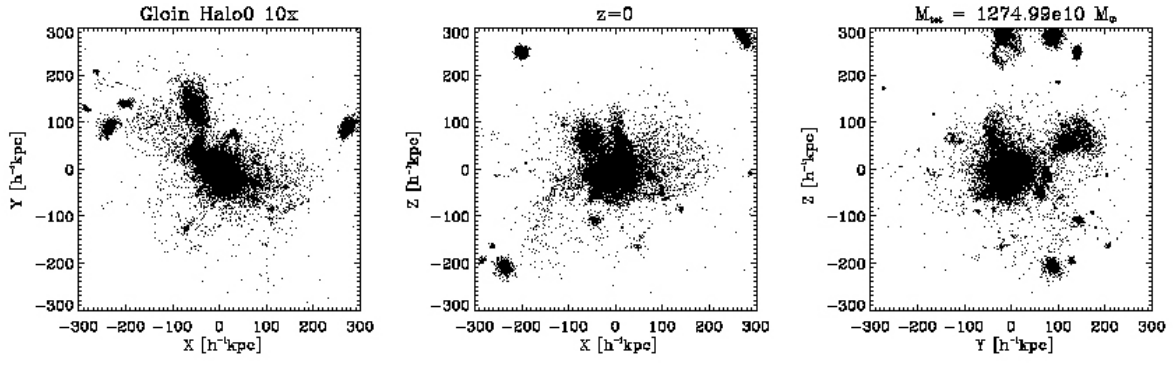


Figure A.4: Image of the stellar component of Gl0in 0 at  $z = 0$  in different projections.

## A.2 Galaxy mergers

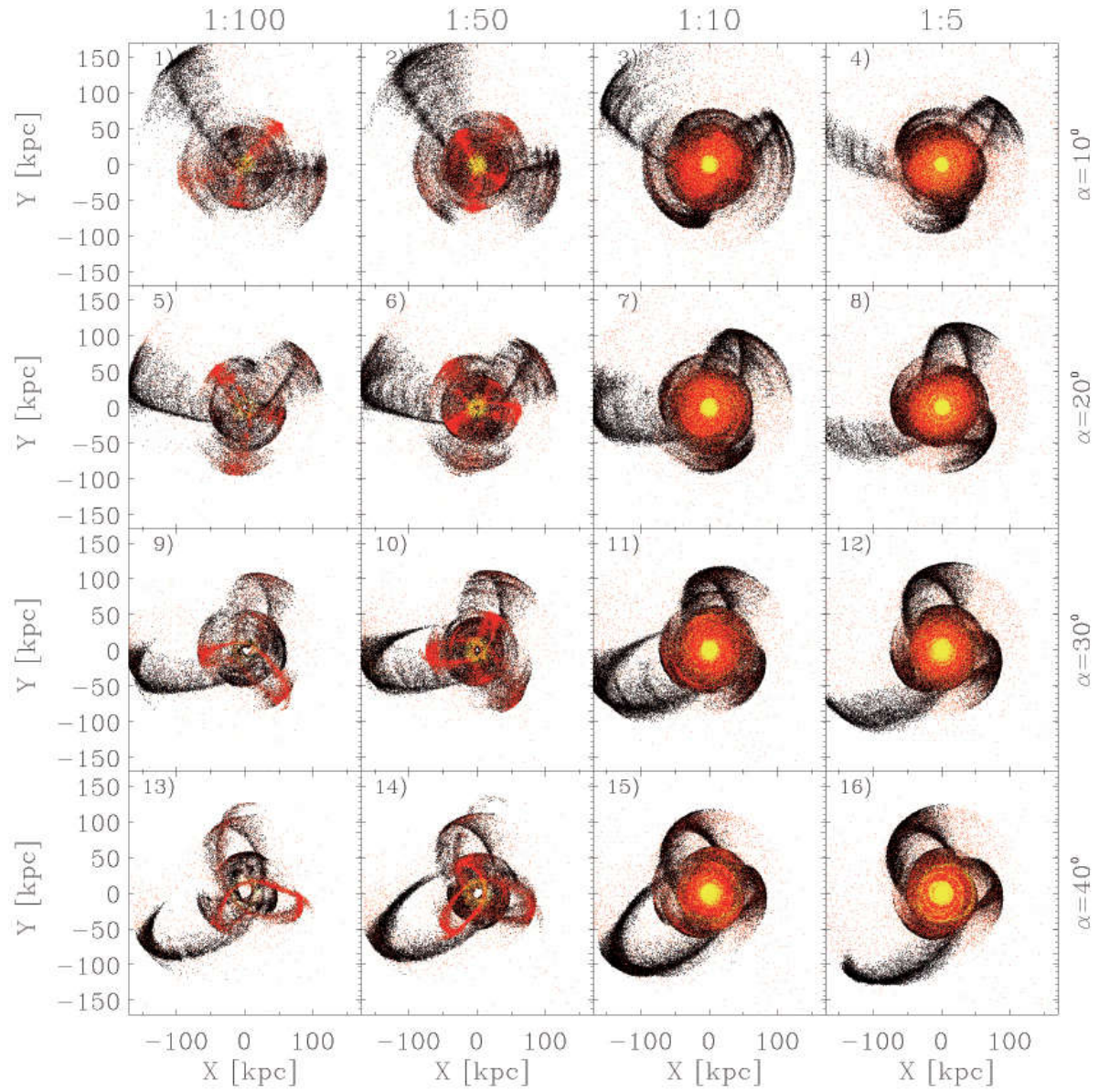


Figure A.5: Top view of all merger particles after  $\approx 3.5 Gyr$  of the collision for all family 1 mergers separated by their part-types (yellow: gas and new stars, red: bulge, black: disc).

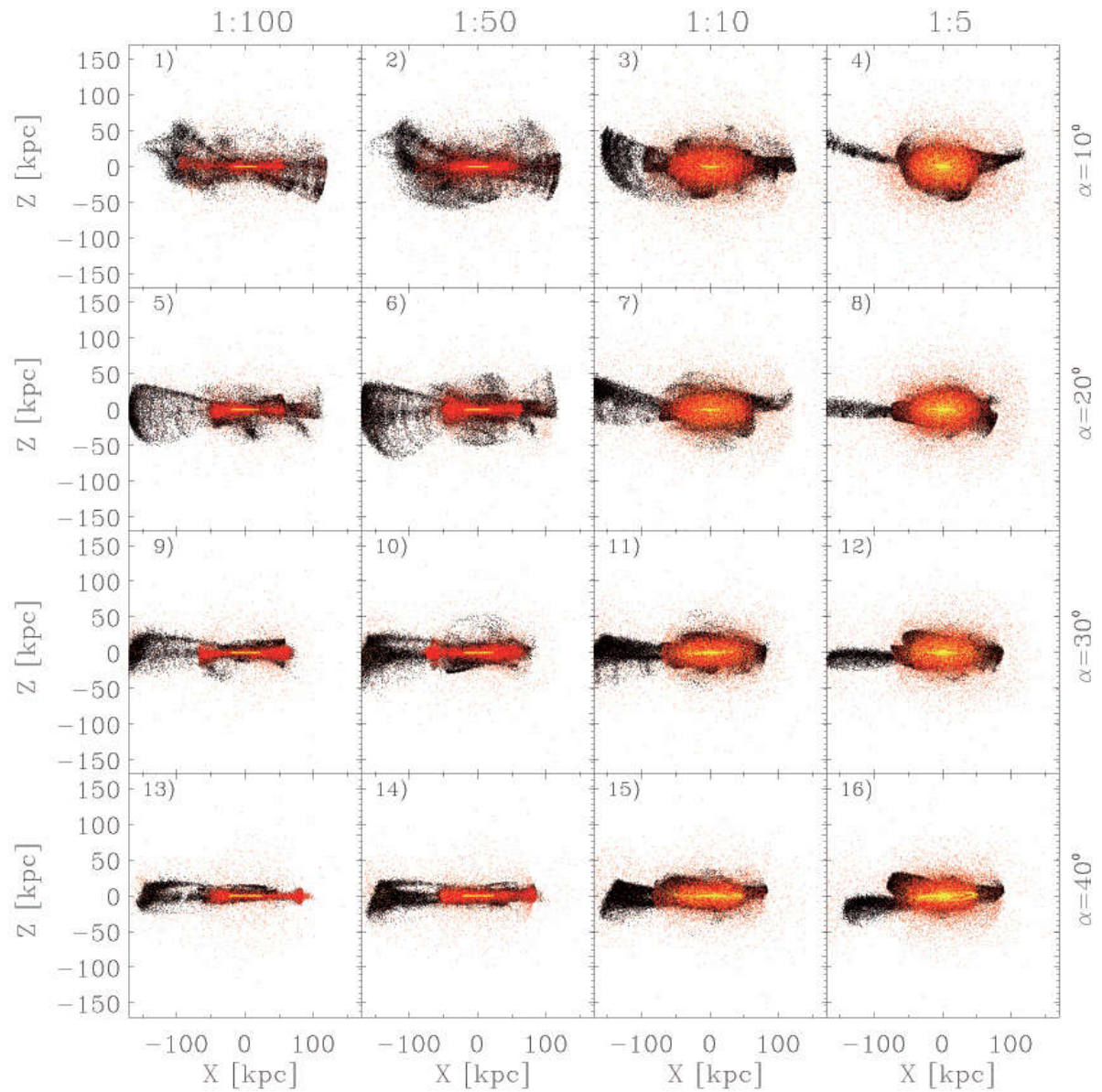


Figure A.6: Side view of all merger particles after  $\approx 3.5 Gyr$  of the collision for all family 1 mergers separated by their part-types (yellow: gas and new stars, red: bulge, black: disc).



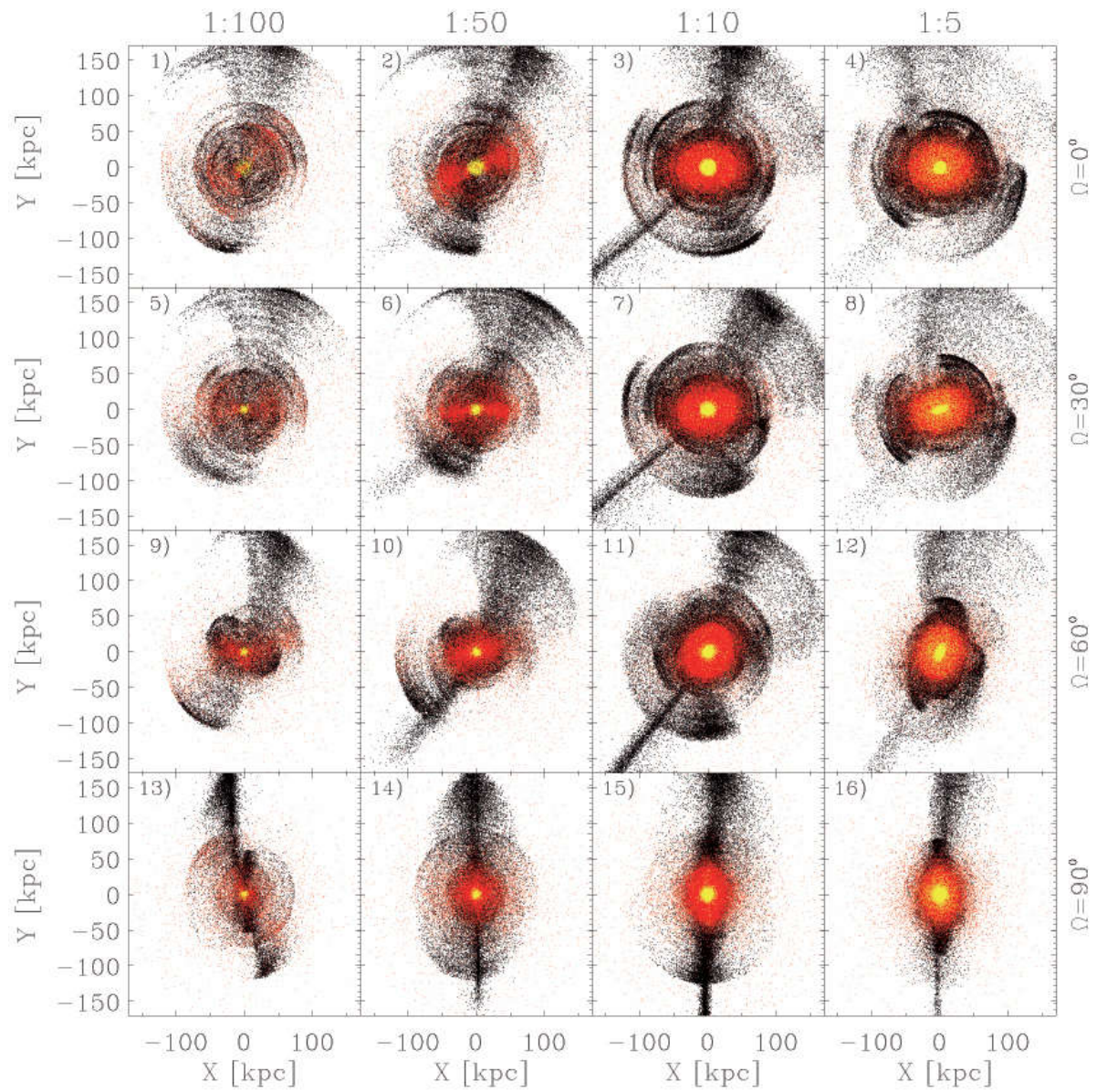


Figure A.7: Top view as in figure A.5 for all family 2 mergers.

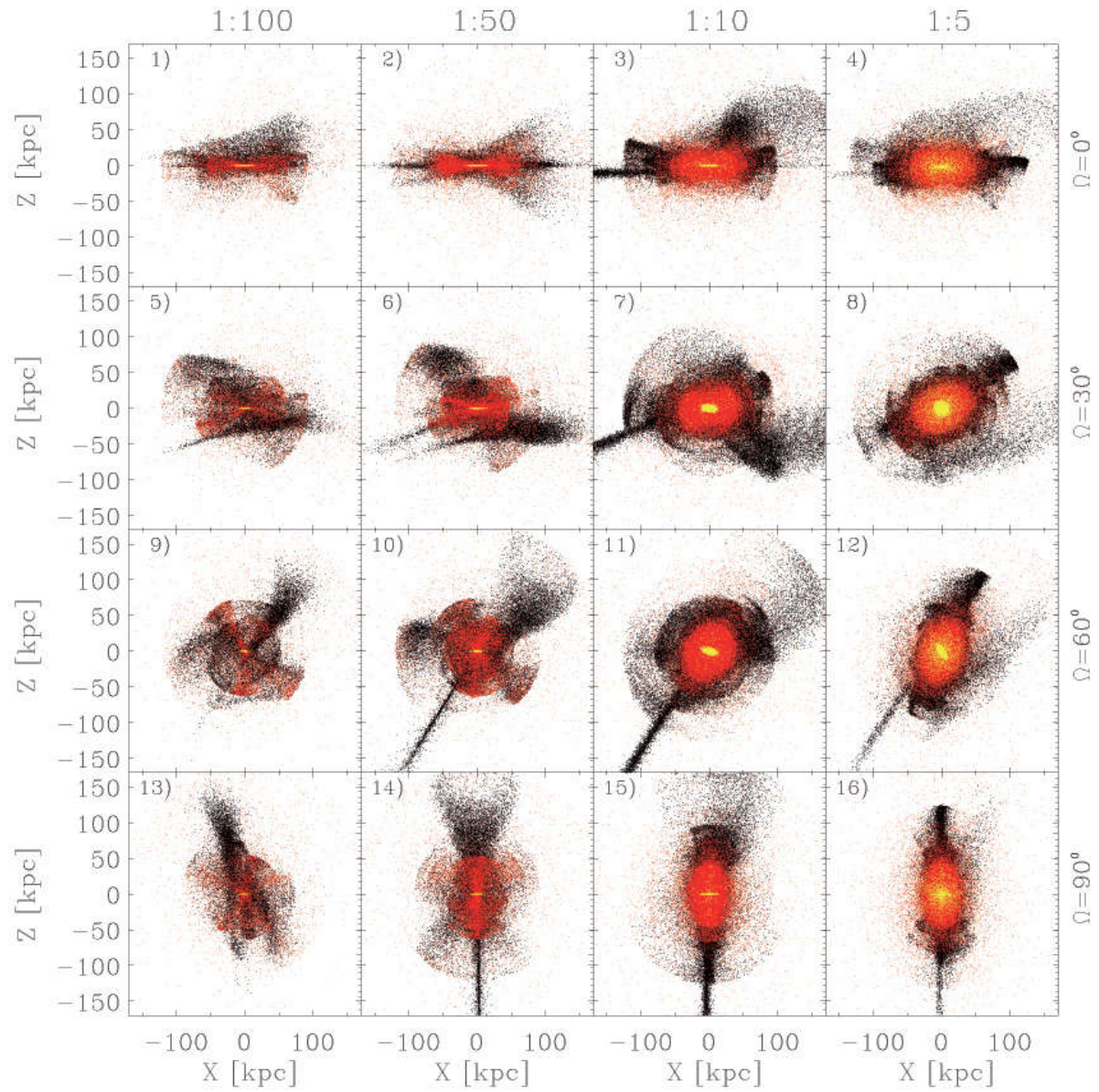


Figure A.8: Side view as in figure A.6 for all family 2 mergers.



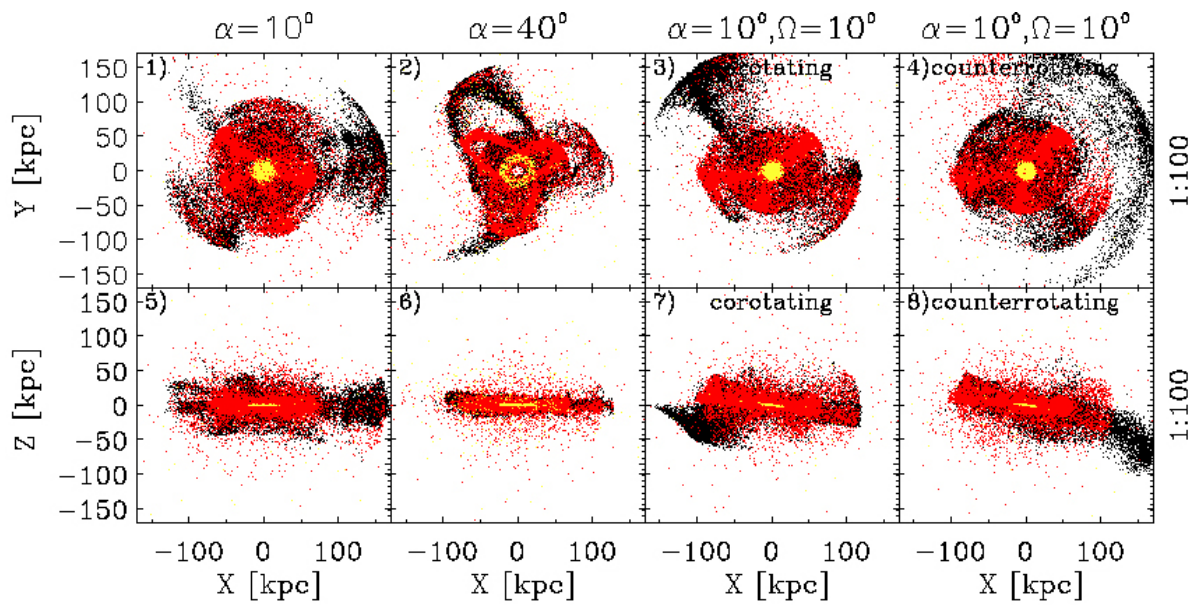


Figure A.9: Top and side view of merger particles for four special mergers. These were ran for longer time until  $t = 6.18Gyr$  (panel 1,2,5 and 6) and two mergers, where one is counterrotating and the other corotating (panels 3,4,7 and 8) at  $t = 4.2Gyr$ .

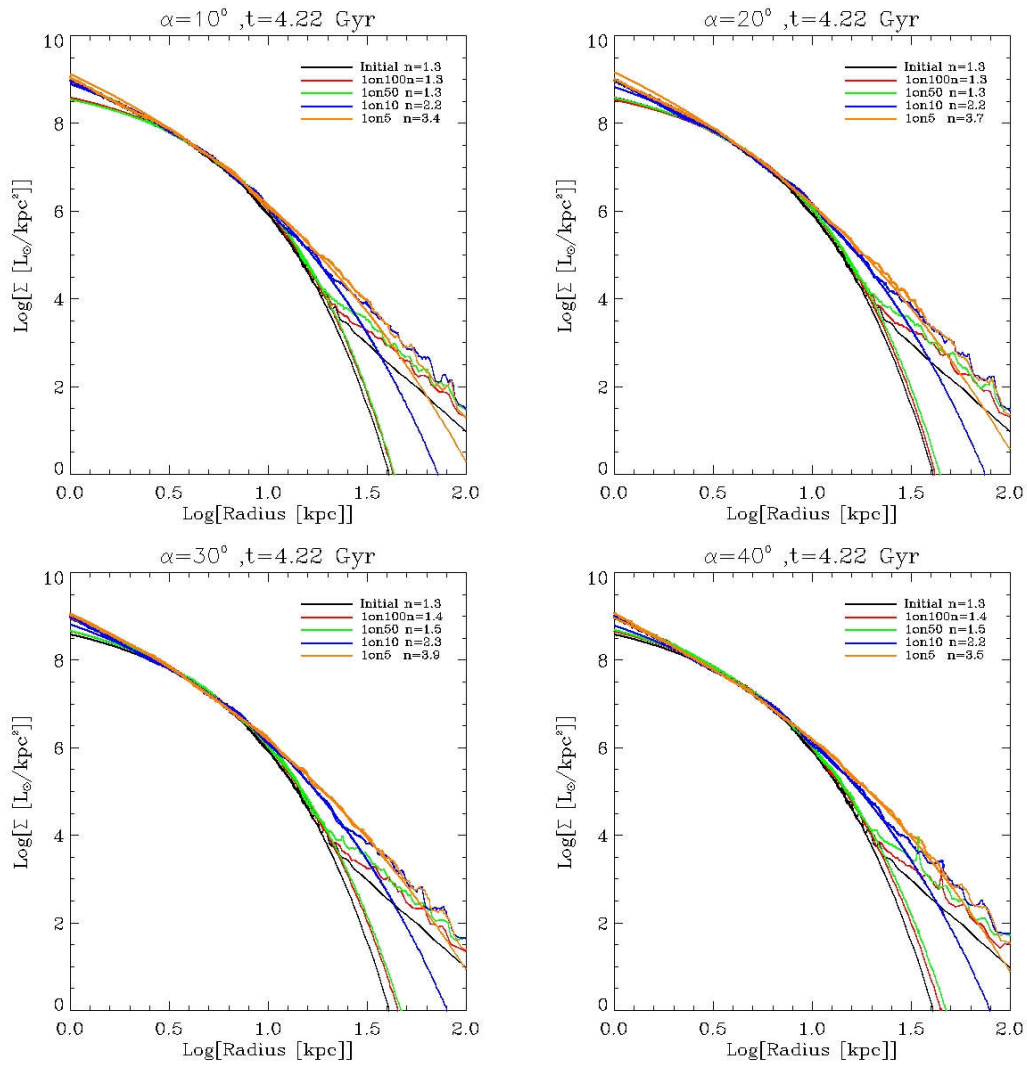


Figure A.10: Sersic profiles for all family 1 mergers.



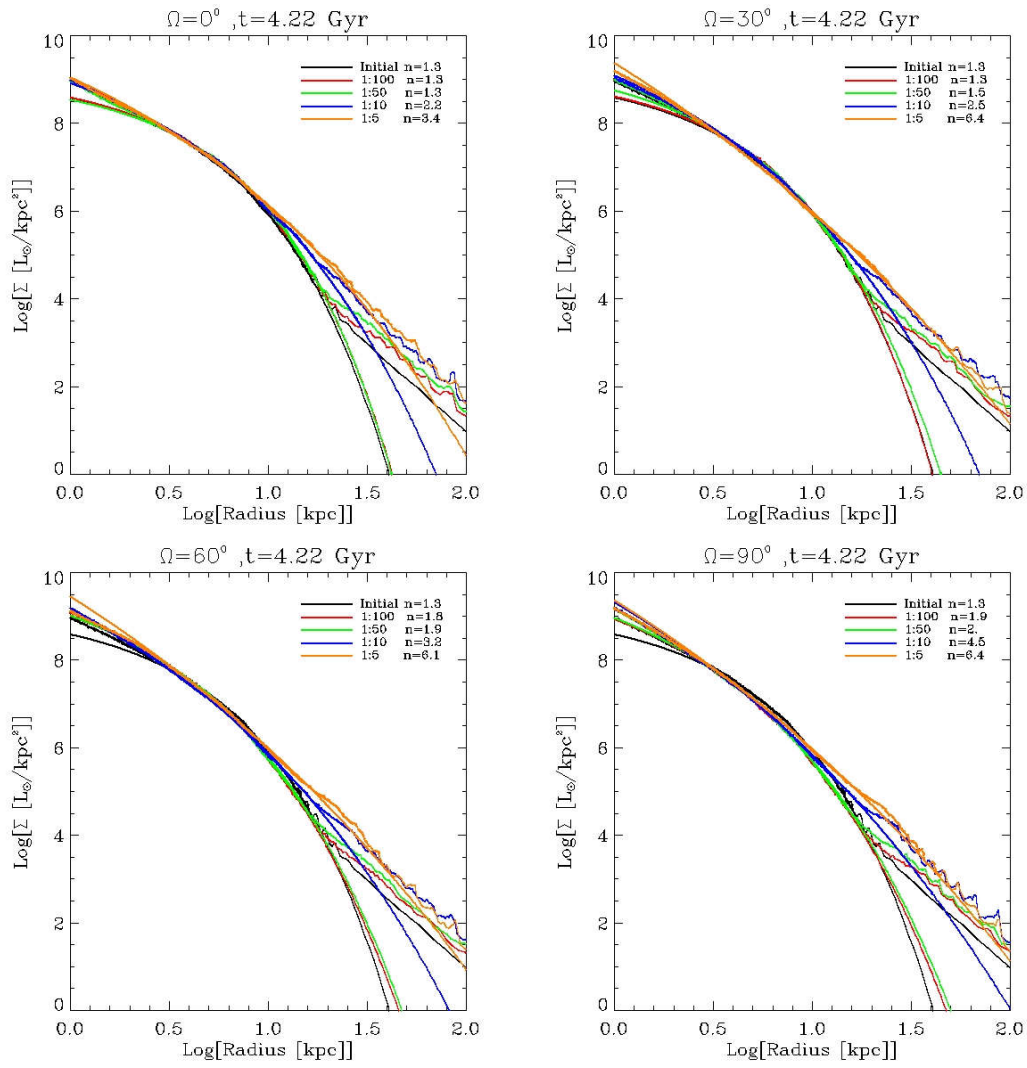


Figure A.11: Sersic profiles for all family 2 mergers.

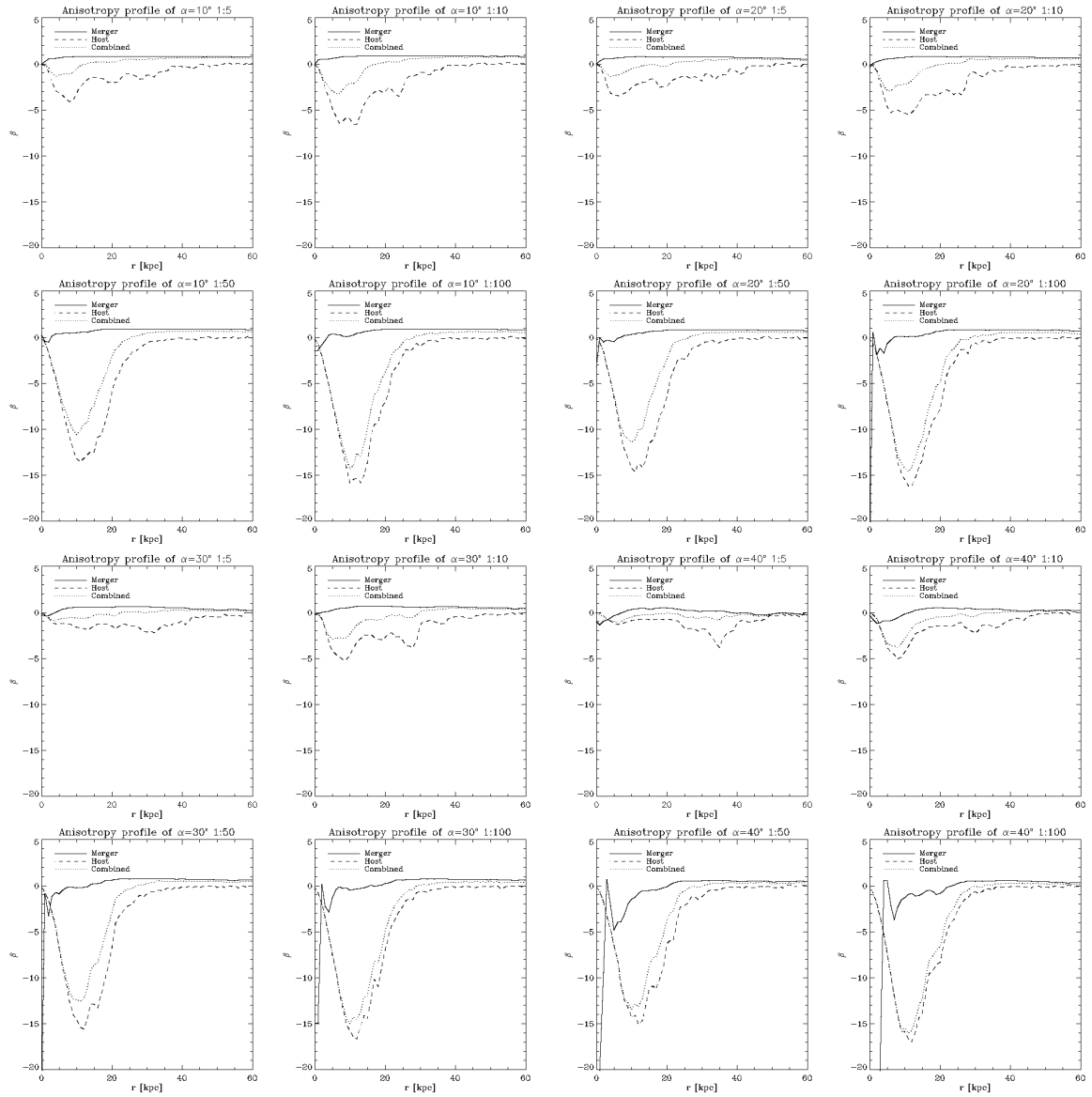


Figure A.12: Radial anisotropy for all family 1 merger at  $\approx 3.5Gyr$  after the collision.

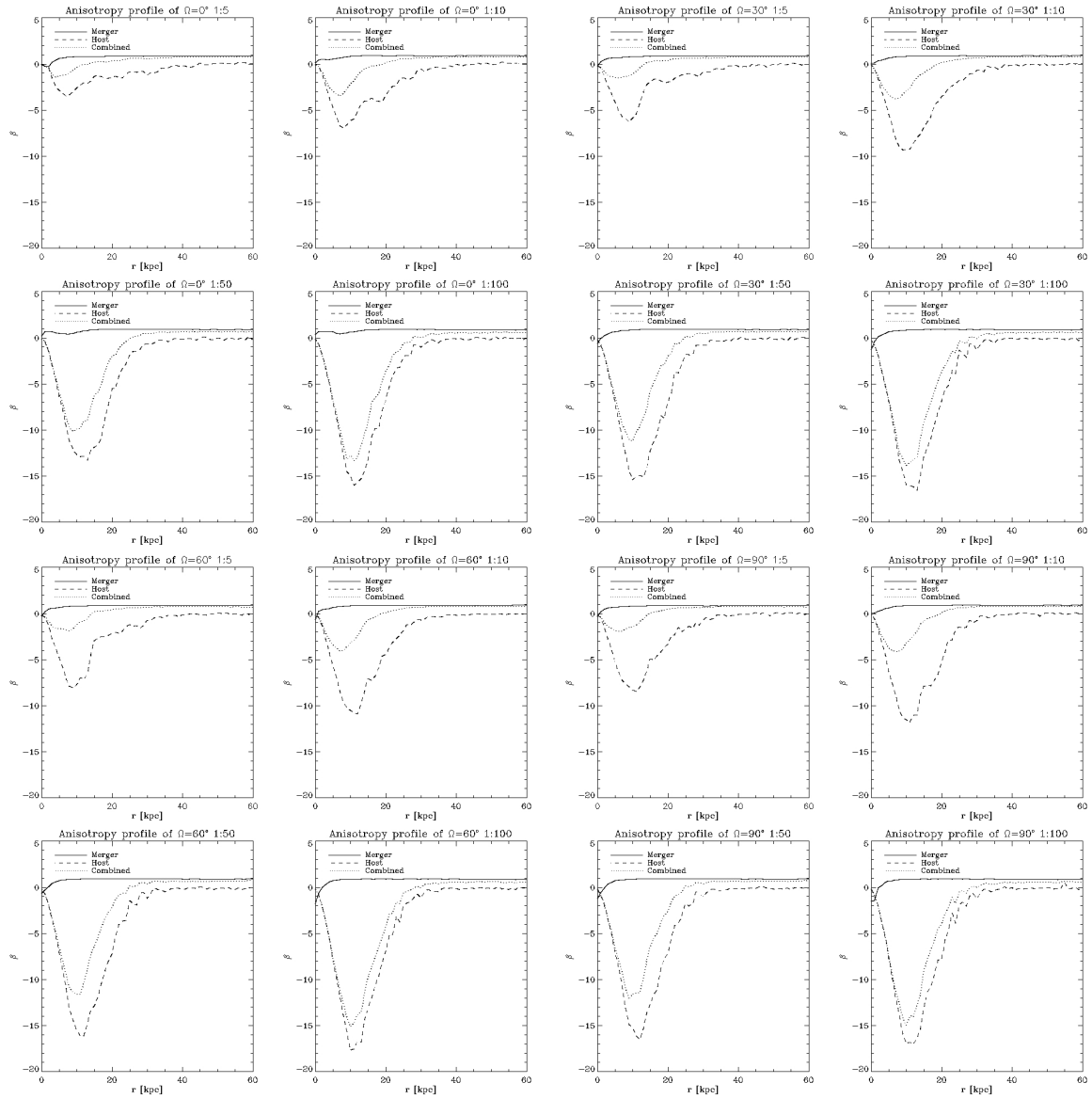


Figure A.13: Radial anisotropy for all family 2 merger at  $\approx 3.5Gyr$  after the collision.



# List of Figures

1.1	De-Vaucouleurs-System (Ciccolella and Leo)	1
1.2	Morphology-density relation Dressler (1980)	3
1.3	DIANOGA	4
2.1	Stephans Quintett (HubbleSite)	7
2.2	Visualisation of a simulated compact group	10
2.3	Distance halo selection criteria	11
2.4	Object environment in DIANOGA	12
2.5	Densities of the environment of the objects	13
2.6	IoCC region	14
2.7	Initial conditions by ZIC	15
2.8	Object cleaning	16
2.9	First step of Graham scan	18
2.10	Convex hull	19
2.11	Smallest enclosing circle	21
2.12	Resolution limitation	22
2.13	Compact group classification	24
2.14	Lifetime of compact groups	25
2.15	Intragroup light of Bofur 0 at $z \approx 0.13$	26
2.16	Velocity histogram of Thorin 0	27
2.17	IGL and total mass fraction	28
2.18	$b$ -value of main galaxies in Thorin 0 and Bofur 0	29
2.19	Specific angular momentum vs. stellar mass	30
2.20	Mass-size relation and evolution	31
2.21	Thorin 0 at $z = 0$	32
2.22	Nori 0 in three projections	33
2.23	Mergers and their influence on the $b$ -value	34
3.1	Visualization of a 1:5 merger	37
3.2	Softeningtest	40
3.3	Geometrical set-up of the merger orbits	41
3.4	Surface density distribution	43
3.5	Central surface density distributions for various 1:100 mergers	44

3.6	Median of the mass distribution for all merger compared to idealized theoretical models . . . . .	45
3.7	Surface density for a family 1 1:100 merger at $\alpha = 40^\circ$ . . . . .	46
3.8	Density distribution of the disc-component . . . . .	47
3.9	Galaxy shells . . . . .	48
3.10	Sersic profiles for all mergers at $\alpha = 10^\circ$ . . . . .	50
3.11	Radial anisotropy profile of a 1:50 merger at $\alpha = 10^\circ$ . . . . .	51
A.1	Stellar component of the halos Thorin 0 and Dwalin 0 at $z = 0$ . . . . .	55
A.2	Stellar component of the halos Bofur 0, Bofur 1 and Bofur 2 at $z = 0$ . . . . .	56
A.3	Stellar component of the halos Nori 0, Nori 1 and Nori 2 at $z = 0$ . . . . .	57
A.4	Stellar component of Gloin 0 at $z = 0$ . . . . .	58
A.5	Top view of all merger particles for family 1 . . . . .	59
A.6	Side view of all merger particles for family 1 . . . . .	60
A.7	Top view of all merger particles for family 2 . . . . .	61
A.8	Side view of all merger particles for family 1 . . . . .	62
A.9	Side and top view of special mergers . . . . .	63
A.10	Family 1 Sersic profiles . . . . .	64
A.11	Family 2 Sersic profiles . . . . .	65
A.12	Radial anisotropy for family 1 . . . . .	66
A.13	Radial anisotropy for family 2 . . . . .	67

# List of Tables

- 2.1 Main parameters of the objects . . . . . 12
- 2.2 Resolution steps . . . . . 16
- 2.3 Masses of the largest halos at different resolutions . . . . . 23
- 2.4 Halo information . . . . . 25
- 2.5 Mass-size relation parameters . . . . . 31
  
- 3.1 Main parameters of the created galaxies . . . . . 40
- 3.2 Comparison between  $\alpha$  and the pericentric distance . . . . . 41





# Bibliography

- O. Agertz, B. Moore, J. Stadel, D. Potter, F. Miniati, J. Read, L. Mayer, A. Gawryszczak, A. Kravtsov, Å. Nordlund, F. Pearce, V. Quilis, D. Rudd, V. Springel, J. Stone, E. Tasker, R. Teyssier, J. Wadsley, and R. Walder. Fundamental differences between SPH and grid methods. *MNRAS*, 380:963–978, Sept. 2007. doi: 10.1111/j.1365-2966.2007.12183.x.
- A. M. Atkinson, R. G. Abraham, and A. M. N. Ferguson. Faint Tidal Features in Galaxies within the Canada-France-Hawaii Telescope Legacy Survey Wide Fields. *ApJ*, 765:28, Mar. 2013. doi: 10.1088/0004-637X/765/1/28.
- J. Barnes. The dynamical state of groups of galaxies. *MNRAS*, 215:517–536, Aug. 1985. doi: 10.1093/mnras/215.3.517.
- A. M. Beck, G. Murante, A. Arth, R.-S. Remus, A. F. Teklu, J. M. F. Donnert, S. Planelles, M. C. Beck, P. Förster, M. Imgrund, K. Dolag, and S. Borgani. An improved SPH scheme for cosmological simulations. *MNRAS*, 455:2110–2130, Jan. 2016. doi: 10.1093/mnras/stv2443.
- J. Binney and S. Tremaine. *Galactic Dynamics: Second Edition*. Princeton University Press, 2008.
- A. Bittner. Spiral galaxies in cosmological zoom-simulations. Master’s thesis, Ludwig-Maximilians-Universität (LMU) München, 2018.
- A. Bonafede, K. Dolag, F. Stasyszyn, G. Murante, and S. Borgani. A non-ideal magnetohydrodynamic GADGET: simulating massive galaxy clusters. *MNRAS*, 418:2234–2250, Dec. 2011. doi: 10.1111/j.1365-2966.2011.19523.x.
- A. Ciccolella and M. D. Leo. *Hubble - de Vaucouleurs Galaxy Morphology Diagram*, 2016 (Accessed: 2018-03-14). URL [https://en.wikipedia.org/wiki/Galaxy\\_morphological\\_classification#/media/File:Hubble\\_-\\_de\\_Vaucouleurs\\_Galaxy\\_Morphology\\_Diagram.png](https://en.wikipedia.org/wiki/Galaxy_morphological_classification#/media/File:Hubble_-_de_Vaucouleurs_Galaxy_Morphology_Diagram.png).
- A. P. Cooper, O. H. Parry, B. Lowing, S. Cole, and C. Frenk. Formation of in situ stellar haloes in Milky Way-mass galaxies. *MNRAS*, 454:3185–3199, Dec. 2015. doi: 10.1093/mnras/stv2057.

- T. J. Cox, P. Jonsson, J. R. Primack, and R. S. Somerville. Feedback in simulations of disc-galaxy major mergers. *MNRAS*, 373:1013–1038, Dec. 2006. doi: 10.1111/j.1365-2966.2006.11107.x.
- C. Da Rocha, B. L. Ziegler, and C. Mendes de Oliveira. Intragroup diffuse light in compact groups of galaxies - II. HCG 15, 35 and 51. *MNRAS*, 388:1433–1443, Aug. 2008. doi: 10.1111/j.1365-2966.2008.13500.x.
- G. de Vaucouleurs. Classification and Morphology of External Galaxies. *Handbuch der Physik*, 53:275, 1959.
- K. Dolag, M. Reinecke, C. Gheller, and S. Imboden. Splotch: visualizing cosmological simulations. *New Journal of Physics*, 10(12):125006, Dec. 2008. doi: 10.1088/1367-2630/10/12/125006.
- K. Dolag, G. Murante, and S. Borgani. Dynamical difference between the cD galaxy and the diffuse, stellar component in simulated galaxy clusters. *MNRAS*, 405:1544–1559, July 2010. doi: 10.1111/j.1365-2966.2010.16583.x.
- A. Dressler. Galaxy morphology in rich clusters - Implications for the formation and evolution of galaxies. *ApJ*, 236:351–365, Mar. 1980. doi: 10.1086/157753.
- Edouard Jean-Marie Stephan. Nebulae (new) discovered and observed at the observatory of Marseilles, 1876 and 1877, M. Stephan. *MNRAS*, 37:334, Apr. 1877. doi: 10.1093/mnras/37.6.334.
- J. Einasto. On the Construction of a Composite Model for the Galaxy and on the Determination of the System of Galactic Parameters. *Trudy Astrofizicheskogo Instituta Alma-Ata*, 5:87–100, Jan. 1965.
- F. Governato, P. Tozzi, and A. Cavaliere. Small Groups of Galaxies: A Clue to a Critical Universe. *ApJ*, 458:18, Feb. 1996. doi: 10.1086/176789.
- R. L. Graham. An efficient algorithm for determining the convex hull of a finite planar set. *Inf. Process. Lett.*, 1(4):132–133, 1972.
- L. Hernquist. An analytical model for spherical galaxies and bulges. *ApJ*, 356:359–364, June 1990. doi: 10.1086/168845.
- L. Hernquist. N-body realizations of compound galaxies. *ApJS*, 86:389–400, June 1993. doi: 10.1086/191784.
- L. Hernquist and P. J. Quinn. Formation of Shell Galaxies. I. Spherical Potentials. *ApJ*, 331:682, Aug. 1988. doi: 10.1086/166592.
- P. Hickson. Systematic properties of compact groups of galaxies. *ApJ*, 255:382–391, Apr. 1982. doi: 10.1086/159838.

- P. Hickson. Compact Groups of Galaxies. *ARA&A*, 35:357–388, 1997. doi: 10.1146/annurev.astro.35.1.357.
- P. Hickson, C. Mendes de Oliveira, J. P. Huchra, and G. G. Palumbo. Dynamical properties of compact groups of galaxies. *ApJ*, 399:353–367, Nov. 1992. doi: 10.1086/171932.
- M. Hilz, T. Naab, J. P. Ostriker, J. Thomas, A. Burkert, and R. Jesseit. Relaxation and stripping - The evolution of sizes, dispersions and dark matter fractions in major and minor mergers of elliptical galaxies. *MNRAS*, 425:3119–3136, Oct. 2012. doi: 10.1111/j.1365-2966.2012.21541.x.
- M. Hilz, T. Naab, and J. P. Ostriker. How do minor mergers promote inside-out growth of ellipticals, transforming the size, density profile and dark matter fraction? *MNRAS*, 429:2924–2933, Mar. 2013. doi: 10.1093/mnras/sts501.
- G. Hinshaw, D. Larson, E. Komatsu, D. N. Spergel, C. L. Bennett, J. Dunkley, M. R. Nolta, M. Halpern, R. S. Hill, N. Odegard, L. Page, K. M. Smith, J. L. Weiland, B. Gold, N. Jarosik, A. Kogut, M. Limon, S. S. Meyer, G. S. Tucker, E. Wollack, and E. L. Wright. Nine-year Wilkinson Microwave Anisotropy Probe (WMAP) Observations: Cosmological Parameter Results. *ApJS*, 208:19, Oct. 2013. doi: 10.1088/0067-0049/208/2/19.
- E. Holmberg. On the Clustering Tendencies among the Nebulae. II. a Study of Encounters Between Laboratory Models of Stellar Systems by a New Integration Procedure. *ApJ*, 94:385, Nov. 1941. doi: 10.1086/144344.
- E. Hubble. No. 324. Extra-galactic nebulae. *Contributions from the Mount Wilson Observatory / Carnegie Institution of Washington*, 324:1–49, Jan. 1926.
- E. P. Hubble. *Realm of the Nebulae*. 1936.
- HubbleSite. *Stephans Quintett observed by the Hubble Space Telescope*, 2009 (Accessed: 2018-02-10). URL [http://hubblesite.org/image/2575/news\\_release/2009-25](http://hubblesite.org/image/2575/news_release/2009-25).
- M. L. Humason, N. U. Mayall, and A. R. Sandage. Redshifts and magnitudes of extragalactic nebulae. *AJ*, 61:97–162, 1956. doi: 10.1086/107297.
- N. Katz, D. H. Weinberg, and L. Hernquist. Cosmological Simulations with TreeSPH. *ApJS*, 105:19, July 1996. doi: 10.1086/192305.
- F.-S. Kitaura, S. Rodríguez-Torres, C.-H. Chuang, C. Zhao, F. Prada, H. Gil-Marín, H. Guo, G. Yepes, A. Klypin, C. G. Scóccola, J. Tinker, C. McBride, B. Reid, A. G. Sánchez, S. Salazar-Albornoz, J. N. Grieb, M. Vargas-Magana, A. J. Cuesta, M. Neyrinck, F. Beutler, J. Comparat, W. J. Percival, and A. Ross. The clustering of galaxies in the SDSS-III Baryon Oscillation Spectroscopic Survey: mock galaxy catalogues for the BOSS Final Data Release. *MNRAS*, 456:4156–4173, Mar. 2016. doi: 10.1093/mnras/stv2826.

- C. d. P. Lagos, A. R. H. Stevens, R. G. Bower, T. A. Davis, S. Contreras, N. D. Padilla, D. Obreschkow, D. Croton, J. W. Trayford, C. Welker, and T. Theuns. Quantifying the impact of mergers on the angular momentum of simulated galaxies. *MNRAS*, 473:4956–4974, Feb. 2018. doi: 10.1093/mnras/stx2667.
- R. Lange, A. J. Moffett, S. P. Driver, A. S. G. Robotham, C. d. P. Lagos, L. S. Kelvin, C. Conselice, B. Margalef-Bentabol, M. Alpaslan, I. Baldry, J. Bland-Hawthorn, M. Bremer, S. Brough, M. Cluver, M. Colless, L. J. M. Davies, B. Häußler, B. W. Holwerda, A. M. Hopkins, P. R. Kafle, R. Kennedy, J. Liske, S. Phillipps, C. C. Popescu, E. N. Taylor, R. Tuffs, E. van Kampen, and A. H. Wright. Galaxy And Mass Assembly (GAMA):  $M_{\text{star}} - R_e$  relations of  $z = 0$  bulges, discs and spheroids. *MNRAS*, 462:1470–1500, Oct. 2016. doi: 10.1093/mnras/stw1495.
- D. F. Malin and D. Carter. A catalog of elliptical galaxies with shells. *ApJ*, 274:534–540, Nov. 1983. doi: 10.1086/161467.
- D. Martínez-Delgado, R. J. Gabany, K. Crawford, S. Zibetti, S. R. Majewski, H.-W. Rix, J. Fliri, J. A. Carballo-Bello, D. C. Bardalez-Gagliuffi, J. Peñarrubia, T. S. Chonis, B. Madore, I. Trujillo, M. Schirmer, and D. A. McDavid. Stellar Tidal Streams in Spiral Galaxies of the Local Volume: A Pilot Survey with Modest Aperture Telescopes. *AJ*, 140:962–967, Oct. 2010. doi: 10.1088/0004-6256/140/4/962.
- T. K. Menon. Radio properties of spiral galaxies in high-density groups. *MNRAS*, 274:845–852, June 1995. doi: 10.1093/mnras/274.3.845.
- A. Merritt, P. van Dokkum, R. Abraham, and J. Zhang. The Dragonfly nearby Galaxies Survey. I. Substantial Variation in the Diffuse Stellar Halos around Spiral Galaxies. *ApJ*, 830, Oct. 2016. doi: 10.3847/0004-637X/830/2/62.
- T. Naab and J. P. Ostriker. Are Disk Galaxies the Progenitors of Giant Ellipticals? *ApJ*, 690:1452–1462, Jan. 2009. doi: 10.1088/0004-637X/690/2/1452.
- T. Naab, P. H. Johansson, and J. P. Ostriker. Minor Mergers and the Size Evolution of Elliptical Galaxies. *ApJ*, 699:L178–L182, July 2009. doi: 10.1088/0004-637X/699/2/L178.
- J. F. Navarro, C. S. Frenk, and S. D. M. White. A Universal Density Profile from Hierarchical Clustering. *ApJ*, 490:493–508, Dec. 1997. doi: 10.1086/304888.
- D. Obreschkow, K. Glazebrook, R. Bassett, D. B. Fisher, R. G. Abraham, E. Wisnioski, A. W. Green, P. J. McGregor, I. Damjanov, A. Popping, and I. Jørgensen. Low Angular Momentum in Clumpy, Turbulent Disk Galaxies. *ApJ*, 815:97, Dec. 2015. doi: 10.1088/0004-637X/815/2/97.
- S. A. Pardy, E. D’Onghia, and A. J. Fox. Models of Tidally Induced Gas Filaments in the Magellanic Stream. *ArXiv e-prints*, Feb. 2018.

- Planck Collaboration, P. A. R. Ade, N. Aghanim, M. Arnaud, M. Ashdown, J. Aumont, C. Baccigalupi, A. J. Banday, R. B. Barreiro, J. G. Bartlett, and et al. Planck 2015 results. XIII. Cosmological parameters. *A&A*, 594:A13, Sept. 2016. doi: 10.1051/0004-6361/201525830.
- C. W. Purcell, J. S. Bullock, and A. R. Zentner. Shredded Galaxies as the Source of Diffuse Intrahalo Light on Varying Scales. *ApJ*, 666:20–33, Sept. 2007. doi: 10.1086/519787.
- R.-S. Remus, K. Dolag, and T. Hoffmann. The Outer Halos of Very Massive Galaxies: BCGs and their DSC in the Magneticum Simulations. *Galaxies*, 5:49, Sept. 2017. doi: 10.3390/galaxies5030049.
- V. Rodriguez-Gomez, A. Pillepich, L. V. Sales, S. Genel, M. Vogelsberger, Q. Zhu, S. Wellons, D. Nelson, P. Torrey, V. Springel, C.-P. Ma, and L. Hernquist. The stellar mass assembly of galaxies in the Illustris simulation: growth by mergers and the spatial distribution of accreted stars. *MNRAS*, 458:2371–2390, May 2016. doi: 10.1093/mnras/stw456.
- A. J. Romanowsky and S. M. Fall. Angular Momentum and Galaxy Formation Revisited. *ApJS*, 203:17, Dec. 2012. doi: 10.1088/0067-0049/203/2/17.
- H. J. Rood and M. F. Struble. Spatial coincidence between a number of Hickson compact groups and loose groups or clusters. *PASP*, 106:413–416, Apr. 1994. doi: 10.1086/133393.
- V. C. Rubin. Evidence for dark matter from rotation curves: Ten years later. In *After the first three minutes. AIP Conference Proceedings, Volume 222, pp. 371-380 (1991).*, volume 222, pages 371–380, Apr. 1991. doi: 10.1063/1.40398.
- V. C. Rubin, D. A. Hunter, and W. K. Ford, Jr. Optical properties and dynamics of galaxies in the Hickson compact groups. *ApJS*, 76:153–183, May 1991. doi: 10.1086/191567.
- E. E. Salpeter. The Luminosity Function and Stellar Evolution. *ApJ*, 121:161, Jan. 1955. doi: 10.1086/145971.
- D. Schlachtenberger. The origin of cold gas in the center of massive elliptical galaxies. Master’s thesis, Ludwig-Maximilians-Universität (LMU) München, 2014.
- F. Schweizer. Observational evidence for mergers. In *IN: Internal kinematics and dynamics of galaxies; Proceedings of the Symposium, Besancon, France, August 9-13, 1982 (A83-49201 24-89)*. Dordrecht, D. Reidel Publishing Co., 1983, p. 319-326; Discussion, p. 327-329., volume 100, pages 319–326, Jan. 1983.
- F. Schweizer and J. Ford, W. K. *Fine Structure in Elliptical Galaxies*, page 145. 1985. doi: 10.1007/BFb0030934.
- J. L. Sersic. *Atlas de Galaxias Australes*. 1968.

- S. Shao, M. Cautun, C. S. Frenk, R. J. J. Grand, F. A. Gómez, F. Marinacci, and C. M. Simpson. The multiplicity and anisotropy of galactic satellite accretion. *MNRAS*, Feb. 2018. doi: 10.1093/mnras/sty343.
- S. Shen, H. J. Mo, S. D. M. White, M. R. Blanton, G. Kauffmann, W. Voges, J. Brinkmann, and I. Csabai. The size distribution of galaxies in the Sloan Digital Sky Survey. *MNRAS*, 343:978–994, Aug. 2003. doi: 10.1046/j.1365-8711.2003.06740.x.
- S. Skyum. A simple algorithm for computing the smallest enclosing circle. *Inf. Process. Lett.*, 37(3):121–125, Feb. 1991. ISSN 0020-0190. doi: 10.1016/0020-0190(91)90030-L.
- V. Springel. The cosmological simulation code GADGET-2. *MNRAS*, 364:1105–1134, Dec. 2005. doi: 10.1111/j.1365-2966.2005.09655.x.
- V. Springel and L. Hernquist. Cosmological smoothed particle hydrodynamics simulations: a hybrid multiphase model for star formation. *MNRAS*, 339:289–311, Feb. 2003. doi: 10.1046/j.1365-8711.2003.06206.x.
- V. Springel, N. Yoshida, and S. D. M. White. GADGET: a code for collisionless and gasdynamical cosmological simulations. *New A*, 6:79–117, Apr. 2001. doi: 10.1016/S1384-1076(01)00042-2.
- V. Springel, T. Di Matteo, and L. Hernquist. Modelling feedback from stars and black holes in galaxy mergers. *MNRAS*, 361:776–794, Aug. 2005. doi: 10.1111/j.1365-2966.2005.09238.x.
- A. F. Teklu, R.-S. Remus, K. Dolag, A. M. Beck, A. Burkert, A. S. Schmidt, F. Schulze, and L. K. Steinborn. Connecting Angular Momentum and Galactic Dynamics: The Complex Interplay between Spin, Mass, and Morphology. *ApJ*, 812:29, Oct. 2015. doi: 10.1088/0004-637X/812/1/29.
- A. Toomre and J. Toomre. Galactic Bridges and Tails. *ApJ*, 178:623–666, Dec. 1972. doi: 10.1086/151823.
- G. Tormen, F. R. Bouchet, and S. D. M. White. The structure and dynamical evolution of dark matter haloes. *MNRAS*, 286:865–884, Apr. 1997. doi: 10.1093/mnras/286.4.865.
- F. C. van den Bosch, G. Ogiya, O. Hahn, and A. Burkert. Disruption of dark matter substructure: fact or fiction? *MNRAS*, 474:3043–3066, Mar. 2018. doi: 10.1093/mnras/stx2956.
- B. A. Williams and J. H. van Gorkom. VLA observations of hydrogen in HCG 18. *AJ*, 95: 352–355, Feb. 1988. doi: 10.1086/114639.
- B. A. Williams, P. M. McMahon, and J. H. van Gorkom. VLA neutral hydrogen imaging of compact groups of galaxies. II - HCG 31, 44, and 79. *AJ*, 101:1957–1968, June 1991. doi: 10.1086/115820.

- 
- J. Zhang, R. Abraham, P. van Dokkum, A. Merritt, and S. Janssens. The dragonfly nearby galaxies survey. Iv. A giant stellar disk in ngc 2841. *ArXiv e-prints*, Feb. 2018.
- A. Zolotov, B. Willman, A. M. Brooks, F. Governato, C. B. Brook, D. W. Hogg, T. Quinn, and G. Stinson. The Dual Origin of Stellar Halos. *ApJ*, 702:1058–1067, Sept. 2009. doi: 10.1088/0004-637X/702/2/1058.





# Acknowledgements

The first person I have and I want to thank is PD Dr. Klaus Dolag for providing me the opportunity for writing my thesis with him and his fellows. Thanks for this very interesting topic, that you always took your time to help me, either regarding computational or scientific aspects, and also giving me the freedom to find my own way and letting me do my own mistakes.

I also want to thank Prof. Dr. Andreas Burkert for introducing me into his versatile CAST-group, his critical questions and helpful discussions.

The greatest thanks nevertheless goes to Dr. Rhea-Silvia Remus for always supporting me in doing detours during my thesis and showing me the greater picture of my work, especially when I was restricting my view onto the technical part of my work.

Last but not least, I want to thank all other people supporting and or distracting me during this time - was it during meetings, coffee breaks, in the office or after work. Unfortunately there were too many to name you all individually, but you made the time special.